

Constrained Simulation of the Bullet Cluster

by

Craig Lage

A dissertation submitted in partial fulfillment

of the requirements for the degree of

Doctor of Philosophy

Department of Physics

New York University

September 2014

Professor Glennys Farrar

Dedication

I dedicate this thesis to my wife, Sharon. Someone once asked me when I had met her, and I replied, “I don’t remember, she has always been there.” Thanks, Sharon, for always being there.

Acknowledgements

I have benefited from innumerable valuable discussions and advice from a great many colleagues – too many to list them all. Volker Springel and Yuval Birnboim provided support for getting started with the initial simulations. Eugene Vasiliev provided the SMILE software, and I thank him for that and for helpful discussions on its use. Much of the data analysis was done using the code known as *yt* [1], which greatly simplifies analysis of AMR output. Thanks also to Marusa Bradac for providing the mass lensing data, Tom Plagge for providing the SZ data and Maxim Markevitch for providing the extracted temperature map. Jeremy Tinker has provided helpful discussions on cosmology and growth of structure. Lastly, my heartfelt thanks to my thesis advisor Glennys Farrar for her continued support and encouragement.

Most of the simulations were done under GID S1248 on the NASA Pleiades supercomputer system, for which I gratefully acknowledge support. Computations described in this work were performed using the Enzo code developed by the Laboratory for Computational Astrophysics at the University of California in San Diego (<http://lca.ucsd.edu>). This work has been supported in part by grants NNX08AG70G, NSF PHY-1212538, NSF PHY-0900631 and NSF PHY-0970075.

Abstract

The Bullet Cluster collision is an ongoing collision of two galaxy clusters in the constellation of Carina. In this work, we have built a detailed simulation of this merger, including magnetohydrodynamics, plasma cooling, and adaptive mesh refinement. We constrain the simulation with data from gravitational lensing reconstructions and Chandra X-ray flux maps, then compare the resulting model to plasma temperature maps, Sunyaev-Zel'dovich effect measurements, and cluster halo radio emission. We constrain the initial conditions by minimizing the chi-squared figure of merit between the full 2D observational data sets and the simulation, rather than comparing only a few features such as the location of subcluster centroids, as in previous studies. A simple initial configuration of two triaxial clusters with Navarro-Frenk-White dark matter profiles and physically reasonable plasma profiles gives a good fit to the current observational morphology and X-ray emissions of the merging clusters. There is no need for unconventional physics or extreme infall velocities. The study gives insight into the astrophysical processes at play during a galaxy cluster merger. In addition, the techniques developed here to create realistic, stable, triaxial clusters, and to utilize the totality of the 2D image data, will be applicable to future simulation studies of other merging clusters. This work also highlights the important role of non-thermal pressure in galaxy clusters. A simple model of the non-thermal pressure is primarily used here, but we have investigated a more physical model where the non-thermal pressure is due to fluid turbulence, and have outlined a path for future work based on this more physical model.

Contents

Dedication	iii
Acknowledgements	iv
Abstract	v
List of Figures	ix
List of Tables	xii
1 Introduction	1
1.1 Overview	1
1.2 Goals of this Work	4
2 Galaxy Clusters and Cluster Collisions	6
2.1 The Large-Scale Structure of the Universe	6
2.2 The Structure of Galaxy Clusters	8
2.2.1 Galaxy Cluster Overview	8
2.2.2 Dark Matter Profiles	11
2.2.3 Baryon Profiles and X-ray Emission	14
2.2.4 Need for Non-Thermal Pressure	21
2.2.5 Cluster Shapes	23

2.2.6	Magnetic Fields	24
2.3	Collisions of Galaxy Clusters	25
3	Data, Tools, and Methods	27
3.1	Data	27
3.1.1	Summary of Observations	27
3.1.2	Primary Constraining Datasets	29
3.1.3	Secondary Comparison Datasets	30
3.2	Software Tools	31
3.2.1	Simulation Conditions	32
3.3	Methods	34
3.3.1	Generation of Initial Conditions and Fitting Parameters . .	34
3.3.2	Calculation of Observables	47
3.3.3	Optimization Procedure	55
3.3.4	Statistics	58
4	Results and Major Findings	61
4.1	Comparison of Best Fit Simulation to Observations	61
4.1.1	Mass Lensing	62
4.1.2	X-ray Flux	64
4.1.3	S-Z Effect, Plasma Temperature, and Non-Thermal Pressure	67
4.1.4	Role of Magnetic Field and Radio Halo Prediction	70
4.1.5	Summary of Best Fit Results	76
4.2	Comparison to Past Simulation Studies	77
4.3	Resolution Study	79
4.4	Cosmological Comparisons	81

4.4.1	Cluster Initial Velocities	82
4.4.2	Cluster Concentrations and Shapes	84
4.4.3	Comparison to Universal Baryon Fraction	87
4.5	Improved Modeling of Non-Thermal Pressure	89
5	Conclusions and Recommendations	98
5.1	Conclusions	98
5.2	Recommendations for Future Work	99
	Bibliography	102

List of Figures

2.1	Growth of Cosmic Structure	7
2.2	Abell-1689 - A typical large galaxy cluster.	10
2.3	Typical Dark Matter profile (simulation).	13
2.4	Mass-Concentration relation of galaxy clusters.	14
2.5	Measured Cluster Density Profiles	16
2.6	Measured Cluster Temperature Profiles	17
2.7	Measured Cluster Pressure Profiles	18
2.8	Typical Gas Density profile (simulation).	19
2.9	SZ Signal for Abell 2744.	21
2.10	Simulated Cluster Shapes	24
2.11	Bullet Cluster Collision	26
3.1	The primary datasets.	30
3.2	The six observational datasets.	31
3.3	Triaxial cluster shape stability	42
3.4	Triaxial cluster profile stability	43
3.5	Initial Baryon Distribution	44

3.6	Plasma emissivity due to thermal bremsstrahlung.	50
3.7	Plasma emissivity from APEC.	51
3.8	Typical evolution of the χ^2 parameter.	57
3.9	Behavior of the Radial Basis Function model.	60
4.1	Mass lensing fit between the data and the simulation.	63
4.2	Visualization of the collision path.	64
4.3	Best fit result for the X-ray flux.	65
4.4	X-ray flux on a log scale	66
4.5	Initial baryon profiles	67
4.6	X-ray flux and non-thermal pressure.	69
4.7	S-Z effect and non-thermal pressure	69
4.8	Plasma temperature and non-thermal pressure.	70
4.9	Impact of magnetic field on the X-ray flux.	72
4.10	Radio flux comparison.	73
4.11	Impact of spectral index.	74
4.12	Evolution of the collision.	75
4.13	Simulated Rotation Measure as compared to Measured Clusters	76
4.14	Spatially resolved contribution to χ^2 values.	77
4.15	Mass lensing compared to past simulation work.	78
4.16	X-ray flux compared to past simulation work	79
4.17	Impact of resolution on Mass Lensing fit	80
4.18	Impact of resolution on X-ray intensity fit	81
4.19	Initial cluster velocities	85
4.20	Total energy and Impact Parameter of Cluster Pairs	86
4.21	Best-fit masses and concentrations	86

4.22	Best-fit cluster axis ratios	88
4.23	Equilibrium temperature of clusters.	90
4.24	Energy balance of plasma in a galaxy cluster.	92
4.25	Non-thermal pressure radial profile.	93
4.26	Decay of turbulent fluid motion vs resolution.	95
4.27	Modeling non-thermal pressure through fluid turbulence	96
4.28	Fluid turbulence in NTP simulation.	97

List of Tables

3.1	Summary of Software Tools	32
3.2	Enzo simulation conditions.	33
3.3	Fitting Parameters	37
4.1	Comparison of initial infall velocities.	83

Chapter 1

Introduction

1.1 Overview

Galaxy clusters are the largest bound structures in the Universe. Mergers of these clusters are key events in the evolution of structure in our universe. The Bullet Cluster (1E0657-56) is an ongoing collision of two massive galaxy clusters which has been called, “the most interesting cluster in the Universe,” (Markevitch 2005 [2]). This cluster merger is interesting for several reasons, including its relatively simple structure (Markevitch 2002 [3]) and high surface brightness across the electromagnetic spectrum. For these reasons, the Bullet Cluster has been extensively studied observationally, and observational data has been gathered on the Bullet Cluster across a wide range of wavelengths with a number of different observational tools, making it an ideal laboratory for the study of the physics of galaxy clusters and their interactions.

Our current standard model of cosmology, the Λ CDM model, includes “Cold Dark Matter” as an important component. Most astrophysicists accept that this

dark matter is made up of an as yet undiscovered subatomic particle. However, direct searches for this particle have continued to fail to yield a clear discovery. This leaves open the possibility that the need for dark matter to explain our observations could be eliminated by modification of the laws of physics at large distances or small accelerations (see Kroupa 2012 [4], for example). The Bullet Cluster plays an important role in these discussions, because the clear separation of the lensing mass centroids from the centroids of the X-ray emission has been taken as one of the strongest demonstrations of the reality of dark matter as a physical substance (Clowe 2002 [5]; Clowe 2004 [6]). However, even this interpretation has been called into question and a modified gravity model has been proposed as an alternate explanation (Moffat 2007 [7]). Simulation studies offer a valuable tool for shedding light on these debates, because one can make changes to the physics of the simulation to investigate alternate physical models.

A number of simulation studies of the Bullet Cluster merger have been performed (Springel and Farrar 2007 [8]; Mastropietro and Burkert 2008; [9]Milosavljević 2007 [10]; Dawson 2013 [11]). Although there has been rough agreement with the observations, there has been disagreement on some key details of the initial conditions, especially the initial velocities of the two subclusters. These studies have raised the question of whether or not this cluster is consistent with a Λ CDM cosmology. Lee and Komatsu (2010 [12]) reviewed the simulations that had been done as of 2010, and found that, while the studies of Milosavljevic and Springel and Farrar were consistent with a Λ CDM cosmology, the study of Mastropietro and Burkert was not. Lee and Komatsu estimated that the large relative velocity of the two clusters seen by Mastropietro and Burkert had a probability between 3.6×10^{-9} and 3.3×10^{-11} of occurring in a Λ CDM universe. Hayashi and White

(2006 [13]) concluded that the Bullet Cluster was not an exceptionally rare event. Given the disagreements between the different simulation studies, there is clearly a need to add clarity to this situation.

We have undertaken to build a detailed simulation model of the Bullet Cluster merger, with the intent to use it to study cluster structure, dark matter-dark matter and dark matter-baryon interactions, possible modifications of general relativity, and to check the extent to which this cluster merger is or is not an outlier in Λ CDM cosmology. At the same time, constraints can be obtained on the present baryon and electron distributions, the magnetic field of the system and potentially on the non-thermal sources of support in X-ray clusters. One of the improvements of this study compared to past studies is that, rather than compare the simulation to the data using a small number of extracted parameters (mass centroids, calculated velocities, etc.), we compare the simulation to the observational data on a pixel-by-pixel basis. Extensive observations of the Bullet Cluster have been made at multiple wavelengths, and these two-dimensional images contain a large quantity of information. Our approach makes use of this information to provide details of the structure of the initial clusters and the physics of the collision. A second improvement presented here is the implementation of techniques to generate realistic, stable, triaxial clusters. We will show that our techniques result in an excellent fit to the observed mass lensing distribution for this cluster collision. We will also show reasonably good fits to the measurements of X-ray flux, Sunyaev-Zel'dovich (S-Z) effect, plasma temperature, and radio emission, although these results are more uncertain due to the additional “gastrophysics” degrees of freedom.

This thesis is organized as follows. We begin (Section 2.1) by reviewing the current knowledge of the large-scale structure of the universe, the structure of

galaxy clusters, and the process of galaxy cluster mergers. We then review the observational data that we use to constrain the simulations and the means of comparing the observations to the simulations (Section 3.1). This is followed by a description of the simulation tools employed (Section 3.2), the techniques for generating the clusters which are the inputs to the collision, the techniques for analyzing the output of the simulations, and the optimization and error estimation techniques (Section 3.3). We then show a set of image comparisons comparing the observations to the best fit simulations, and report what we have learned about the structure of the initial clusters (Section 4). Finally, we discuss the major conclusions (Section 5.1), and outline a path for future work (Section 5.2). We note that much of this work has been peer reviewed and published (Lage and Farrar 2014 [14]).

1.2 Goals of this Work

Given the above considerations, we identified the following goals at the beginning of this work:

1. Build a detailed simulation of the Bullet Cluster merger, including dark matter, baryonic matter, magnetic fields, and plasma cooling.
2. Develop the software tools to allow quantitative comparison of the simulation to the observations by calculating a chi-squared figure of merit between the 2D observational images and the simulation on a pixel-by-pixel basis.
3. Use the developed tools to explore the space of initial conditions and quantify the structure of the two galaxy clusters participating the collision before the

collision began, including the cluster magnetic fields.

4. Use the developed tools to explore the space of initial conditions to clarify the disagreements on whether or not the cluster collision is consistent with the Λ CDM standard cosmological model.
5. After developing a simulation which adequately fits the observations using standard physics, explore the addition of dark matter - dark matter and dark matter - baryon interactions and attempt to place limits on the magnitude of these interactions. Limits based on these lines have already been published (Markevitch 2004 [15]; Randall 2008 [16]), but we hope to improve on these limits.

Chapter 2

Galaxy Clusters and Cluster Collisions

2.1 The Large-Scale Structure of the Universe

The last few decades have seen the transition of cosmology from a qualitative discipline to a quantitative science, causing the current situation in the field to often be referred to as the era of “Precision Cosmology”. A detailed exposition of the current status of cosmology is beyond the scope of this thesis, but a short summary is needed to set the stage for the work. Readers interested in more detail are referred to one of the many good textbooks on the topic such as Mukhanov (2005 [17]). The standard Λ CDM model of cosmology is extremely successful in describing the properties and evolution of the universe at large scales. Based on this model, we know that small initial density perturbations have grown under the influence of gravity into the large-scale structure that we see today. An example of this known as the Horizon Run (Kim 2009 [18]) is shown in Figure 2.1. This is

a dark-matter-only simulation of structure growth as the Universe has evolved.

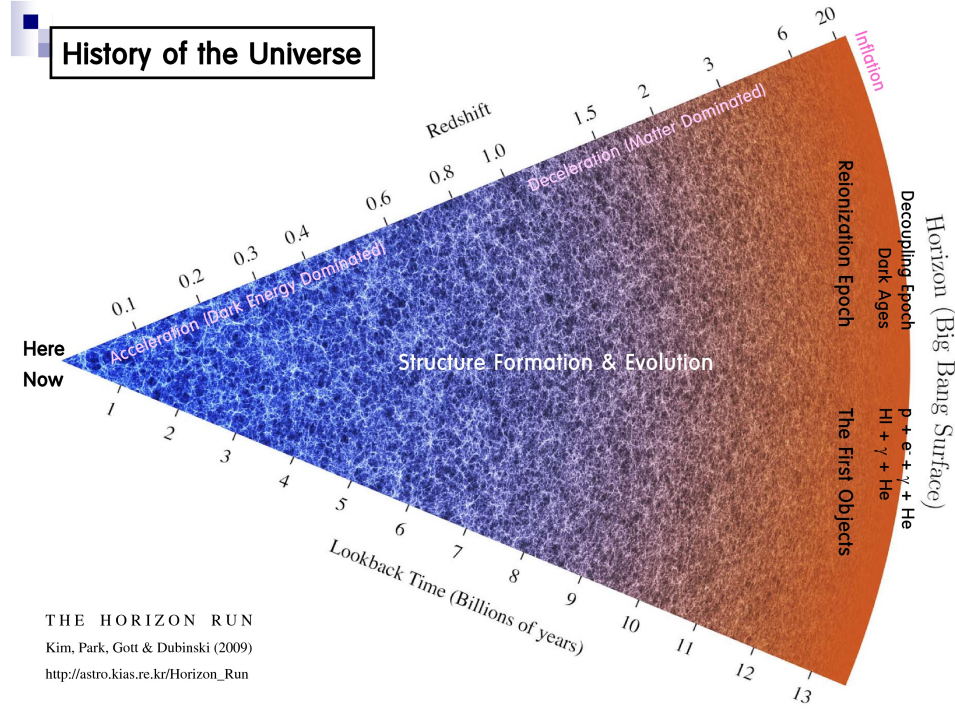


Figure 2.1: Growth of cosmic structure as seen in the Horizon simulation (Kim 2009 [18]).

The standard Λ CDM model of cosmology is a solution to the Friedmann equations, which result from applying the equations of General Relativity to the Universe as a whole. Observationally, it is found that the Universe is quite close to being spatially flat, which means that the average mass-energy density of the Universe is close to the critical density:

$$\rho_{\text{Crit}} = \frac{3H_0^2}{8\pi G}, \quad (2.1)$$

where H_0 is the Hubble constant. It is usual to describe the different components of the density as fractions of the critical density, as follows:

$$\Omega_i = \frac{\rho_i}{\rho_{\text{Crit}}}. \quad (2.2)$$

In this work, all cosmological calculations assume the following parameters:

$$H_0 = 70 \frac{\text{km}}{\text{sec Mpc}} \quad \Omega_m = 0.30 \quad \Omega_\Lambda = 0.70. \quad (2.3)$$

Here Ω_m represents the fraction of the density due to matter, and Ω_Λ represents the fraction of the density due to dark energy. We can further partition Ω_m into Ω_b , the fraction due to baryons (ordinary matter) and Ω_{CDM} , the fraction due to dark matter. This study will shed light on the ratio of these two quantities, and how our simulations compare to the Λ CDM model, as will be discussed in later sections.

2.2 The Structure of Galaxy Clusters

2.2.1 Galaxy Cluster Overview

We begin by reviewing the major features of galaxy clusters using Figure 2.2, which shows some of the typical features of a galaxy cluster (Peng 2008 [19]; Chandra website 2008 [20]). This galaxy cluster, Abell-1689, is at a redshift $z = 0.18$, placing it at a distance of approximately 700 Mpc (cosmological distance calculations follow Hogg 1999 [21]). The cluster has a total mass determined from mass lensing of approximately $2.0 \times 10^{15} M_\odot$ (Coe 2010 [22]). The white light image,

taken with the Hubble Space Telescope, clearly shows the large number of galaxies contained in the cluster; the galaxies in this cluster number in the thousands. Near the center of the cluster is a large elliptical galaxy. Large clusters typically have a large elliptical galaxy near the center which is referred to as the “Brightest Cluster Galaxy” (BCG), or sometimes as the “Central Dominant” (cD) galaxy. Also visible in the white light image are a number of curved arcs, roughly concentric with the center of the cluster. These are lensed images of galaxies or quasars more distant than the Abell-1689 cluster. By building a model of the galaxy cluster and the distant galaxies which are being lensed, one can determine the distribution of mass within the galaxy cluster. It is important to note that mass determination through gravitational lensing is independent of the type of matter doing the lensing; any matter which contributes to the gravitational field is included in the lensing mass determination. From this, as well as from other observations, it is known that galaxy clusters contain large amounts of non-luminous (i.e. “dark”) matter.

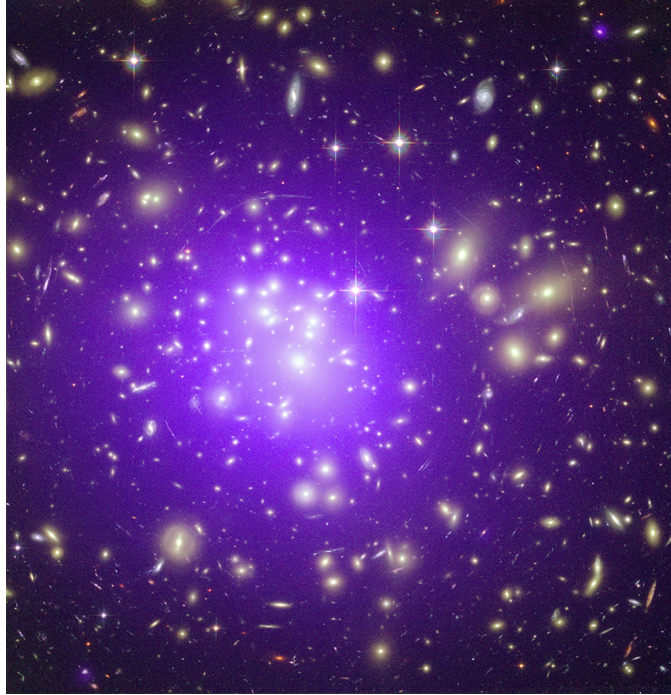


Figure 2.2: Abell-1689 - A typical large galaxy cluster.

Overlaid with the visible light image in Figure 2.2 is a false color (violet) image of the cluster taken in the X-ray region with the Chandra X-ray telescope. Large galaxy clusters contain most of their ordinary matter (i.e. baryons) in the form of hot, diffuse ionized gas (i.e. plasma). This hot gas emits X-rays, primarily through the mechanism of bremsstrahlung as energetic electrons are accelerated through collisions with the more massive ionized nuclei. This X-ray radiation is visible to an X-ray detector like Chandra, and can be used to gather information on the density and temperature of the hot gas (Vikhlinin 2005 [23]). Perhaps surprisingly, it is found that in massive clusters most of the baryonic mass of the cluster is in the form of this hot gas, and the baryonic mass in the form of stars is only a few percent of the total (Gonzalez 2013 [24]).

2.2.2 Dark Matter Profiles

It has long been known that galaxy clusters contain large quantities of non-luminous matter. In fact, the original motivation for the dark matter concept came from Zwicky's analysis of galaxy cluster velocity dispersions in the 1930's (Zwicky 1937 [25]). Today, large N-body simulations based on the Λ CDM model of cosmology accurately reproduce the observed large-scale structure of the Universe. These simulations show that the visible part of galaxy clusters are embedded in large extended dark matter halos. By examining the density profiles of these dark matter halos, a number of semi-empirical models of these halos have been developed. One of the more successful of these has been the NFW profile, based on the work of Navarro, Frenk, and White (1996 [26]). While other profiles, such as the Einasto and Sersic profiles have been proposed, the simple two-parameter NFW is widely used and has been shown to do a good job of reproducing the simulated dark matter halo profiles (see Merritt et.al. 2006 [27] for a review of these profiles). The NFW profile is the model used in this work.

The NFW profile is a two parameter model, comprising a density parameter ρ_0 and a scale radius parameter R_C , as follows:

$$\rho_{\text{DM}} = \frac{\rho_0}{\frac{R}{R_C}(1 + \frac{R}{R_C})^2}. \quad (2.4)$$

At radii much less than the scale radius R_C , the density falls off $\propto 1/R$, and at radii much larger than the scale radius, the density falls off $\propto 1/R^3$. Defining the total mass included in the NFW profile is problematic, since integrating the profile from $R = 0$ to $R = \infty$ gives an infinite result. Thus, it is necessary to cut off the integral at some large but finite radius in order to give a finite result. The usual

prescription for doing this is to integrate the density until it falls to 200 times the critical density of the universe (the density which results in a flat Universe as described by the Friedmann equations). This radius is then referred to as the “virial radius”, or R_{200} . One then further defines the concentration parameter C of the dark matter halo as the ratio of the virial radius to the scale radius, and the mass of the halo M_{200} as the total halo mass contained within the virial radius. Integrating the profile then gives the following relations, where ρ_{CRIT} is the critical density of the Universe at $z=0$:

$$R_{200} = \left[\frac{M_{200} C^2}{4\pi 200 \rho_{\text{CRIT}} (1+z)^3 (1+C) ((1+C) \ln(1+C) - C)} \right]^{1/3}, \quad (2.5)$$

$$C = \frac{R_{200}}{R_C}, \quad (2.6)$$

$$\rho_0 = \frac{M_{200} C^3 (1+C)}{4\pi R_{200}^3 ((1+C) \ln(1+C) - C)}. \quad (2.7)$$

It is usually more convenient to use the two parameters (M_{200}, C) to characterize the halo instead of the two parameters (ρ_0, R_C), and this is the convention that is used in this work. Figure 2.3 shows a typical dark matter profile, calculated for a cluster at $z=0$ with a mass of $M_{200} = 1.0\text{E}15 M_\odot$ and a concentration factor $C=3.0$. The change in slope from a $1/R$ to a $1/R^3$ profile is clearly seen.

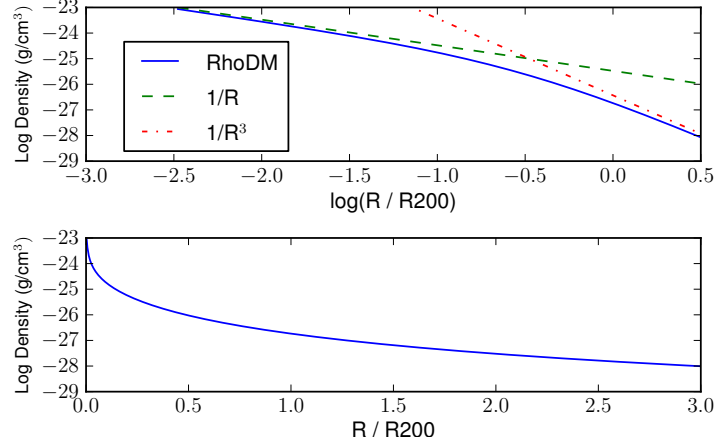


Figure 2.3: Typical Dark Matter profile (simulation).

While the value of R_{200} is most often used to quantify the size of the cluster, other similarly defined measures, such as R_{100} , R_{180} , and R_{500} are also used.

It is also found both observationally and through simulation (see for example Comerford 2007 [28]; Vikhlinin 2006 [29]; Okabe 2010 [30]; Bhattacharya 2013 [31]) that the concentration and masses of galaxy clusters are not fully independent parameters, in that more massive clusters tend to be less concentrated. Figure 2.4, reproduced from Comerford, et.al. [28] shows this relation.

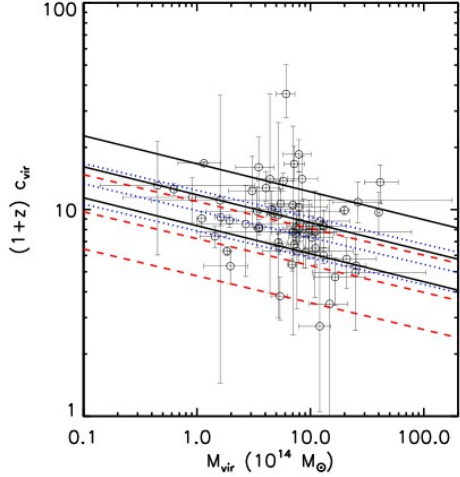


Figure 2.4: Mass-Concentration relation of galaxy clusters.

2.2.3 Baryon Profiles and X-ray Emission

While the dark matter halo of a galaxy cluster is believed to dominate the total mass of the cluster, it is not directly observable, and is only detected through its gravitational effects. However, clusters also contain a significant quantity of hot, ionized gas (plasma) which is directly observable through a variety of techniques. The most direct method is through measurement of the X-rays emitted by the hot gas, as seen in the violet overlay in Figure 2.2. With the advent of orbiting X-ray satellites like Chandra [32] and XMM-Newton, it is now possible to get detailed X-ray images of galaxy clusters. These instruments detect X-ray photons in the approximate energy range of 0.5-10.0 keV, and use grazing-incidence X-ray mirrors which are capable of forming images with arc-second resolution.

The hot gas emits X-rays through several mechanisms, including bremsstrahlung, emitted when electrons are accelerated through collisions with the heavier ions, and line emission from electronic transitions in heavier elements. The quantitative cal-

culation of the X-ray emission from the hot plasma is discussed in detail in Section 3.3.2.2. From analysis of the X-ray emission from galaxy clusters, many studies have been performed to quantify the density and temperature profiles of the hot ionized gas. Figure 2.5, reproduced from Vikhlinin (2006 [29]) shows measured density profiles of both the total mass and the X-ray emitting gas. The thick yellow line is the calculated NFW profile, which is seen to fit the total mass profile well. It is seen that there are a range of profiles for the cluster gas, but that in general the gas density profile follows a similar trend to the total matter density profile. However, since the gas density profile falls off less steeply than the total matter profile, the baryon fraction (i.e. the fraction of total mass made up of baryons) increases as one moves out from the center of the cluster.

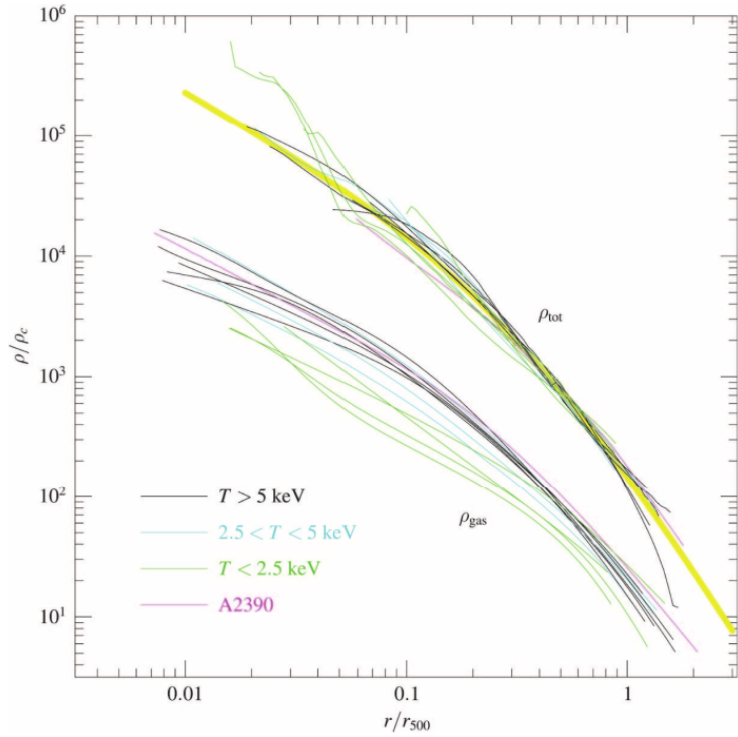


Figure 2.5: Measured total matter density and gas density as a function of radius for a number of X-ray emitting galaxy clusters. The thick yellow line is the calculated NFW profile. Figure reproduced from Vikhlinin [29].

Because the X-ray flux is caused by collisions between gas particles, the X-ray flux scales as the square of the gas number density. This means that the X-ray flux increases dramatically at the center of the cluster where the number density is the highest. The cluster gas density is low enough that the cluster is typically optically thin, so the X-ray flux emitted from the cluster gas is radiated away and causes the cluster gas to lose energy. This causes the center of the cluster to have a cooler region caused by the higher rate of energy loss due to X-ray radiation. This is clearly illustrated in Figure 2.6, reproduced from Leccardi and Molendi (2008 [33]), which shows the temperature profiles for a sample of galaxy clusters.

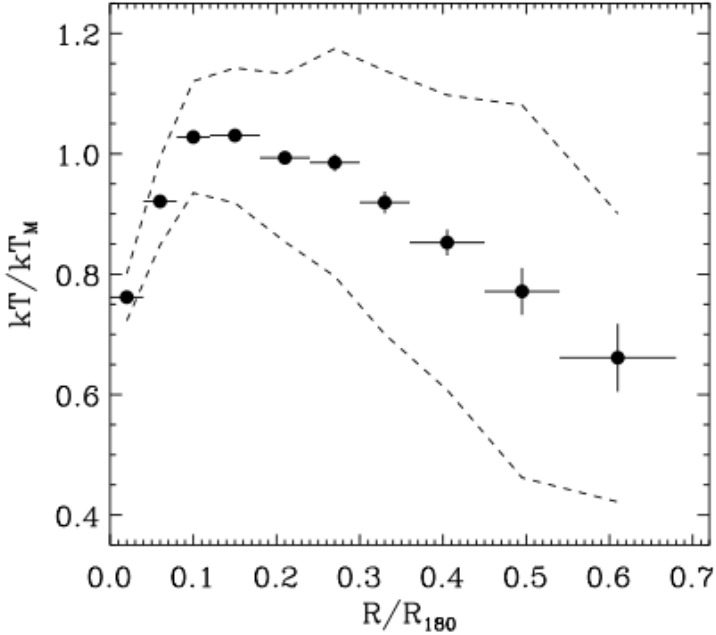


Figure 2.6: Measured temperature profiles for a sample of galaxy clusters. The dots are the mean temperature and the dotted lines show the one sigma scatter. T_M is the mean cluster temperature outside $0.1 R_{180}$. Figure reproduced from Leccardi and Molendi [33].

While the gas density and gas temperature profiles follow some general trends, there is considerable variability among clusters. However, the gas pressure of clusters follows a more universal profile. The reason is that the total mass density of the cluster is dominated by the dark matter, and the total mass density is what sets the gravitational potential. The gradient of the gravitational potential gives the gravitational force, which in hydrostatic equilibrium is balanced by the fluid pressure. Thus it is found that, when scaled properly, the pressure profile of galaxy clusters all follow a similar trend. Figure 2.7, reproduced from Arnaud (2010 [34]), shows this relation.

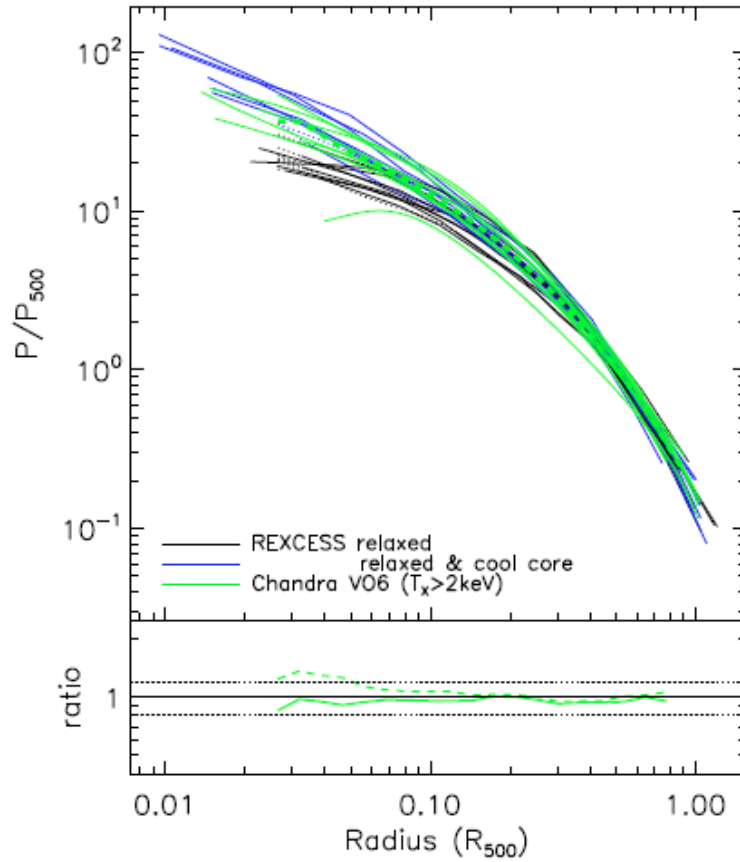


Figure 2.7: Measured cluster pressure profiles for a sample of galaxy clusters. The green curves are from Vikhlinin [29], while the blue and black curves are from Arnaud [34]. The Figure is reproduced from [34].

Since the density and temperature of the gas can vary independently, modeling of the cluster gas profiles can be complex. One simple model that has enjoyed significant success is the so-called “Beta-model” (see Arnaud 2009 [35]) for an excellent description of the history of this model). In this model, the gas density is assumed to follow a profile of the following form:

$$\rho_G = \frac{\rho_{G0}}{(1 + (\frac{R}{R_C})^2)^{3\beta/2}}. \quad (2.8)$$

Here R_C is referred to as the “cooling radius”, and β describes the fall-off of the plasma density. A value of $\beta = 1$ represents an isothermal plasma. Figure 2.8 shows some representative gas density profiles for a range of values of the parameter β .

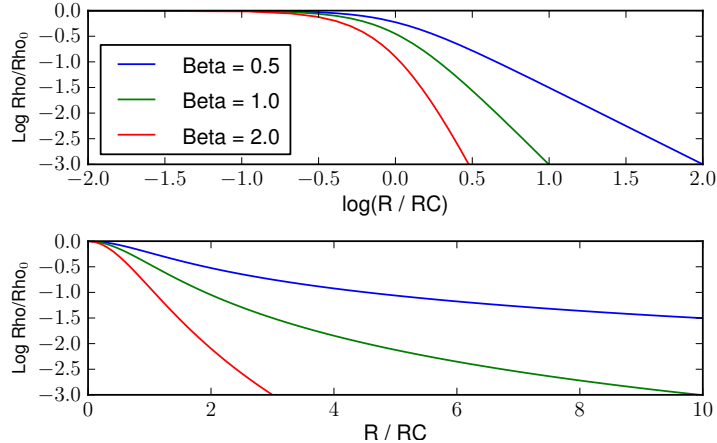


Figure 2.8: Typical Gas Density profile (simulation).

The X-ray flux is an important observational signal used for characterizing the gas properties of a galaxy cluster. An equally important signal, especially in recent years, is the use of the Sunyaev-Zel'dovich effect. The effect is caused by inverse Compton scattering of the Cosmic Microwave Background(CMB) photons by the hot plasma, which leads to a distortion of the CMB blackbody spectrum. We will quantify this in more detail in Section 3.3.2.2, but at this point we will simply state that the S-Z effect leads to a reduction in the measured CMB temperature which is proportional to the gas pressure (gas density times gas temperature) integrated along the line of sight. For this reason, large galaxy clusters cause “shadows” of the CMB radiation which have a slightly reduced temperature. The S-Z signal can

be measured with ground and space-based radio telescopes, and investigations of these signals has led to a rapid acceleration of our understanding of the structure of massive galaxy clusters (see, for example, Battaglia 2010 [36]; Battaglia 2012 [37]; Khedekar 2013 [38]; Prokhorov 2012 [39]; Birnboim 2013 [40]). Because the S-Z signal is proportional to the gas density, and the X-ray flux is proportional to the square of the gas density, these two signals together can help give independent measures of the density and the temperature, and we utilize these independent measures to characterize the Bullet Cluster in this work. An example of the S-Z signal of a large galaxy cluster is shown in Figure 2.9 (Plagge 2010 [41]). Another reason for the importance of the S-Z signal is that the S-Z signal is independent of redshift. This makes it an excellent tool for identifying distant clusters at high redshift, where the individual galaxies have become quite dim and difficult to image with optical telescopes.

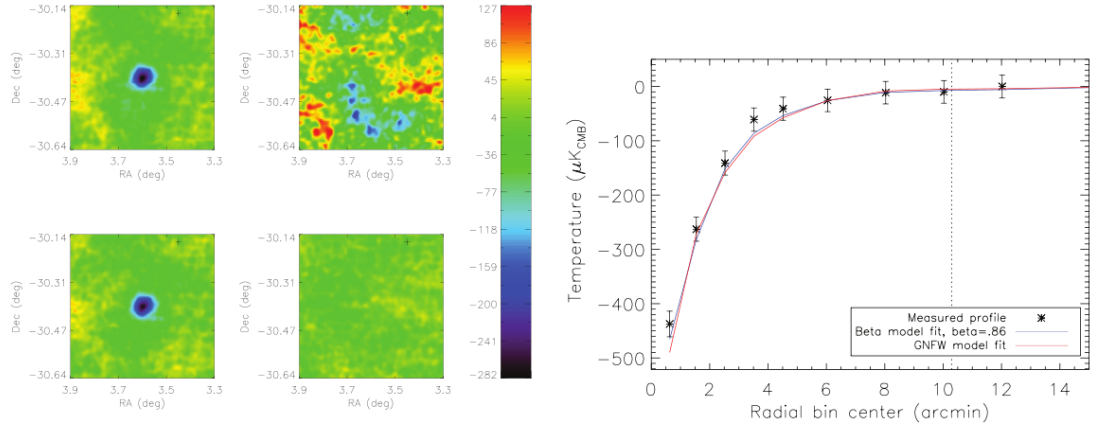


Figure 2.9: The Sunyaev-Zel'dovich signal for the cluster Abell 2744, measured with the South Pole Telescope. The four colored maps are in μK and are 150 GHz (upper left), 220 GHz (upper right), where the S-Z signal is much reduced, band subtracted (lower left), and jackknife noise map(lower right). These maps are reproduced from Plagge [41].

2.2.4 Need for Non-Thermal Pressure

It has been known for some time (see, for example Loeb 1994 [42]) that a significant amount of non-thermal pressure support is needed in galaxy clusters in order to agree with the observations. The assumption that the gas in galaxy clusters is in hydrostatic equilibrium leads to predictions of gas temperature that are well in excess of what is observed. Thus, some form of non-thermal pressure appears to be supporting the gas, in addition to the thermal pressure. Several mechanisms have been suggested as the source of this non-thermal pressure, including turbulent gas motions, and cosmic ray particles (Battaglia 2010 [36]; Bode 2009 [43]; Bruggen 2005 [44]; Lazarian 2011 [45]). Recent publications indicate that the turbulent fluid motions are the likely dominant source of the non-thermal pressure (Shi and

Komatsu 2014 [46]; Nelson 2014 [47]; Battaglia 2012 [37]), and our results in this work are consistent with this, as will be shown in Section 4.5.

Even if the turbulent fluid motions are the dominant source of the non-thermal pressure, there still remains the question of what sustains these turbulent motions over time, since viscosity will cause the turbulent motions to dissipate and be converted to thermal energy. In addition, without a source of energy to sustain a reservoir of thermal and non-thermal pressure, simulations of galaxy clusters are susceptible to a “cooling-flow problem”. Since the central region of the galaxy cluster is radiating X-rays most strongly, energy is carried away from the central region, causing the center to cool and the thermal pressure to be reduced. Gas from the outer regions, now lacking pressure support, then flows into the central regions, increasing the density and consequently the X-ray emissions, leading to further cooling. Simulations show that, lacking a continued energy source, the gas in galaxy clusters should collapse in a time short compared to the Hubble time. While clusters are observed to have cores of cooler plasma (Vikhlinin 2005 [23]; Markevitch 2007 [48]; Owers 2009 [49]), these cores appear to be relatively stable and are not collapsing. This discrepancy with observation has been referred to as the “cooling catastrophe problem” (Blanton 2002 [50]; Vernaleo 2006 [51]; Parrish 2009 [52]). We therefore conclude that there must be a source of energy flowing into the cluster gas to maintain the pressure support. The most likely source of energy to sustain the thermal energy and turbulent fluid motions is energetic outflows from Active Galactic Nuclei (AGN) (Battaglia 2010 [36]). However, the details of this energy outflow, such as the rate of energy transfer and whether the energy flow is continuous or intermittent, is still being actively investigated.

2.2.5 Cluster Shapes

Galaxy clusters grow with time as the large-scale structure of the Universe grows. Since the clusters grow from hierarchical mergers of smaller structures, they are generally not spherically symmetric. There are two main sources of information on the shape of the clusters. First, we can infer the shape of the mass distribution from gravitational measurements or by observing the shapes of the X-ray emissions from the hot gas (Limousin 2013 [53]). Second, N-body simulations of the growth of large-scale structure can be interrogated to determine the shapes of the dark matter halos (Schneider 2012 [54]; Bailin 2005 [55]). All of these studies agree that galaxy clusters are typically not spherical in shape. The recent study by Lau [56] also shows how the shapes can help elucidate the physics involved in cluster formation.

In order to quantify the shape of these clusters, we introduce a set of axis ratios. We assume that the clusters are ellipsoidal shapes with each of the three axes of the ellipsoid being different. We arbitrarily define the X-axis as the longest axis and the Z-axis as the shortest axis. The shape of the ellipsoid is then completely determined by the two ratios of these three axes, with P being the Z-axis to X-axis ratio, and Q being the Y-axis to X-axis ratio. With these definitions, we have $1.0 \geq Q \geq P \geq 0.0$. If the X and Y axes are equal (meaning $Q = 1$), then the ellipsoid is an oblate spheroid, with a shape like a pancake. If the Y and Z axes are equal (meaning $P = Q$), then the ellipsoid is a prolate spheroid, with a shape like a cigar. If all three axes are equal, then the shape is a sphere, and if all three axes are unequal, we refer to the shape as triaxial. Bailin, et.al. (2005 [55]) have extracted the shapes of a large number of dark matter halos that result from an N-body simulation of structure growth, with the result shown in Figure 2.10. It

can be seen that the majority of galaxy clusters are triaxial.

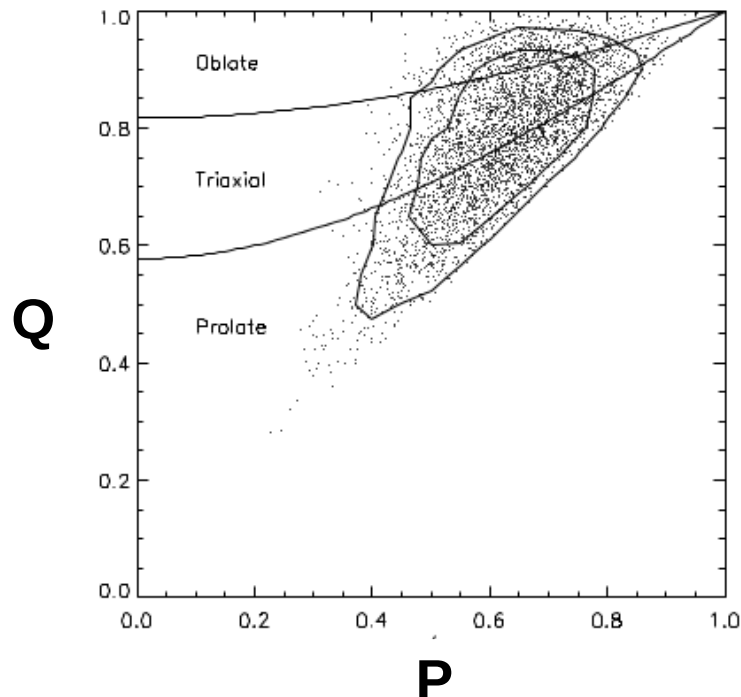


Figure 2.10: Axis ratios of dark matter halos of galaxy clusters from N-body simulations. Reproduced from [55].

2.2.6 Magnetic Fields

The magnetic fields of galaxy clusters are of interest for a number of reasons. First, radio emissions are detected from galaxy clusters (especially merging clusters), and it is believed that these radio emissions are due, at least in part, to synchrotron emission from energetic electrons spiraling along magnetic field lines. Knowing the strength and structure of the cluster magnetic fields allows one to model these radio emissions. Second, it is clear that the cluster magnetic fields are amplified during cluster collisions by the conversion of turbulent fluid energy

to magnetic field energy. Measurements of cluster magnetic fields have been attempted by measuring the Faraday rotation of distant sources as their radiation passes through the galaxy cluster. Such measurements indicate that cluster magnetic fields can reach values as high as 10's of μG (Carilli 2002 [57]; Vogt 2003 [58]; Ensslin 2009 [59]), and it has been suggested that the magnetic fields may reach levels where they become dynamically important [57]. Attempts have also been made to correlate the cluster magnetic fields with cluster radio emission [60]. These measurements, together with simulations (Dolag 1999 [61]; Dolag 2001 [62]; Dolag 2002 [63]; Kotarba 2011 [64]), show that the magnetic fields in the clusters are larger in regions of higher gas density, and Dolag (2001 [62]) has suggested a scaling of $|B| \propto \rho^{0.9}$. We will discuss our attempts to model the magnetic fields in the Bullet cluster collision in the subsequent sections.

2.3 Collisions of Galaxy Clusters

Clusters of galaxies grow in a hierarchical process through mergers of smaller clusters. Kravtsov (2012 [65]) has written an excellent review of the formation of clusters. This process has been ongoing through the history of the universe, resulting in the large clusters we see today. While some of the galaxy clusters we observe today are relatively quiescent, others are clearly in the process of merging. In addition to the Bullet Cluster, some of the other interesting merging clusters are known as “El Gordo”, the “Musket Ball Cluster”, Abell 576, Abell 520, and Abell 222/223. However, of these, the Bullet Cluster is perhaps the most interesting due to its very simple structure which apparently consists of two clusters merging very nearly in the plane of the sky. Figure 2.11 shows a composite image of the Bullet

Cluster collision (Clowe [66]). The white light image is from the Hubble space telescope. The blue overlay shows the location of the cluster mass, as determined from gravitational lensing (Bradac 2006 [67]). The pink overlay shows the X-ray flux map from the Chandra X-ray telescope (Markevitch 2005 [2]). This image has become somewhat of an iconic image with respect to the search for the existence of dark matter, in that the clear separation of the mass centroids from the X-ray flux centroids has been taken as “proof” of the existence of dark matter. (Clowe 2006 [6]). As discussed above, the ability to use a galaxy cluster merger as a laboratory to study our knowledge of the structure of clusters and their interactions is one of the prime motivations for this work.

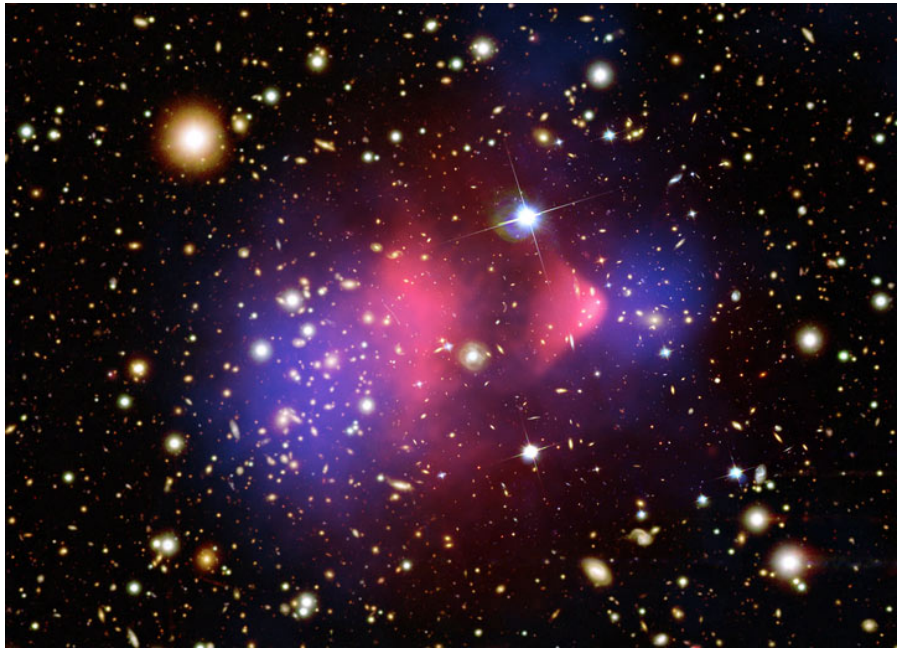


Figure 2.11: Composite image of the Bullet Cluster collision. The white light image is from the Hubble space telescope. The blue overlay shows the location of the cluster mass, as determined from gravitational lensing [67]. The pink overlay shows the X-ray flux map from the Chandra X-ray telescope [2]. Figure from [66].

Chapter 3

Data, Tools, and Methods

3.1 Data

One of the primary goals of this study is to build a detailed simulation of the Bullet Cluster collision and compare the simulation to observations. To this end, we have collected a number of observations of the Bullet Cluster which have been made at a wide range of wavelengths. This section summarizes those observations.

3.1.1 Summary of Observations

There are a total of six observational datasets which we compare to the simulation:

- A mass lensing reconstruction
- Three maps of X-ray intensity in different energy bins
- The Sunyaev-Zel'dovich effect CMB temperature decrement
- The radio halo intensity.

Each dataset is converted to a 2D map containing 110x110 pixels¹, where for each pixel we have an observed value and an estimated uncertainty. Two primary datasets, the mass lensing data and the lowest energy X-ray flux, are used to constrain the simulation initial conditions and fitting parameters. The resulting simulation is then used to generate images which are compared to the remaining four datasets. We have manually identified the central region where the data has the highest confidence, and only pixels inside this region are included in the χ^2 calculation in Equation 3.1. This region is shown by the heavy white outline in Figure 3.1; it contains 5780 pixels in each dataset and is about 4.5 arc minutes across.

Using the two primary datasets, we construct the following combined figure of merit to measure the quality of fit between simulation and measurement

$$\chi^2 = \frac{1}{N_k N_i} \sum_{\text{Observations}=k}^{N_k} \sum_{\text{Pixels}=i}^{N_i} \frac{(\text{Sim}_i^k - \text{Obs}_i^k)^2}{(\sigma_i^k)^2}, \quad (3.1)$$

and then vary the parameters to minimize this χ^2 . For brevity, we refer to this parameter as χ^2 throughout this work, but in fact it is χ^2 per degree of freedom. When fitting to the two primary datasets, the product $N_k N_i$ is 11,560. We note that the parameter χ^2 is used as a figure of merit for finding the best fit initial conditions. Our large-scale simulation provides a mean description of the system, and is not expected or intended to capture small-scale details such as inhomogeneous initial conditions and accretion of small mass concentrations during the merging process. For these reasons, although the χ^2 parameter is useful for finding the best-fit initial conditions, we do not expect a value of one.

¹Maps of 110x110 pixels were chosen for historical reasons. The initial mass lensing maps were at this resolution, so all subsequent maps were adjusted to match.

3.1.2 Primary Constraining Datasets

- *The gravitational lensing reconstruction from Bradac et.al. (2006 [67]).* This dataset consists of the total projected mass in each 2D pixel as determined to reproduce the observed weak and strong lensing data. The values of σ_i associated with the reconstruction have also been provided by M. Bradac [private communication]; these typically range from 5-25% of the mass lensing data. More recently, a new mass reconstruction has become available (Paraficz et.al. 2012 [68]). We have examined this new reconstruction, and it shows promise of resolving some of the discrepancies we see, but it is not incorporated into this analysis.
- *X-ray flux measurements from the Chandra X-ray observatory [32].* A total of 9 separate observations are included in the datasets, representing a total observing time of 558 ks. The X-ray flux is binned into three separate energy bins, 500eV - 2000eV, 2000eV - 5000eV, and 5000eV - 8000eV. The lowest energy bin (500eV - 2000eV), which contains most of the photons, is our second primary dataset, along with the mass-lensing map. The “Ciao” [69] software analysis package is used to reduce the measured data to an X-ray flux in photons/(cm²sec). For this data, a statistical uncertainty of $1/\sqrt{N_{\text{photons}}}$ and a systematic uncertainty of 1.7% [32] are combined in quadrature to generate σ_i .

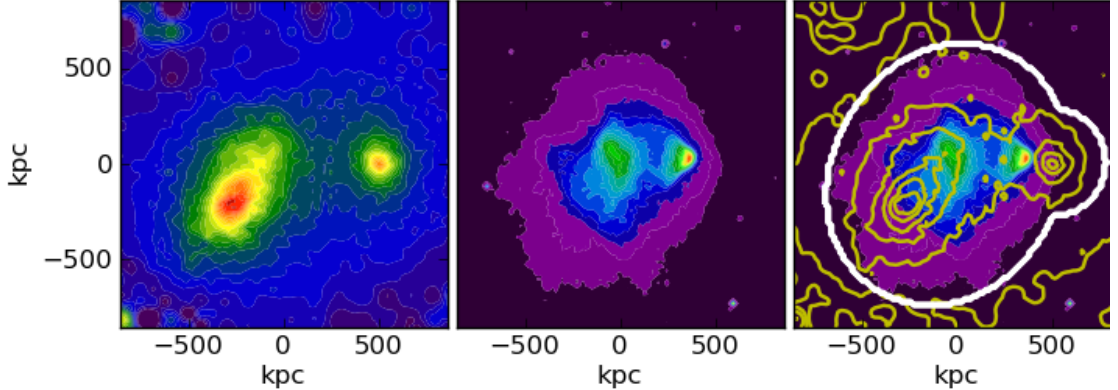


Figure 3.1: The primary datasets. Left: Mass lensing dataset. Center: 500eV-2000eV X-ray flux dataset. Right: These two primary datasets overlaid. Only the region inside the heavy white outline is included in the χ^2 calculation.

3.1.3 Secondary Comparison Datasets

- *The two higher energy X-ray bins (2000eV - 5000eV and 5000eV - 8000eV)* from the Chandra X-ray data, extracted as described above.
- *A Sunyaev-Zel'dovich effect map from Plagge et.al. (2010 [41])*. This is a map of the SZE temperature decrement in μK , measured using the South Pole Telescope. Based on [41], σ_i is taken to have a constant value of $25 \mu\text{K}$. Earlier data from Halverson (2009 [70]) was used initially, but the higher resolution Plagge data has proven more useful.
- *Radio halo measurements at 1.3 GHz from Liang et.al. (2000 [71])*. This dataset is a digitized version of the map in Figure 5 from [71]. No attempt is made to assign a σ_i value for this dataset. More recently, higher resolution data from Shimwell et.al. (2014 [72]) has become available and is being

examined.

Plots of each of the six datasets are shown in Figure 3.2. Comparisons of these datasets to the corresponding simulation predictions, are shown in the following sections.

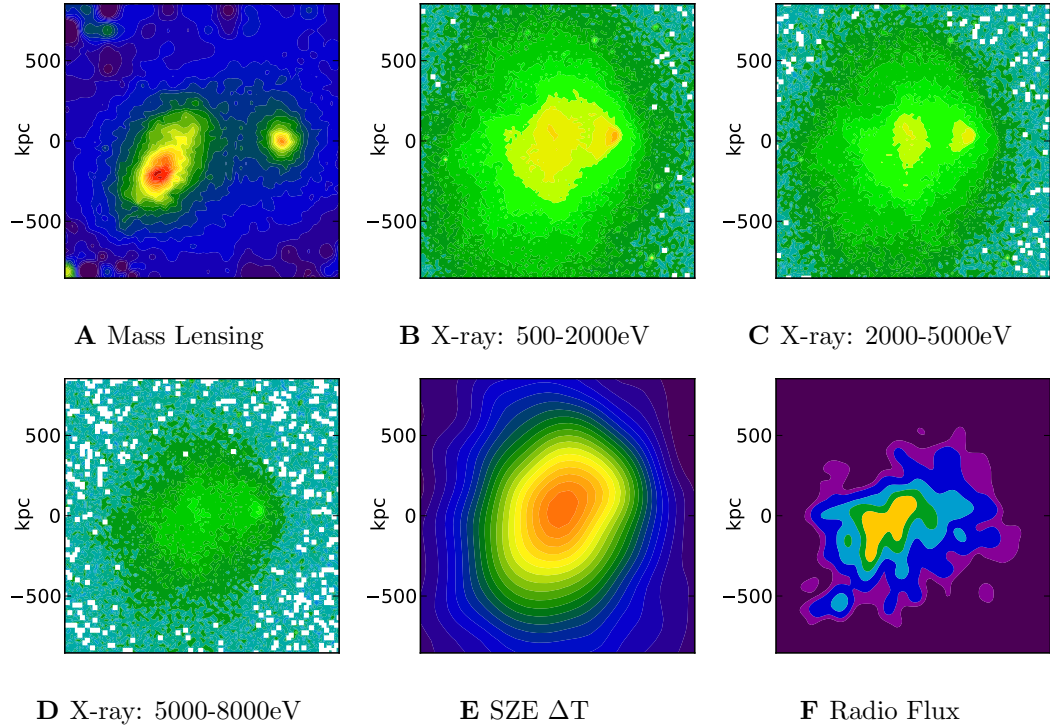


Figure 3.2: The six observational datasets.

3.2 Software Tools

A number of different software tools are used in this study. These include tools for generating the initial clusters, tools for simulating the actual collision, and tools for analyzing the results of the simulation. The Table 3.1 gives a high-level overview of these software tools. The methods by which these tools are employed to generate the simulation results are detailed in the subsequent sections.

Generating Initial Clusters		
Tool	Purpose	Source
SMILE	Generation of stable DM halos	Vasiliev [73]
TriaxialHalo	Generation of stable baryon profiles	Lage (this work)
CombineGalaxies	Combines and aligns multiple clusters	MPA (Springel, private)
GarFields	Generation of random B-field	MPA [74]
Simulation of Collision		
Tool	Purpose	Source
Gadget	Simulation of Collision	MPA [75]
Enzo	Simulation of Collision	UCSD [76]
Run scripts	Python scripts for automatically running the simulation, analyzing the results, and launching new simulations	Lage (this work)
Analyzing Results		
Tool	Purpose	Source
APEC	Calculation of plasma X-ray emissivity	Chandra [69], [77]
YT	Analysis of AMR output	Turk, et.al. [1]
Findfom	Python scripts for calculating χ^2 and other observables	Lage (this work)

Table 3.1: Summary of Software Tools

3.2.1 Simulation Conditions

For the simulation of the actual collision, we evaluated two simulation tools, Gadget (Springel 2005 [75]), an SPH code, and Enzo (Bryan 2013 [76]), a grid-based

hydrodynamics code with adaptive mesh refinement (AMR). Both simulators use discrete particles for the dark matter, but differ in the simulation of the hydrodynamics. The two simulators were found to give similar results, but ultimately, the Enzo simulator was chosen when the need for incorporation of MHD into the simulations became apparent. A summary of the key simulation conditions is shown in Table 3.2.

Parameter	Value	Units
Simulation Volume	12000 x 6000 x 6000	kpc
Coarse Grid	128 x 64 x 64	-
Maximum Number of Refinement Levels	6	-
Minimum Grid Cell Size	5.8	kpc
Total Number of Grid Cells	3.2E6	-
Maximum Baryon Mass per Grid Cell	2.5E8	M_{\odot}
Number of DM Particles	5.0E6	-
Mass of DM Particles	1.5E8	M_{\odot}
Hydro Method	Runge Kutta 3rd-order MUSCL w/ Dedner MHD	-
Cosmology	Flat, Static	-

Table 3.2: Enzo simulation conditions.

3.3 Methods

This section describes the methods used for generating the initial clusters, simulating the actual collision, and analyzing the results of the simulation.

3.3.1 Generation of Initial Conditions and Fitting Parameters

The simulations begin with two widely separated galaxy clusters, each in a state of dynamic equilibrium, approaching each other on a collision course. For clarity, in what follows we will refer to the larger cluster as the main cluster, and the smaller cluster as the bullet cluster. In the images, the bullet cluster initially approached the main cluster from the left, but has now passed through the main cluster and is currently on the right. The major challenge in obtaining a simulation which produces a good fit to the observations lies in choosing appropriate initial conditions.

In the first stage of this effort we used spherically symmetric clusters. This gave an approximate fit to the observations, but as our understanding increased we came to appreciate that some features of the system are most likely due to initial cluster triaxiality. We find that initial clusters with a triaxial shape give a much better fit to the data, although this introduces additional variables. With tens of thousands of measurements to fit, these additional parameters are in fact quite well constrained. The procedures used to generate stable triaxial clusters with an NFW dark matter profile and a flexible baryon profile are described below.

3.3.1.1 Fitting Parameter Overview

We use a total of 34 fitting parameters, as listed in Table 3.3 and described below, to model the collision. The meaning of these parameters, the method for obtaining the optimum parameter values, and the method for estimating the uncertainties are discussed in detail in the following sections.

Fitting Parameters with Best Fit Values				
Dark Matter Halo Parameters				
Parameter	Description	Value	Sigma	Units
M ₁	Main Cluster Mass (M ₂₀₀)	1.91E15	0.20E15	M _⊕
M ₂	Bullet Cluster Mass (M ₂₀₀)	2.59E14	0.31E14	M _⊕
C ₁	Main Cluster Concentration	1.17	0.14	-
C ₂	Bullet Cluster Concentration	5.45	0.70	-
P ₁	Main Cluster Z/X Axis Ratio	0.35	0.05	-
Q ₁	Main Cluster Y/X Axis Ratio	0.68	0.09	-
P ₂	Bullet Cluster Z/X Axis Ratio	0.61	0.08	-
Q ₂	Bullet Cluster Y/X Axis Ratio	0.68	0.10	-
Gas Profile Parameters				
Parameter	Description	Value	Sigma	Units
GF ₁	Main Cluster Gas Fraction	0.19	0.02	-
GF ₂	Bullet Cluster Gas Fraction	0.17	0.02	-
RC ₁₁	Main Cluster Gas Radius1	59.4	7.9	kpc
RC ₁₂	Bullet Cluster Gas Radius1	19.8	1.9	kpc
β ₁₁	Main Cluster Exponent1	0.38	0.06	-
β ₁₂	Bullet Cluster Exponent1	0.51	0.07	-
RC ₂₁	Main Cluster Gas Radius2	69.9	11.4	kpc
RC ₂₂	Bullet Cluster Gas Radius2	47.8	6.4	kpc
β ₂₁	Main Cluster Exponent2	0.45	0.05	-
β ₂₂	Bullet Cluster Exponent2	0.85	0.14	-
RC ₃₁	Main Cluster Gas Radius3	647	82	kpc
RC ₃₂	Bullet Cluster Gas Radius3	465	80	kpc

Fitting Parameters with Best Fit Values				
Gas Profile Parameters - Cont.				
Parameter	Description	Value	Sigma	Units
β_{31}	Main Cluster Exponent3	0.67	0.05	-
β_{32}	Bullet Cluster Exponent3	0.50	0.06	-
Orbital Geometry Parameters				
ϕ_1	Main Cluster Euler Angle 1	185	33	Degrees
θ_1	Main Cluster Euler Angle 2	38.4	5.9	Degrees
ψ_1	Main Cluster Euler Angle 3	221	30	Degrees
ϕ_2	Bullet Cluster Euler Angle 1	164	23	Degrees
θ_2	Bullet Cluster Euler Angle 2	100	14	Degrees
ψ_2	Bullet Cluster Euler Angle 3	65.0	10	Degrees
IP	Impact Parameter	256	35	kpc
V _{Inc}	Infall Velocity Increment	-10.9	15	%
Remaining Parameters				
Parameter	Description	Value	Sigma	Units
Z	Metallicity (Cooling)	0.78	0.10	Solar
Mag	Peak Magnetic Field Magnitude	61.0	5.4	μ G
f _{ntp}	Non-Thermal Pressure factor	0.52	0.09	-
Visc	Viscosity	0.12	0.02	Spitzer

Table 3.3: Best fit parameters determined from the simulations, as well as an estimate of the uncertainties. The determination of the uncertainties is described in Section 3.3.4

3.3.1.2 Dark Matter Halos

For the dark matter halos, we assume that each of the initial clusters is described by a triaxial NFW profile (Navarro, Frenk, White 1996 [26]; Lee and Suto 2003 [78]), with dark matter surfaces of constant density being a set of concentric ellipsoids, as follows:

$$\rho_{\text{DM}} = \frac{\rho_{\text{DM}0}}{\frac{R}{R_C}(1 + \frac{R}{R_C})^2}. \quad (3.2)$$

Here the radial parameter R is given by:

$$R^2 = x^2 + \frac{y^2}{Q^2} + \frac{z^2}{P^2}, \quad (3.3)$$

where P and Q are the triaxiality axis ratios. As discussed earlier, we take $P \leq Q \leq 1$, meaning that the x -axis is the long axis and the z axis is the short axis. Each ellipsoid is then rotated to its initial orientation, as described later. The parameters $\rho_{\text{DM}0}$ and R_C are related to the virial radius R_{200} , the concentration parameter C , the mass within the virial radius M_{200} , and the critical density ρ_{CRIT} at redshift z as described in equations 2.5, 2.6, and 2.7. There are thus a total of eight parameters to describe the two clusters: the mass M_{200} , the concentration parameter C , and the shape parameters P and Q , for each of the two clusters.

3.3.1.3 Baryonic Distributions

Following Lee and Suto (2003 [78]), we make the physically reasonable assumption that the density and temperature of the baryonic plasma are constant along surfaces of constant gravitational potential. We find that correctly fitting the X-Ray emission data depends critically on the gas profiles of the initial clusters. For this reason, we assume a flexible three-slope gas density profile, as follows:

$$\rho_G = \frac{\rho_{G0}}{(1 + (\frac{R}{R_{C1}})^2)^{\beta_1}(1 + (\frac{R}{R_{C2}})^2)^{\beta_2 - \beta_1}(1 + (\frac{R}{R_{C3}})^2)^{\beta_3 - \beta_2}}, \quad (3.4)$$

where the parameter R is given by $R^2 = x^2 + y^2/Q(R)^2 + z^2/P(R)^2$, with $P(R)$ and $Q(R)$ the (slowly varying) shape parameters of the equipotential ellipsoids. As described in detail in Binney and Tremaine (2008 [79]), the equipotential ellipsoids defined by $P(R)$ and $Q(R)$ are aligned with the density ellipsoids, but they are more spherical than the density ellipsoids and become more spherical still as one moves out from the cluster center.

The central density parameter ρ_{G0} is adjusted so that the ratio of baryonic mass to total cluster mass within R_{200} is equal to an assumed gas fraction parameter GF. This parameter GF is then taken as a fitting parameter for each cluster. For given plasma and dark matter densities, the plasma temperature required for hydrostatic equilibrium is determined by evaluating the following integral for the particle internal energy

$$u(R) = \frac{3}{2\rho_G(R)} \int_R^{R_{\max}} \frac{\partial \varphi}{\partial R'} \rho_G(R') dR'. \quad (3.5)$$

Since the plasma temperature is assumed constant along the equipotential ellipsoids, it is sufficient to evaluate this integral along the x-axis of the cluster, and use the resulting value all along the equipotential surface intersecting that axis at R .

There are thus 14 parameters needed to describe the baryonic matter distributions: the gas fraction parameter GF and three pairs of (R_C, β) parameters, for each of the two clusters.

3.3.1.4 Cluster Generation Procedure

To combine these dark matter and gas profiles into a stable cluster we use the following procedure:

- We choose the cluster mass, concentration parameter, and triaxiality parameters. These parameters fix the mass density, and hence the gravitational potential of the cluster.
- We generate a stable dark matter halo using the Schwarzschild procedure[80]. This procedure involves assuming a randomly chosen initial position and velocity for each of a set of trial dark matter particles within the given potential, then calculating the orbit followed by each particle. The density distribution which results from each particle following the calculated orbit is then determined. A set of linear equations is solved to calculate the weight to be given to each of the trial particles in order to reproduce the original, assumed mass density distribution. The dark matter particle initial positions and velocities are distributed along these orbits. For these studies we use a total of 50,000 initial orbits, and several million dark matter particles (see Table 3.2). We utilize a software package called SMILE from Vasiliev (2012 [73]), for carrying out the Schwarzschild procedure, and we find it to be very successful at generating stable triaxial halos. A computationally more efficient method has recently been proposed by Yurin and Springel (2014 [81]), but we have not yet evaluated this.
- We choose the parameters specifying the cluster baryon fraction (gas fraction) and the gas density profile.

- Given the potential profile and the gas density profile, we calculate the gas temperature profile using Equation 3.5.
- After each cluster is generated, we rotate it to an assumed orientation, specified by a total of six Euler angles, three for each cluster.

This procedure does involve an approximation, since the cluster gravitational potential is assumed set by the dark matter halo, whereas the cluster also contains a significant amount of baryonic matter. In principle, we could iterate the procedure, calculating the potential due to the combined dark matter and baryonic mass distribution. However, since the shape of the baryonic matter distribution is not too different from the shape of the dark matter distribution (see Figure 4.5A), we find that it is sufficient to use the shape of the potential determined by the dark matter profile, but use the full cluster mass (dark matter + baryons) to set the magnitude of the potential. Because the mass distribution profiles are similar, and the cluster mass is dominated by the dark matter, the error involved in this assumption is small and this procedure gives stable clusters. We demonstrate the stability of clusters created by this procedure in Figures 3.3 and 3.4, which show that a representative cluster is stable on a gigayear timescale. Figure 3.3 shows the stability of the cluster shape, and Figure 3.4 shows the stability of the cluster profiles.

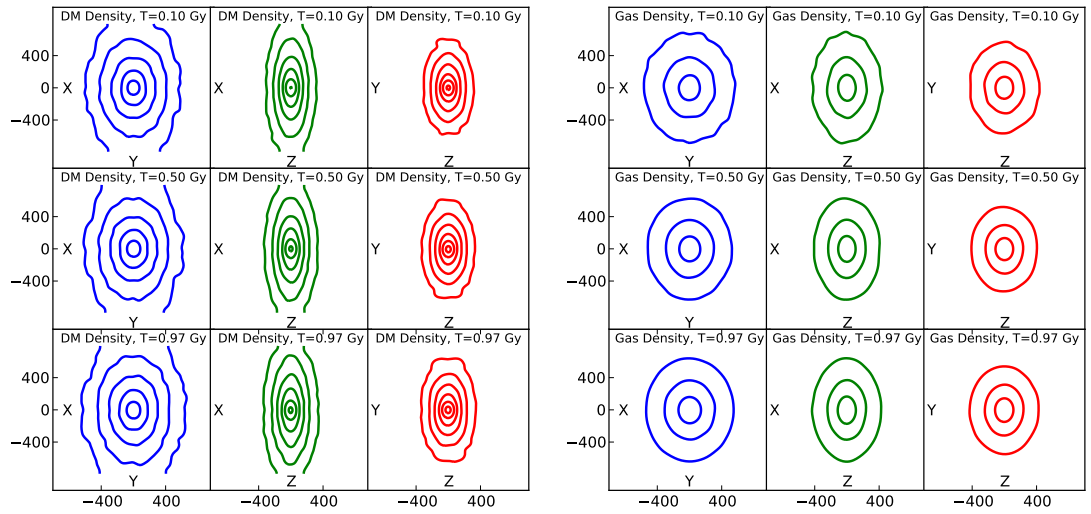


Figure 3.3: Shape stability of a triaxial cluster with $P = 0.35$ and $Q = 0.70$

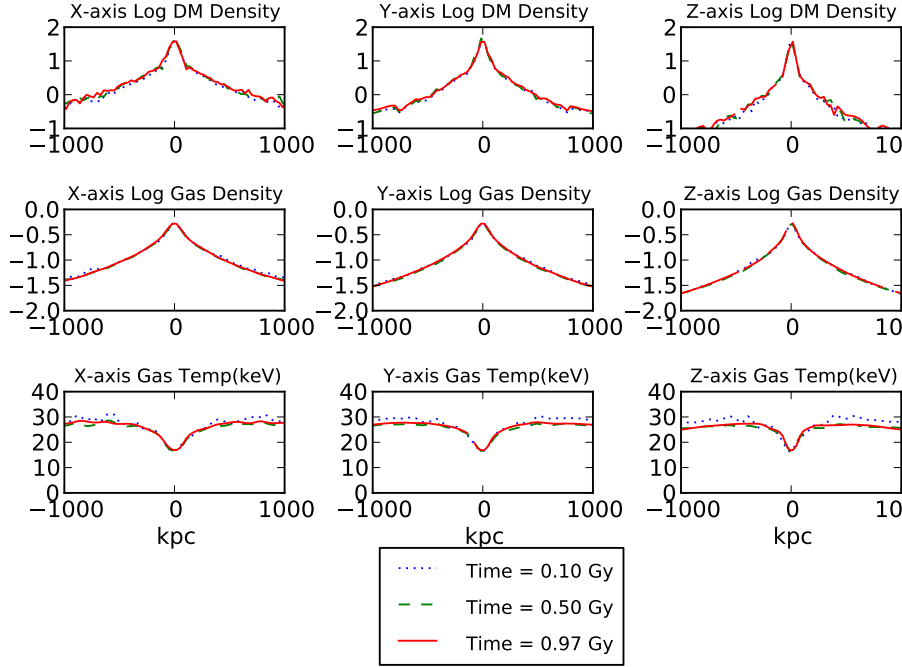


Figure 3.4: Profile stability of a triaxial cluster with $P = 0.35$ and $Q = 0.70$. Note that the temperatures plotted are effective temperatures, as discussed in Sections 3.3.1.7 and 4.1.3

3.3.1.5 Initial Positions and Velocities

The two initial triaxial clusters are assumed to fall in from infinity on a near-radial trajectory. We begin the simulation when the virial radii of the two clusters make contact. Figure 3.5 shows a density slice near the beginning of the simulation. The initial velocities are controlled by two free parameters: the initial impact parameter of the two cluster mass centroids and a radial velocity percent increment over and above the velocity acquired while free-falling from infinite separation. These are referred to as IP and Vinc respectively in Table 3.3. We find the best fit value of Vinc to be about 10 percent less than unity, indicating that the clusters were initially bound, and also showing that large initial velocities are not required

to reproduce the observations.

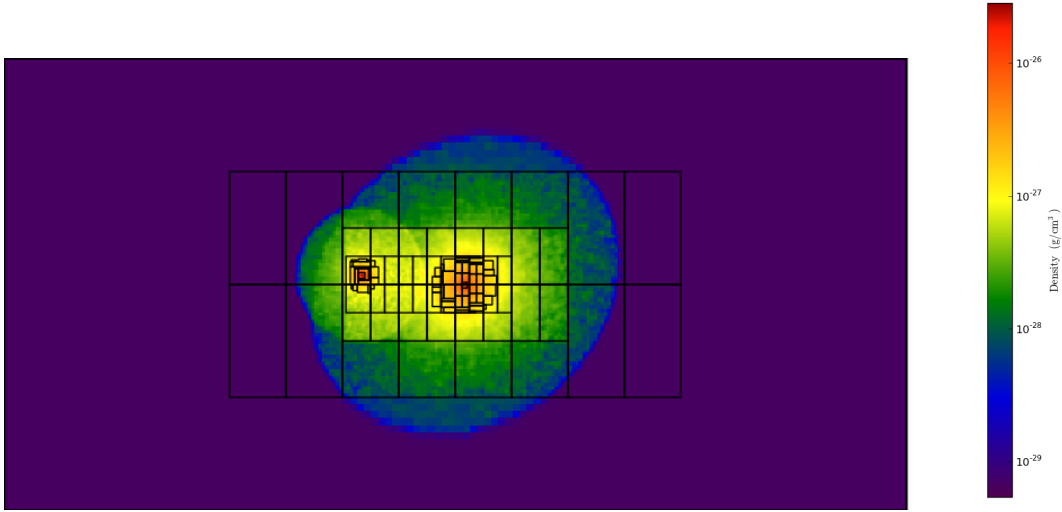


Figure 3.5: This graph shows a typical baryon density slice near the beginning of the simulation. The black boxes show the initial mesh distribution. The size of the region shown is 12.0 x 6.0 Mpc.

3.3.1.6 Magnetic Field

We set the initial magnetic field configuration of the two clusters as follows:

- We generate each of the three components of the Fourier-transformed B -fields $\hat{B}_x, \hat{B}_y, \hat{B}_z$ as a Gaussian random field with a Kolmogorov spectrum ($\hat{B}_i \propto k^{-5/3}$). The minimum and maximum possible k values for the initial random field configuration are given by:

$$k_{\max} = \frac{2\pi}{L} * \frac{N}{2} \quad k_{\min} = k_{\max}/4, \quad (3.6)$$

where L is the box length, which is 6 Mpc in these simulations, and N is the number of cells in the x -direction of the largest (coarsest) grid, which is

128. Due to the adaptive mesh refined MHD, turbulence on smaller scales is generated as the simulation progresses. An important physical question is what maximum coherence length characterizes the initial field configuration. Only a few values have been tried in this first analysis. The best of them is presented here; it has an initial maximum coherence length equal to four times the initial coarsest grid spacing, i.e., about 180 kpc. Future work will explore how well the B-field configuration can be constrained, but this must be done in conjunction with developing a physical understanding the non-thermal pressure, discussed in the next section.

- We clean the divergence in k-space by forcing $\mathbf{k} \cdot \hat{\mathbf{B}} = 0$.
- We then Fourier transform the B-field components back to real space. All of the above steps are performed with the aid of the GarFields software package (Kitaura 2008 [74]).
- This generates a B-field of uniform magnitude throughout the simulation volume, whereas we expect the field to be stronger in regions of higher plasma density. In a simple collapse model of a magnetized sphere, the density scales as $1/r^3$ and the magnetic field scales as $1/r^2$. We therefore scale the initial B-field magnitude so that $|B| \propto \rho_{gas}^{2/3}$. Note that the scaling factor is applied after the two clusters are combined into a single simulation file, so the same scaling factor (relationship between $|B|$ and ρ_{gas}) is used for both clusters. This spatial scaling of the uniform Kolmogorov B-field introduces a slight non-zero value of $\nabla \cdot \mathbf{B}$. We have verified that, because the length scale of the plasma density variation is much longer than the scale of B-field fluctuations, removing this $\nabla \cdot \mathbf{B}$ has negligible impact on the simulations, so we do not

do this routinely. Quantitatively, $|\nabla \cdot \mathbf{B}|/|\mathbf{B}|$ has a value of between 10^{-3} and 10^{-4} kpc^{-1} , and this value is basically unchanged by cleaning the divergence, indicating that this quantity is probably limited by discretization errors.

The only fitting parameter associated with the initial magnetic field configuration is thus an overall scale for the field magnitude, referred to as Mag in Table 3.3. This parameter is the peak magnetic field magnitude in the region of highest density in the initial configuration, which proves to be at the center of the bullet cluster.

3.3.1.7 Non-Thermal Pressure

In this simulation study we have attempted to calculate as many of the observables as possible from first principles, minimizing the number of “fudge factors”. However, we do find it necessary to include such an adjustable parameter to adequately describe the non-thermal pressure. The source of this non-thermal pressure is currently unknown, although turbulent fluid motions and/or cosmic ray pressure appear to be the most likely explanations. Thus, following Bode (2012 [82]), we phenomenologically incorporate non-thermal pressure into this simulation using a single, space- and time-independent parameter, f_{ntp} , as follows:

$$P_{\text{tot}} = P_{\text{th}} + P_{\text{ntp}} = P_{\text{th}} \left(1 + \frac{f_{\text{ntp}}}{1 - f_{\text{ntp}}}\right) = P_{\text{th}} \frac{1}{1 - f_{\text{ntp}}}. \quad (3.7)$$

In effect, the simulation is performed with an effective temperature which is higher than the actual temperature in order to account for the increased pressure, then the effective temperature is reduced by the scaling factor when calculating X-ray flux and the associated plasma cooling. This is a relatively primitive way

of including non-thermal pressure and will be improved in future work. Further discussion can be found in Section 4.1.3 where the predictions from the simulation are discussed, and Section 4.5, where we discuss potential improvements to this model.

3.3.1.8 Other Fitting Parameters

The remaining fitting parameters are:

- The metallicity parameter Z (defined as a fraction of solar metallicity), which controls both the rate of cooling and the plasma X-ray emission, as discussed in Section 3.3.2.2
- The viscosity parameter, Visc , which adds a viscosity as a fraction of Spitzer viscosity.

3.3.2 Calculation of Observables

In order to compare the simulation to the observables, we need to calculate the observables that result from a given set of initial conditions. This section describes the procedures used to calculate the observables from the simulation variables.

3.3.2.1 Lensing Mass

Calculation of the lensing mass for comparison to the lensing data is straightforward. The baryon mass is a conserved quantity in the simulation, while the dark matter consists of discrete particles of fixed mass. We sum the dark matter and baryon mass separately along the line of sight for each pixel, then add the two together to give the total lensing mass. From the standpoint of this calculation,

stars are indistinguishable from dark matter. This should be a good approximation because the stellar mass accounts for only a few percent of the total baryonic mass in extremely massive clusters (Gonzalez 2013 [24]).

3.3.2.2 Calculation of X-ray Flux

The temperature range of the gas in galaxy clusters is typically in the keV range. At these temperatures, thermal bremsstrahlung is the largest component of the X-ray flux. In early work, we assumed that the X-rays were only generated through thermal bremsstrahlung, and we review the method for performing those calculations. The X-ray luminosity (energy emitted per unit volume per unit time per unit frequency interval) is given by: (Rybicki and Lightman 2004 [83])

$$\frac{dW}{dVdt d\nu} = \frac{32\pi e^6}{3m_e c^3} \sqrt{\frac{2\pi}{3m_e k_B T}} Z^2 n_e n_i e^{-\frac{\hbar\nu}{k_B T}} \quad (3.8)$$

$$\frac{dW}{dVdt d\omega} = \frac{16}{3} \frac{e^2}{\hbar c} \frac{e^4}{m_e^2 c^4} m_e c \sqrt{\frac{2\pi}{3m_e k_B T}} Z^2 n_e n_i e^{-\frac{\hbar\omega}{k_B T}} \quad (3.9)$$

$$\frac{dW}{dVdt d\omega} = \frac{16}{3} \sqrt{\frac{2\pi}{3}} \alpha r_e^2 \hbar c \sqrt{\frac{m_e c^2}{k_B T}} Z^2 n_e n_i e^{-\frac{\hbar\omega}{k_B T}} \quad (3.10)$$

Where α is the fine struture constant and r_e is the classical electron radius. The total energy emitted is obtained by integrating this over all frequencies:

$$\frac{dW}{dVdt} = \frac{16}{3} \sqrt{\frac{2\pi}{3}} \alpha r_e^2 \hbar c \sqrt{\frac{m_e c^2}{k_B T}} Z^2 n_e n_i \int_0^\infty e^{-\frac{\hbar\omega}{k_B T}} d\omega = \frac{16}{3} \sqrt{\frac{2\pi}{3}} \alpha r_e^2 c \sqrt{m_e c^2 k_B T} Z^2 n_e n_i \quad (3.11)$$

The total X-ray emission is proportional to $n_e n_i \sqrt{T}$, as is well known. This \sqrt{T} behavior is commonly used to calculate the X-ray emission from the plasma, but it is only correct to do so if all of the energy emitted is observed, which is not

the case here. Also, in the Chandra data we are counting photons, so we need to convert this to the number of photons emitted per unit volume per unit time per unit energy bin, which is:

$$\frac{dN}{dVdt dE} = \frac{16}{3} \sqrt{\frac{2\pi}{3}} \frac{\alpha r_e^2 c}{E} \sqrt{\frac{m_e c^2}{k_B T}} Z^2 n_e n_i e^{-\frac{E}{k_B T}} \quad (3.12)$$

Now since we compare to photons in a given energy bin, we need to integrate over the energies being collected, where E_{\min} and E_{\max} are the minimum and maximum energies at the detector, which of course have been redshifted from their emission. Doing this gives the following expression(note that z is the redshift and Z is the mean atomic number), where E_1 is the exponential integral

$$E_1(\xi) = \int_1^\infty \frac{e^{-\xi t} dt}{t} \quad (3.13)$$

$$\frac{dN}{dVdt} = \frac{16}{3} \sqrt{\frac{2\pi}{3}} \alpha r_e^2 c \sqrt{\frac{m_e c^2}{k_B T}} Z^2 n_e n_i \left(E_1 \left(\frac{E_{\min}(1+z)}{k_B T} \right) - E_1 \left(\frac{E_{\max}(1+z)}{k_B T} \right) \right) \quad (3.14)$$

For the temperatures and energies applicable for the bullet cluster collision, this has a very different functional form from the \sqrt{T} behavior, and is nearly flat with temperature. One final adjustment is the addition of the Gaunt factor, which is a quantum mechanical correction to the classical bremsstrahlung. Tabulated Gaunt factors (see for example Itoh, 2002 [84]) for astrophysical plasmas at these temperatures are in the range of 1.2-1.4. After adding the Gaunt factor, the calculated X-ray luminosity is given by the following equation, and plotted in

Figure 3.6.

$$\frac{dN}{dVdt} = GF \frac{16}{3} \sqrt{\frac{2\pi}{3}} \alpha r_e^2 c \sqrt{\frac{m_e c^2}{k_B T}} Z^2 n_e n_i (E_1 \left(\frac{E_{\min}(1+z)}{k_B T} \right) - E_1 \left(\frac{E_{\max}(1+z)}{k_B T} \right)) \quad (3.15)$$

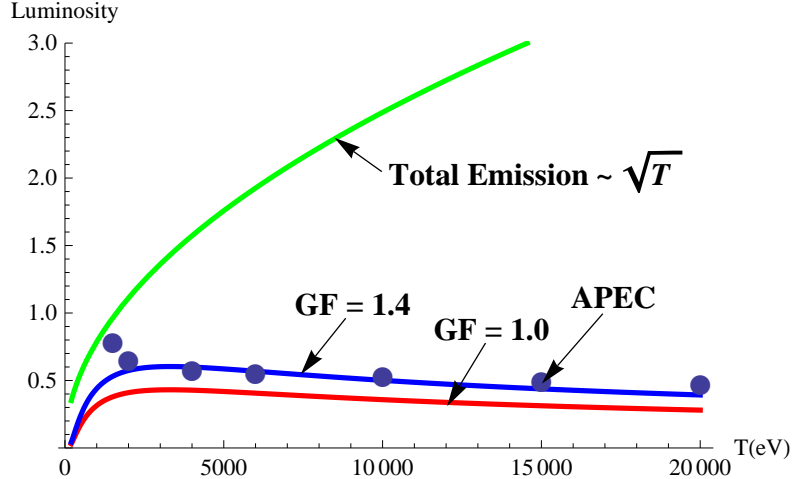


Figure 3.6: This shows the calculated emissivity in photons/(cm³s) due to thermal bremsstrahlung for a plasma with temperature given on the X-axis. The green curve is the total emissivity at all energies, which has a \sqrt{T} dependence. The blue and red curves show the emissivity between 500 eV and 6000 eV, which corresponds to the Chandra sensitivity. The red curve has a Gaunt factor of 1.0, and the blue curve has a Gaunt factor of 1.4. The blue points are the emissivity calculated using the APEC code [69], which includes all emission, not just bremsstrahlung. The blue curve with a Gaunt factor of 1.4 (Equation 3.15) is a good fit to the total emission for plasma temperatures above a few keV.

While the assumption of bremsstrahlung only is seen to be a good assumption at higher temperatures, Figure 3.6 shows that it significantly underpredicts the plasma emissivity at lower temperatures. To improve the accuracy of the simulation,

we modified the code to include both thermal bremsstrahlung and line emission, which is a complex function of temperature and metallicity. To do this, we use the APEC code (Frusciaone 2006 [69]) to build a look-up table of the plasma emissivity in each energy bin (with the energy bin limits blue-shifted back to the source appropriately) as a function of temperature and metallicity; the resulting emissivity is shown in Figure 3.7. Since the plasma is optically thin, we calculate the total flux by summing the flux from each volume element along the line of sight. As discussed above, the calibrated Chandra data is the flux of X-ray photons in photons/(cm²sec) in the given band of energies.

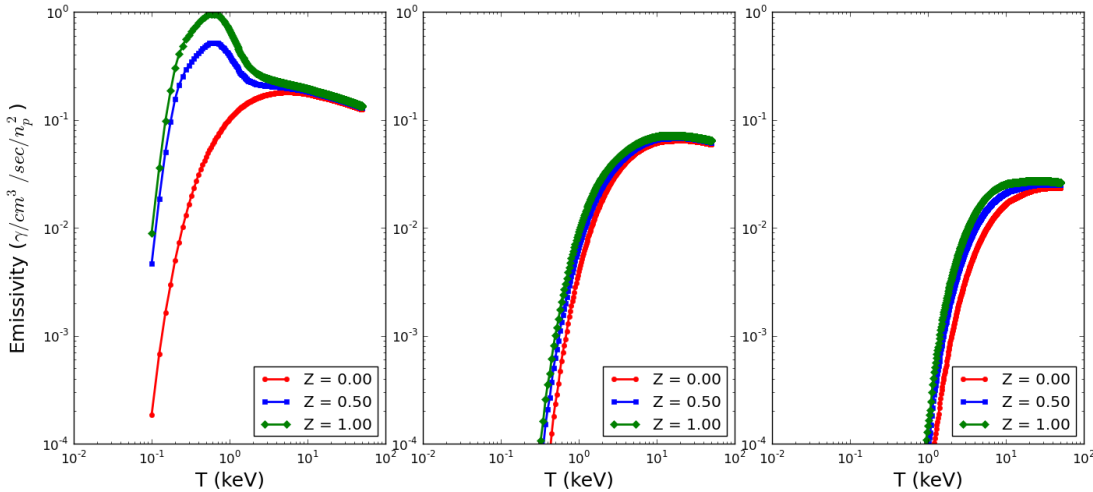


Figure 3.7: Plasma emissivity in photons/cm³/s/(n_p²) where n_p is the plasma mass density, as calculated using the APEC code for different metallicity choices. The metallicity Z is given as a fraction of solar. The left, center, and right plots are for energy bins of 500eV - 2000eV, 2000eV - 5000eV, and 5000eV - 8000eV, respectively.

We use the same calculation of plasma emissivity to calculate the rate of gas

cooling during the simulation by building a look-up table that gives the cooling rate as a function of temperature and metallicity. This is done by slightly modifying the Enzo code to use this look-up table instead of the built-in cooling calculation. Because emission at all energies contribute to the plasma cooling, we sum the X-ray emissivity across all energies for this cooling calculation.

3.3.2.3 Plasma Temperature

Calculation of a 2D map of the plasma temperature to compare to observed temperatures is not trivial, since both the plasma density and the plasma temperature vary along the line of sight. Observational determination of the plasma temperature is a difficult problem (Vikhlinin 2005 [23]; Govoni 2004 [85]; Nagai 2007 [86]). In principle a spectroscopic temperature should be used (Mazzotta 2004 [87]), where the X-ray flux is integrated along the line of sight, and the resulting spectrum fit with a temperature for each pixel, but this is computationally expensive. We find that an X-ray emission weighted temperature gives almost the same result, and is much faster, so we use this procedure to produce the temperature maps (for example, Figure 4.8A). In other words, we calculate the temperature in each pixel by

$$T = \frac{\int_{\zeta_{\min}}^{\zeta_{\max}} T(\zeta) * \epsilon(n_p(\zeta), T(\zeta), Z) d\zeta}{\int_{\zeta_{\min}}^{\zeta_{\max}} \epsilon(n_p(\zeta), T(\zeta), Z) d\zeta}, \quad (3.16)$$

where the integration is along the line of sight, ζ_{\min} , ζ_{\max} are the boundaries of the simulation volume, and the plasma emissivity $\epsilon(n_p, T, Z)$ is calculated as described above. We use E_{\min} and E_{\max} values of 500 eV and 8000 eV for this purpose. We emphasize that these temperature maps are not used for optimization or calculation of χ^2 , but only for comparison purposes.

3.3.2.4 Calculation of S-Z Effect

Inverse Compton scattering of CMB photons by the hot plasma leads to a distortion of the CMB blackbody spectrum. A good approximation for optically thin, non-relativistic plasmas such as these is that the distortion results in a slight modification of the CMB temperature as given by the following equation [88]:

$$\frac{\Delta T}{T_{\text{CMB}}} = -2\sigma_T \int \frac{k_B T(\zeta)}{m_e c^2} n_e(\zeta) d\zeta. \quad (3.17)$$

Here the integration is along the line of sight, and σ_T is the Thomson scattering cross section. Since the X-ray flux is proportional to n_e^2 and is relatively independent of T , and the SZE ΔT is proportional to $n_e T$, the two datasets together allow an independent determination of plasma density and temperature. For the Bullet Cluster, the S-Z effect has a maximum ΔT of approximately $400\mu\text{K}$.

3.3.2.5 Radio Halo

Galaxy clusters, especially those undergoing violent collisions, are known to have extended radio halos. The source of the radio emission is less well understood than the source of the X-ray emission, but is believed to be a population of relativistic electrons which emit synchrotron radiation as they spiral around the cluster magnetic field lines (Govoni 2004 [89]; Liang 2002 [90]; vanWeeren 2011 [91]). Following closely Rybicki and Lightman (2004 [83]), we use the following model:

- The population of relativistic electrons follows a power law distribution (we assume $p > 2$):

$$N(\gamma) d\gamma = C \gamma^{-p} d\gamma. \quad (3.18)$$

- The population of relativistic electrons is in equipartition with the magnetic field, meaning that:

$$\int_0^\infty \gamma m_e c^2 C \gamma^{-p} d\gamma = \frac{B^2}{8\pi}. \quad (3.19)$$

This implies:

$$C = \frac{(p-2)B^2}{8\pi m_e c^2}. \quad (3.20)$$

With these assumptions, the intensity of radio emission depends only on the magnetic field intensity B and the power law exponent p , which we assume constant throughout the simulation volume. After averaging over the randomly oriented direction of the magnetic field, the radio power is given by:

$$P(\nu) d\nu = \frac{\sqrt{3\pi}}{32\pi^2(1+z)} \frac{e^3 B^3}{(m_e c^2)^2} f(p) \left(\frac{2\pi m_e c \nu (1+z)}{3eB} \right)^{-(p-1)/2} d\nu, \quad (3.21)$$

where the function $f(p)$ is given by the following expression:

$$f(p) = \frac{(p-2)}{(p+1)} \frac{\Gamma(\frac{p+5}{4})}{\Gamma(\frac{p+7}{4})} \Gamma(\frac{p}{4} + \frac{19}{12}) \Gamma(\frac{p}{4} - \frac{1}{12}); \quad (3.22)$$

$f(p) \approx 0.3$ for typical values of p ($2.5 < p < 4.0$). For comparing to observations, it is important to note that the spectral index of the electron energy, p , (Equation 3.18) is related to the spectral index of radio emission, s ,

$$f(\nu) d\nu = C \nu^{-s} d\nu, \quad (3.23)$$

by the following equation [83]:

$$s = \frac{p-1}{2}. \quad (3.24)$$

We find the power law exponent to be tightly constrained to a value of $p \approx 3.6$, as discussed in Section 4.1.4.

3.3.2.6 Calculation of Rotation Measure

Electromagnetic radiation propagating through an ionized plasma experiences a rotation of the plane of polarization, an effect known as Faraday rotation. The amount of rotation is proportional to the electron density times the component of magnetic field parallel with the direction of propagation, as follows (Rybicki and Lightman 2004 [83]):

$$\Delta\theta = \frac{e^3 \lambda^2}{2\pi(m_e c^2)^2} \int_{\zeta_{\min}}^{\zeta_{\max}} n_e(\zeta) * B_{||}(\zeta) d\zeta, \quad (3.25)$$

where the integration is along the line of sight, and $\zeta_{\min}, \zeta_{\max}$ are the boundaries of the simulation volume. It is usual to define the *Rotation Measure*, with units of radians/m² as:

$$RM = \frac{\Delta\theta}{\lambda^2}, \quad (3.26)$$

so that:

$$RM = \frac{e^3}{2\pi(m_e c^2)^2} \int_{\zeta_{\min}}^{\zeta_{\max}} n_e(\zeta) * B_{||}(\zeta) d\zeta, \quad (3.27)$$

This is used in generating Figure 4.13.

3.3.3 Optimization Procedure

For a given choice of parameters, we build the appropriate initial clusters and simulate the collision process using the Enzo simulator as described in the preceding sections. As the simulation progresses, the full state of the system is recorded

at time steps of 0.01 Gy in the relevant range of time. The simulation is run in a frame with the initial cluster velocities in the x-direction, and the initial impact parameter in the y-direction, so there are two angular variables ($\theta_{\text{obs}}, \psi_{\text{obs}}$) which determine how our viewing angle is related to the simulation coordinates. For each time value T, a search is run through these viewing angles and the observables are calculated as described in Section 3.3.2. This generates a set of 2D images (one for each observable) for each set of values $(T, \theta_{\text{obs}}, \psi_{\text{obs}})$. These then need to be aligned to the observations in the plane of the sky, requiring three more variables $(\Delta X, \Delta Y, \phi_{\text{obs}})$. The values of $(\Delta X, \Delta Y, \phi_{\text{obs}}, \theta_{\text{obs}}, \psi_{\text{obs}})$ which minimize the calculated χ^2 value are determined for each value of T. (After the initial conditions are approximately determined, this entire procedure only needs to be carried out for a limited time-range.) Figure 3.8 shows the typical evolution of the χ^2 parameter through simulation time. The observations are best described after approximately 0.85 Gy have elapsed since the beginning of the simulation. The time of closest approach of the mass centroids is at 0.73 Gy after the start of the simulation, so approximately 120 My have elapsed since the time of closest approach.

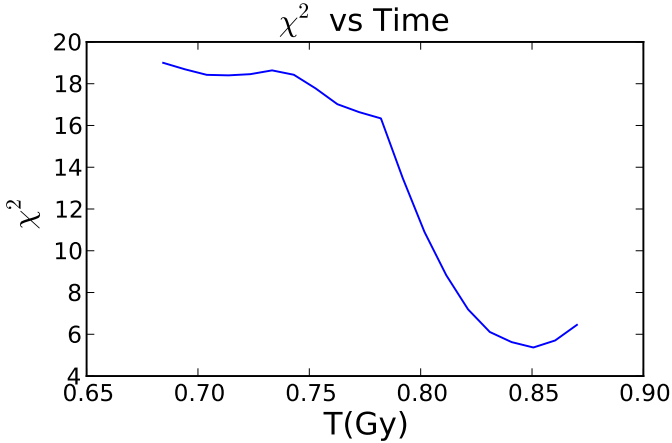


Figure 3.8: Typical evolution of the χ^2 parameter (for the best fit viewing angle and position in the plane of the sky) as the simulation progresses.

We run simulations exploring the space of initial conditions and other parameters to find those which minimize the χ^2 parameter. These simulations are run on the NASA Pleiades supercomputer cluster, with each simulation running for about 8 hours of wall clock time. About 10% of this time is in setting up the initial conditions and analyzing the result. The remainder is spent in running the Enzo simulation, typically using 64 CPUs. The space of possible initial conditions is too large to carry out a fully systematized parameter optimization procedure, such as performing a Markov-Chain-Monte-Carlo. Instead, Monte-Carlo searches are run within generously selected ranges of parameters, with steepest-descent optimizations to find the locally-best fits for several of the best points in parameter space, supplemented by judicious by-hand exploration of parameter space to make sure no minima are overlooked. No sampling procedure can absolutely guarantee one is near the global rather than just a local minimum for χ^2 , the strong constraints the data imposes make it likely that the best-fit initial conditions reported

here are close to a global optimum, for the adopted model treatment. In all, more than 1000 simulations were run in order to find the best fit initial conditions and their uncertainties given in Table 3.3.

There is some degree of decoupling in the parameter space. The mass lensing projection is primarily determined by the dark matter distribution, and hence is mostly determined by the shapes and orientations of the dark matter halos, which are controlled by the parameters labeled “Dark Matter Halo Parameters” and “Orbital Geometry Parameters” in Table 3.3. To most efficiently find the global minimum, the optimization strategy we follow is first to optimize these parameters with a χ^2 calculated only from the mass lensing data, then optimize the remaining parameters with a χ^2 calculated from both the mass lensing data and the lowest energy X-ray flux, and finally to optimize on the full parameter set with a χ^2 calculated from both the mass lensing data and the X-ray flux data.

3.3.4 Statistics

To estimate the uncertainty associated with the parameters determined from the optimization, one would ideally perform a Markov Chain Monte Carlo (MCMC) analysis of the simulation model in the multi-dimensional space of initial conditions. However, the minimal such MCMC analysis for a system such as ours involves running tens or hundreds of thousands of trials, and the simulation is too computationally expensive to allow this. The strategy we use is to run a smaller number of trials, build an approximate model of χ^2 in the multi-dimensional parameter space, then characterize the parameter distributions using this model. This procedure is described in more detail in Blizniouk, et.al. (2008 [92]), where it is shown to give distributions similar to that which result from running an MCMC

analysis on the original computationally expensive simulation.

Simulations are run using a range of initial conditions, and a χ^2 value is calculated for each. Some of these simulation runs (approximately 700) are part of the χ^2 -minimization runs, and some (approximately 300) are run with intentionally varied parameters in order to span the space of input parameters. Many of these simulations are run with the lower resolution conditions described in Section 4.3. We then use the results of these simulation runs to build a multi-dimensional cubic-spline Radial Basis Function (RBF) model of χ^2 as a function of the input parameters. This RBF model fits the simulated points exactly, and varies smoothly as one moves away from the simulated points.

Figure 3.9 shows plots of the RBF model as two typical parameters move away from the optimum point with all other parameters held fixed. The RBF model, which is computationally easy to evaluate, is then used to estimate the uncertainties of the parameters, defined so that the region within 1-sigma on either side of the best-fit value of a given parameter contains 34% of the probability density after marginalizing over all other parameters. The sigma values which result are tabulated in Table 3.3.

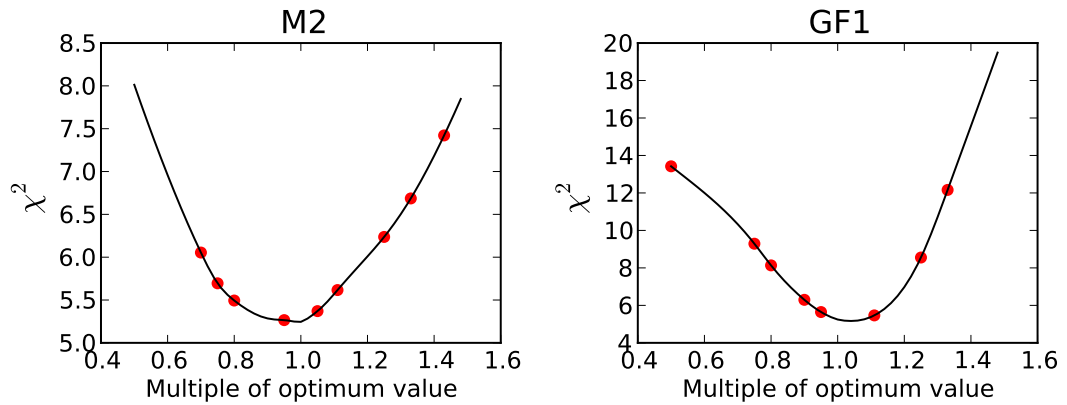


Figure 3.9: Behavior of the Radial Basis Function model as two representative parameters M2(Bullet Cluster mass) and GF1(Main Cluster gas fraction) are varied around the optimum point, with all other parameters held fixed. The RBF model is the black lines, and the actual simulations are the red circles.

Chapter 4

Results and Major Findings

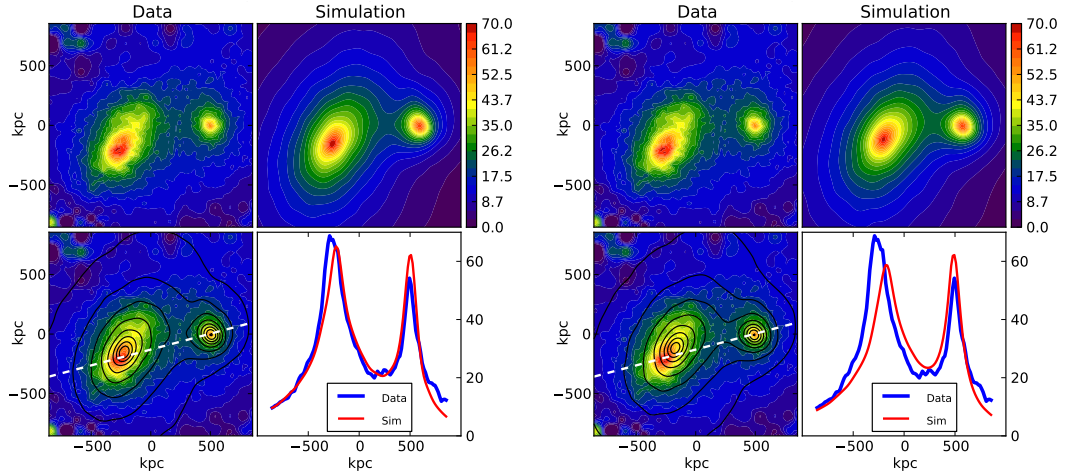
This section discusses the major results of our study. We first compare the best-fit simulation to the observables, then discuss the cosmological implications, then discuss some initial work toward improving the simulation.

4.1 Comparison of Best Fit Simulation to Observations

Following the procedures in the preceding sections leads to the best fit initial conditions summarized in Table 3.3. This section discusses a series of images which exemplify the fit between the optimized simulation and the observations. We begin with results which are governed mainly by the initial conditions on the dark matter and the constraints from mass-lensing data. Then we turn to the more “gastrophysics”-dependent aspects.

4.1.1 Mass Lensing

Figure 4.1A shows the predicted mass-lensing map when parameters are optimized using χ^2 calculated only from the mass lensing data, showing that the model is quite successful at reproducing the mass lensing distributions. The initial cluster triaxiality reproduces the shapes of the clusters quite well, and the value of $\chi^2 = 1.15$ obtained shows a good fit to the observations. For comparison, Figure 4.1B shows the fit of the same simulation with a χ^2 calculated from both the mass lensing data and the lowest energy X-ray flux. Since Figure 4.1A and Figure 4.1B are from the same simulation (using the parameters in Table 3.3), only the alignment to the observational data is different between these two figures. The value of $\chi^2 = 2.04$ obtained in Figure 4.1B shows that the quality of the fit using only mass lensing data is degraded slightly when the alignment is chosen to give the best simultaneous fit including the X-ray flux as described below.



A Fit achieved with χ^2 calculated from mass lensing data only. Mass only $\chi^2 = 1.15$.
B Fit achieved with χ^2 calculated from mass lensing data and lowest-energy X-ray flux data. Mass lensing contribution to $\chi^2 = 2.04$.

Figure 4.1: Mass lensing fit between the data and the simulation. In each of these plots, the measured data is in the upper left and the simulated result, on the same scale, is in the upper right. The lower left shows an overlay of the measured data and the simulation, with the simulation shown as black contour lines, and the lower right shows the measured data and simulation along a line through the 2D data planes chosen to pass approximately through the measured peaks; this slice is shown as a dotted white line in the lower left.

Figure 4.1.1 shows the collision as viewed from our perspective, and is intended to help visualize the orientations of the cluster ellipsoids. The best-fit relative velocity vector between the bullet cluster and the main cluster is inclined approximately 10 degrees to the plane of the sky. This best fit radial velocity has the bullet cluster dark matter centroid receding from us at 837 km/sec relative to the main cluster dark matter centroid. This is to be compared with the radial velocity analysis of Barrena, et.al.(2002 [93]), who found that the bullet subcluster galaxies

have a velocity offset of 616 ± 80 km/sec relative to the main cluster galaxies in the main cluster's rest frame. Our simulation makes a prediction for the distribution of velocities and their variances as a function of position in the sky, so a more detailed comparison to the current full dataset is warranted to determine whether the discrepancy (about 2.7σ with the Barrena et.al. errors) is significant.

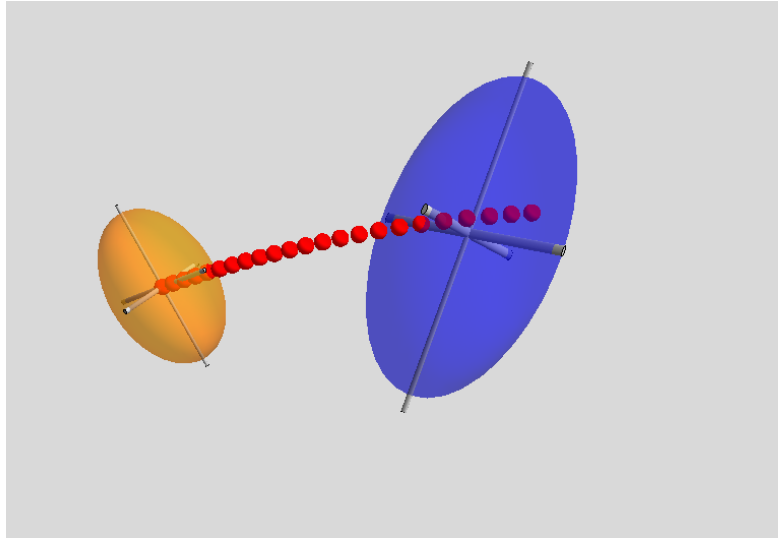


Figure 4.2: The path of the collision, as seen in the plane of the sky, illustrating the initial orientations of the two ellipsoids. The red dots indicate the path of the dark matter centroids.

4.1.2 X-ray Flux

Simultaneously fitting the mass lensing data and the X-ray flux data is more difficult than fitting the mass lensing alone, which is not surprising given the complexity of the baryonic physics and possible systematic errors in the mass lensing reconstruction. Figures 4.3A - 4.3C show the fit to the X-ray fluxes in the

three different energy bins. Figure 4.4A shows the X-ray flux from different slices through the system, on a log scale, and Figure 4.4B shows the location of the shock; these two plots are intended to show how well we have captured the location and shape of the shock. The fit is reasonable, and in particular Figure 4.4A shows that the X-ray flux is well modelled over more than 2 orders of magnitude. However, the χ^2 calculated only from the lowest energy X-ray data has a value of 5.68, so this fit is not nearly as good as the mass lensing fit.

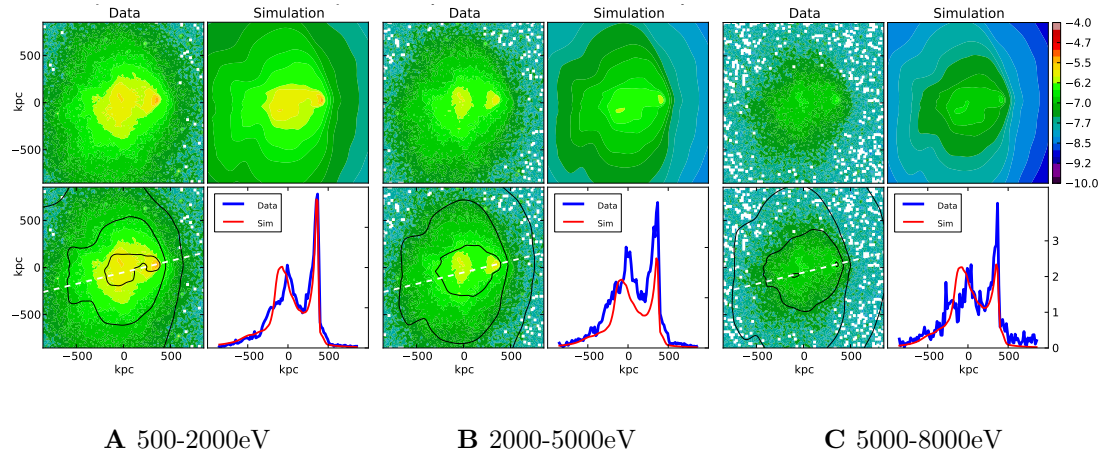


Figure 4.3: Best fit result for the X-ray flux.

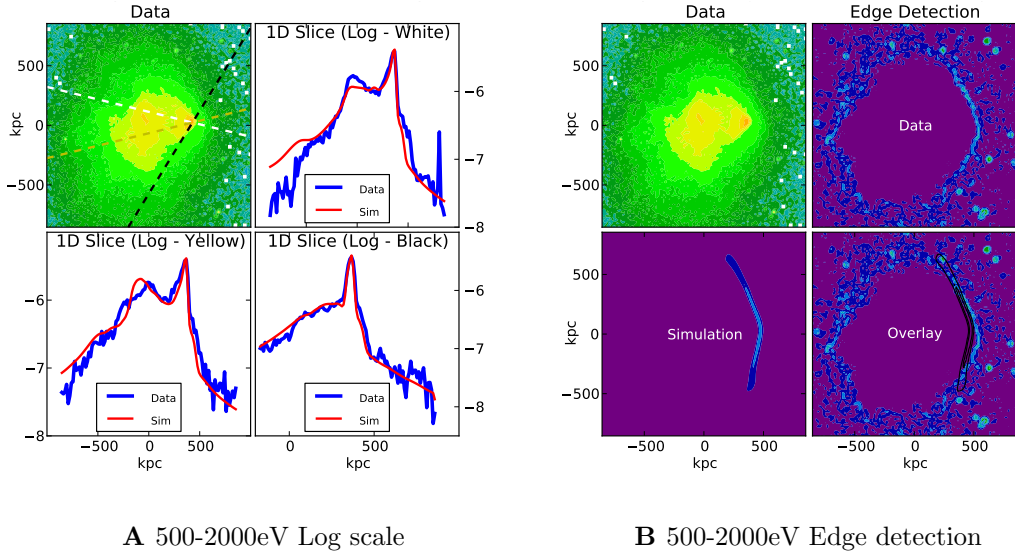
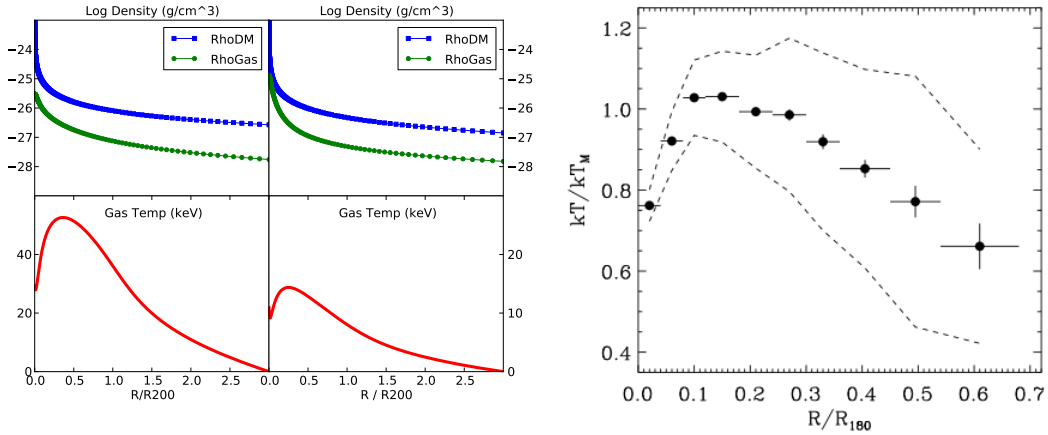


Figure 4.4: Best fit result for the X-ray flux in the range of 500-2000 eV. The left hand plot has slices on a log scale at three different angles. The right hand plot uses an edge detection algorithm to capture the location of the shock. These two plots show that the shock location and shape are reasonably well captured.

The X-ray flux morphologies are found to be quite sensitive to the details of the initial baryon distributions, and the initial distributions which give the best fit are shown in Figure 4.5A. It is important to note that the temperatures plotted here are effective temperatures including the effects of non-thermal pressure, and are therefore higher than the true temperatures, as discussed in Sections 3.3.1.7 and 4.1.3. To see whether our profiles are reasonable, we turn to the extensive measurements of single galaxy clusters which have been done, including McCourt et.al. (2012 [94]), Leccardi and Molendi (2008 [33]), and Simionescu et.al. (2011 [95]). Figure 4.5B shows measured results of cluster temperature profiles from Leccardi and Molendi, which are seen to be qualitatively similar to our initial temperature profiles.



A Baryon profiles of the two clusters; ‘main’ **B** Temperature profiles of measured clusters. cluster on the left, ‘bullet’ cluster on the right.

Figure 4.5: Initial best-fit baryon profiles of the two clusters, and comparison of our initial temperature profiles to a large sample of X-ray clusters. Figure (B) is reproduced from Leccardi and Molendi [33]; T_M is the mean cluster temperature outside $0.1 R_{180}$. Black points are the sample mean and the dotted lines are the one σ scatter. Our initial temperature profiles are qualitatively similar.

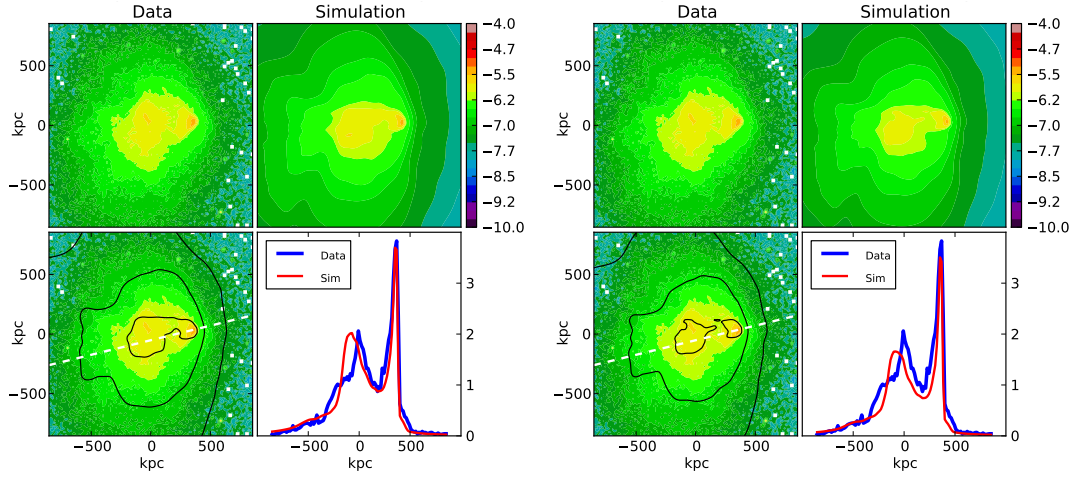
4.1.3 S-Z Effect, Plasma Temperature, and Non-Thermal Pressure

As discussed in Section 3.3.1.7, we find it necessary to explicitly include a fudge-factor to account for effects of non-thermal pressure in order to correctly describe some datasets. We describe the non-thermal pressure with a single parameter f_{ntp} which we take to be constant in space and time. Not including non-thermal pressure in the simulation has a minor impact on the X-ray flux in the 0.5-2 keV band used to constrain the parameters (see Figure 4.6), but leads to temperature and S-Z effect comparisons which are far out of agreement with the observations.

Figure 4.7A shows the S-Z effect data. Its sensitivity to the non-thermal pressure is shown in Figure 4.7B. The overall structure of the S-Z observations is well-matched, but clearly the normalization cannot be predicted with accuracy until non-thermal pressure is treated better. The offset between predicted and observed emission peaks is similar to the net offset between predicted and observed peaks in X-ray and mass lensing peaks; whether any significance can be attached to that is under study.

Figure 4.8A shows the predicted plasma temperature averaged along the line of sight in each pixel, which is compared to the map extracted from the X-ray measurements by M. Markevitch using the procedure described in (Markevitch 2000 [96]) and kindly provided to us. The temperature uncertainty is said to have a median value of 1.5 keV [private communication, 2011], but note that the extracted temperature along a given line of sight is susceptible to large variations due to Poisson statistics in the high-energy X-ray band with the result that the observational map contains a great deal of noise. Therefore, only large-scale features should be compared to the predictions. On the simulation side, non-thermal pressure is important for the high-energy X-ray band, and thus the overall scale of the temperature map is uncertain, as seen in Figure 4.8B showing the sensitivity of the temperature map to the non-thermal pressure. Nonetheless, the qualitative features of hot, low density gas leading a dense cold core are clear in the predictions and also visible as a general pattern underlying the noise in the extracted temperature map.

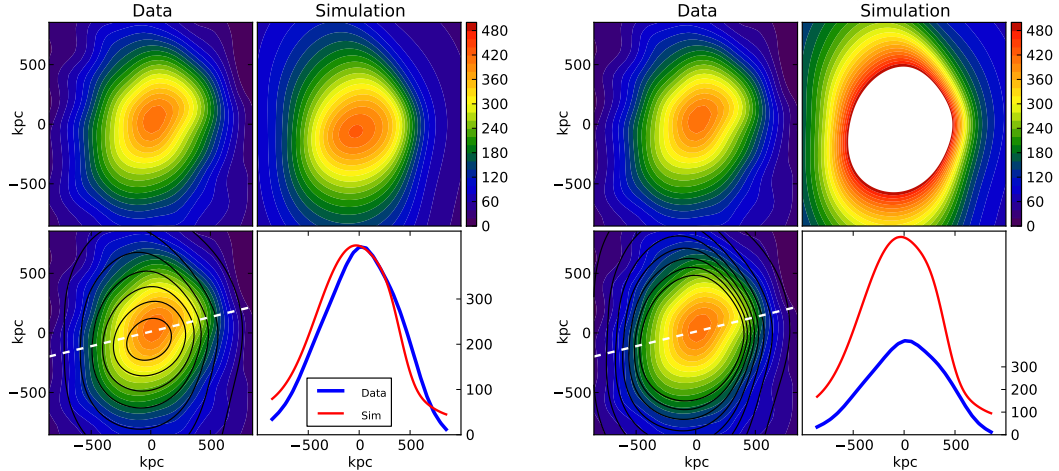
Going forward, it is clear that treating the non-thermal pressure as a constant ratio relative to the thermal pressure is too simplistic and we plan to improve our treatment, as will be discussed in Section 4.5.



A With non-thermal pressure.

B No non-thermal pressure.

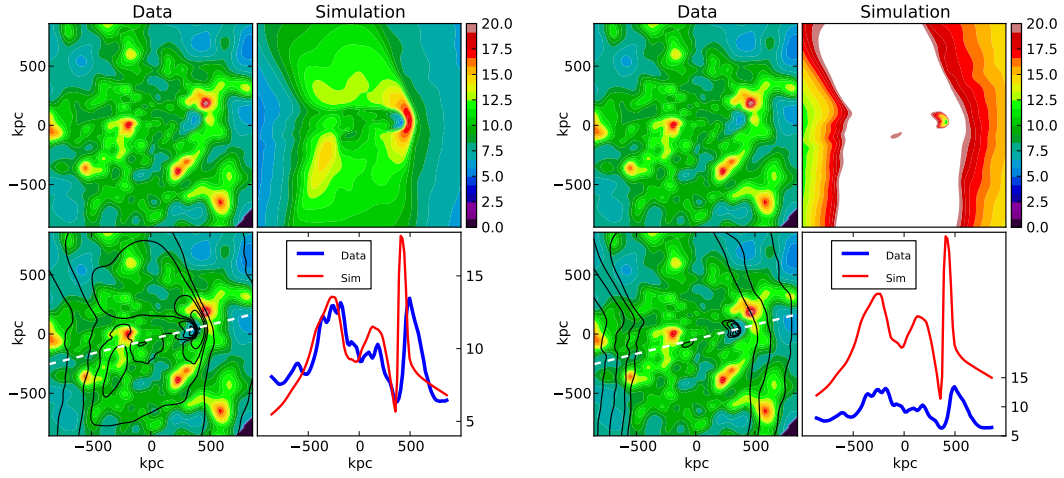
Figure 4.6: Impact of the non-thermal pressure on the X-ray flux from 500-2000 eV.



A With non-thermal pressure.

B No non-thermal pressure.

Figure 4.7: Fit results for the S-Z temperature decrement, with and without the impact of non-thermal pressure. The contour plot color saturation in Figure (b) results from ensuring all plots are on the same scale.



A With non-thermal pressure.

B No non-thermal pressure.

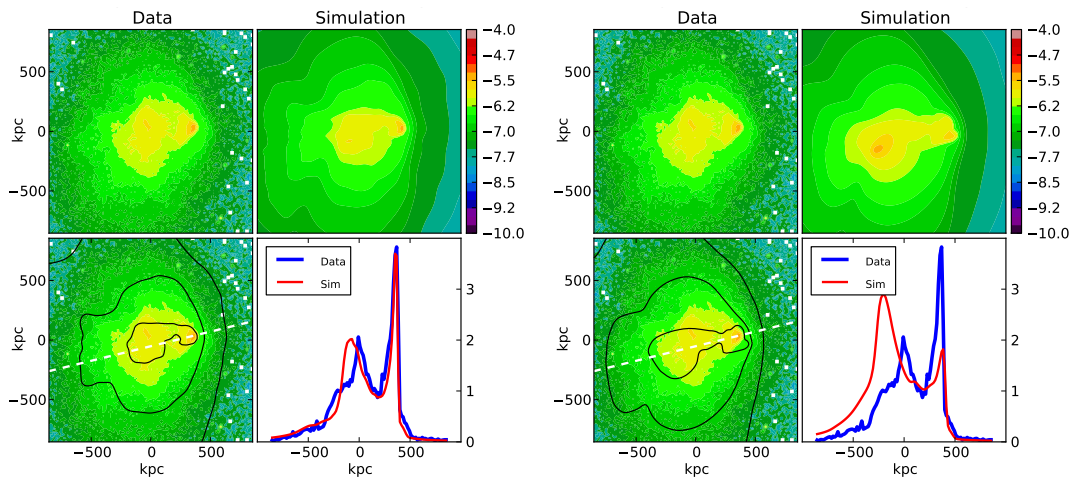
Figure 4.8: Fit results for the plasma temperature with and without the impact of non-thermal pressure. The contour plot color saturation in Figure (b) results from ensuring all plots are on the same scale.

4.1.4 Role of Magnetic Field and Radio Halo Prediction

As noted above, it is non-trivial to accurately match the mass lensing reconstruction while simultaneously accurately reproducing the X-ray flux morphology. The inclusion of magnetic fields is important for achieving a good description. Figure 4.9 shows that, given a good fit to the mass lensing distributions, the baryon density peaks (and their associated X-ray flux peaks) without the magnetic field tend to be “ahead” of their observed locations. This requires some added pressure on the baryons in order to retard the motion of the baryon density peaks to agree with the observations. We have achieved this with a combination of increased magnetic field and added viscosity, both of which retard the motion of the baryon peaks. Attempts to achieve alignment of the various peaks with only the addition

of the magnetic field are not successful, and the addition of the viscosity term is required. Even with these components added, however, the reproduction of the shapes of the regions of high X-ray flux (see Figures 4.3A - 4.3C), while close, is still not completely accurate.

While the best-fit magnetic field found here does not play a dominant dynamical role, the details of the initial magnetic field distribution (see Section 3.3.1.6) do impact the X-ray flux results. To further explore whether the magnetic fields found here are reasonable, we calculated the radio halo emission, and compared this to the measurements of Liang et.al. (2000 [71]). As detailed in Section 3.3.2.5, we use a simple model where a population of relativistic electrons is taken to be in equipartition with the magnetic field. This population follows a power law distribution with power law exponent p (see Equation 3.18), and produces a radio flux with spectral index s (see Equation 3.23), where p and s are related by Equation 3.24. Figure 4.10 shows the fit to the radio halo data using a typical magnetic field as determined from the collision dynamics; it is to be emphasized that since the initial B-field is randomly generated, a detailed fit is not the goal: reproducing the general magnitude and location of the radio emissions is the best that can be expected. The value of the power law exponent p is fairly tightly constrained to a value of $p \sim 3.6$, as seen in Figure 4.11, which shows that this value is needed in order to reproduce the magnitude of the observed radio emissions. This predicts a value of radio emission spectral index $s \sim 1.3$, which is encouragingly close to the value of 1.2-1.3 measured by Liang.



A Mag = $61\mu G$.

B Mag = $0.01\mu G$.

Figure 4.9: Impact of magnetic field on the X-ray flux in the range of 500-2000 eV. The magnetic field pressure impacts the location of the X-ray peaks.

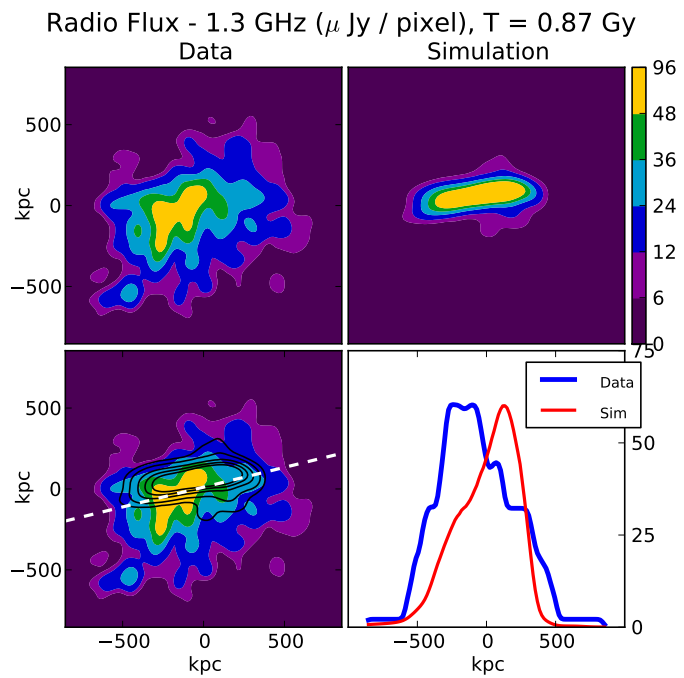


Figure 4.10: Predicted radio flux, as compared to observations by Liang, et. al.[71]
The subpanels of each plot are as described in Figure 4.1A.

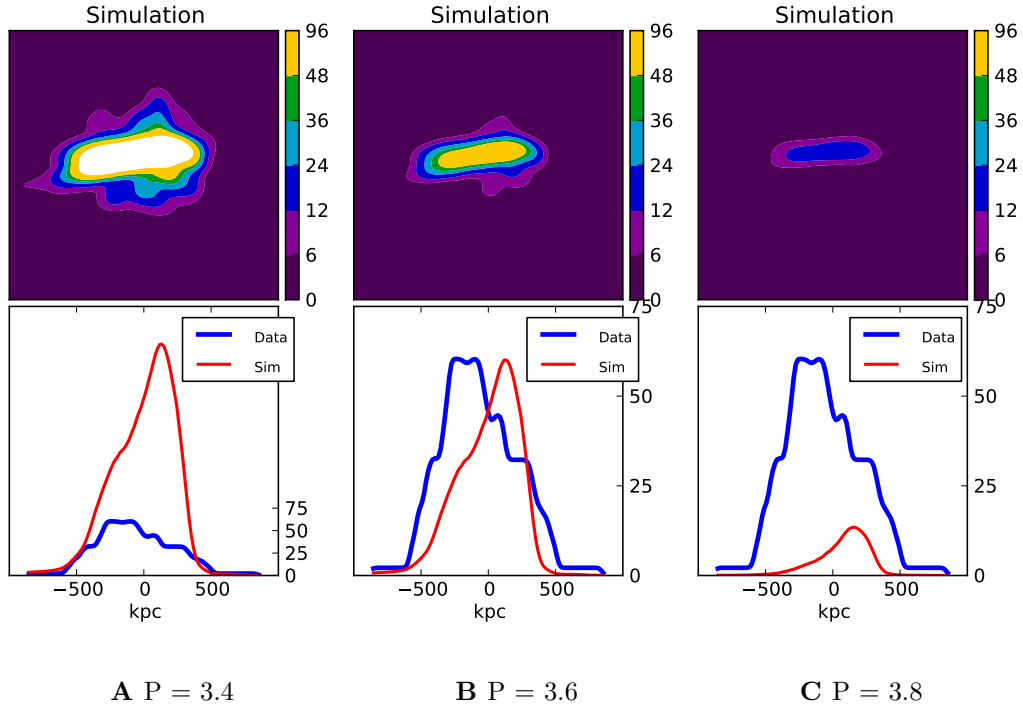
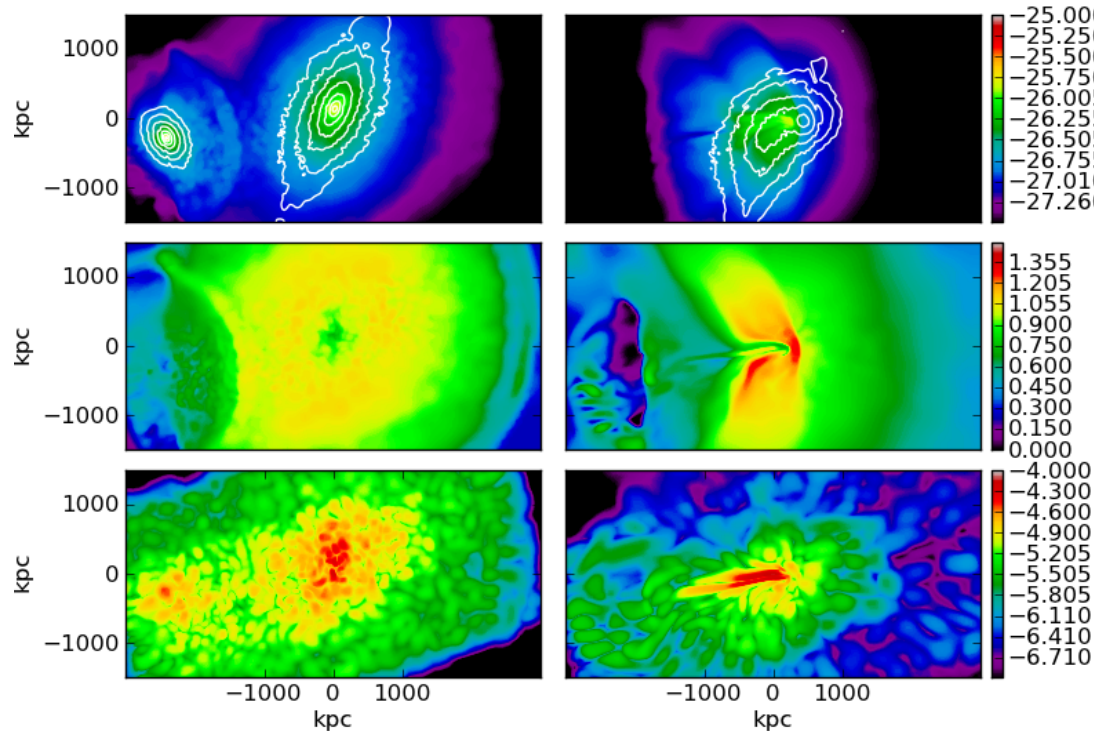


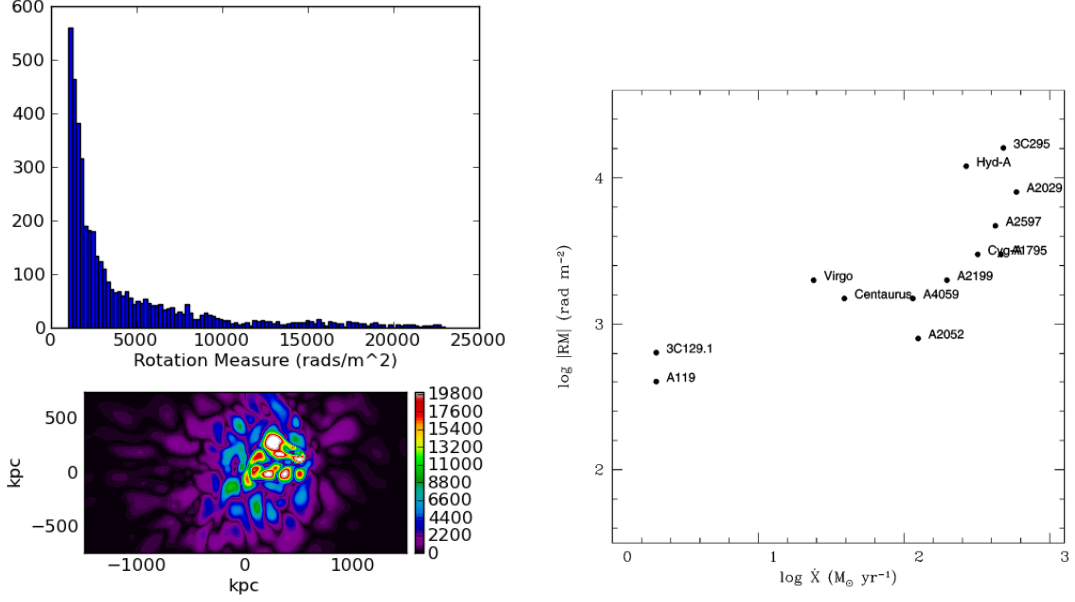
Figure 4.11: Impact of the spectral index parameter p . A value of $p=3.6$ best captures the magnitude of the radio halo flux. The contour plot color saturation in Figure (a) results from ensuring all plots are on the same scale.

Figure 4.12 shows the magnetic field amplification which takes place during the collision. The peak magnetic field increases from $\approx 60\mu\text{G}$ at the beginning of the collision to $\approx 80\mu\text{G}$ at the time of observation. These magnetic fields seem quite high, and have been called into question by several researchers. To see whether these values are reasonable, we calculated the Rotation Measure (RM) that would result from these values and compared them to measured galaxy clusters, as shown in Figure 4.13. While the RM values predicted for the Bullet Cluster are large, there exist other measured clusters with RM values on the order of 10,000 radians/m². Thus, it appears that the large simulated values of magnetic field that we find are reasonable. RM measurements of the Bullet Cluster would be invaluable for confirming the simulation results.

able in resolving this situation. The fact that the value of magnetic field which is required to give the proper alignment of the X-ray intensity peaks is consistent with the radio halo emission lends confidence to the model. Future work will explore this further to see if modifications of the initial B-field or improvements to the radio emission model (Section 3.3.2.5) can improve this fit further.



A Near the beginning of the simulation. **B** At the time of observation.
 Figure 4.12: Top panel: $\log(\text{baryon density in g/cm}^3)$ plotted in color; dark matter density overlaid in white contours. Middle panel: $\log(\text{gas temperature in keV})$. Bottom panel: $\log(|\mathbf{B}|)$ in Gauss.



A Simulated Rotation Measure (radians/m²). **B** Measured RM from Carilli and Taylor (2002 [57])

Figure 4.13: Simulated Rotation Measure as compared to Measured Clusters

4.1.5 Summary of Best Fit Results

Although the fits we have obtained are good and they are a considerable improvement over earlier attempts (see Section 4.2), it is clear that they could be improved. Figure 4.14 shows the contributions to the total χ^2 value (i.e. the residuals) over the 2D simulation plane, allowing the regions where the fit is poorest to be identified.

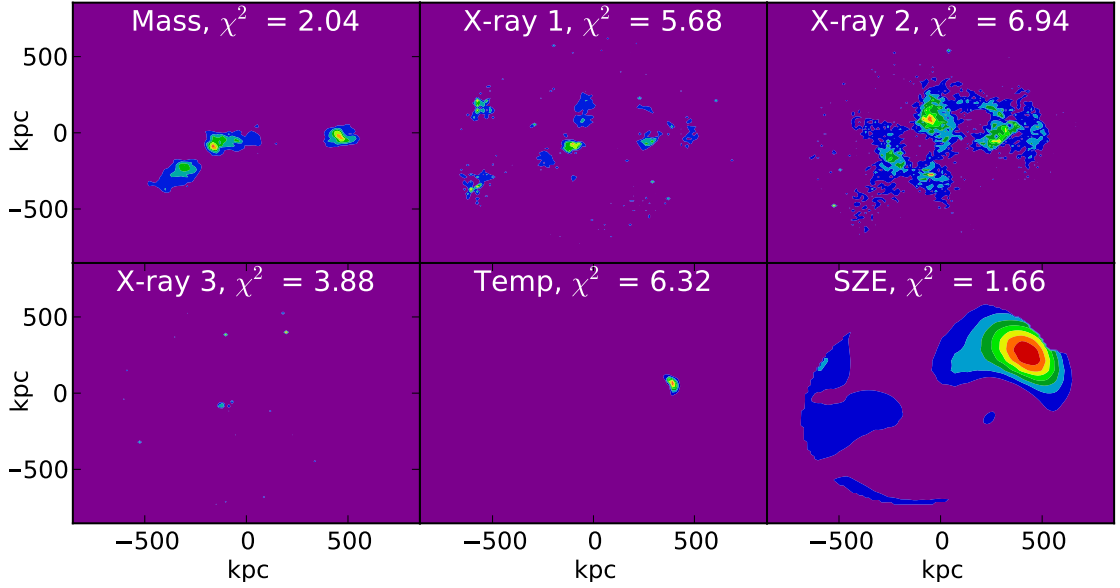


Figure 4.14: The χ^2 value calculated for each dataset alone, with the location of the regions of poorest fit (i.e. the residuals) over the 2D simulation plane shown in the colored contours.

4.2 Comparison to Past Simulation Studies

We can compare the quality of the fit achieved here to that of the earlier simulation studies of Springel and Farrar (2007 [8]) and Mastropietro and Burkert (2008 [9]). As noted in the Introduction, those studies took a different approach of trying to fit some key separations between features, and did not explore such a large range of initial conditions as we have done. Nonetheless, we can use the initial conditions reported in those papers in our simulation, and compare to the observations using our techniques. The value of the figure-of-merit parameter χ^2 calculated from mass lensing and the lowest energy X-ray data is 3.92 for our best

fit initial conditions, 13.67 for Springel and Farrar, and 19.93 for Mastropietro and Burkert. This shows the clear improvement in fitting the data that we have achieved.

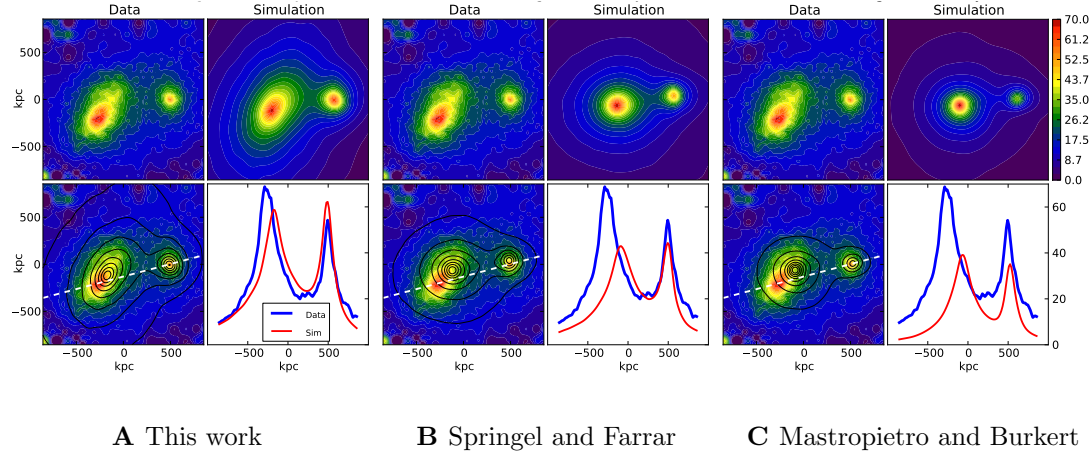


Figure 4.15: Mass lensing fits as compared to past simulation work. χ^2 calculated from mass lensing and lowest energy X-ray data as described in the text is 3.92 in this work, 13.67 for Springel and Farrar, and 19.93 for Mastropietro and Burkert.

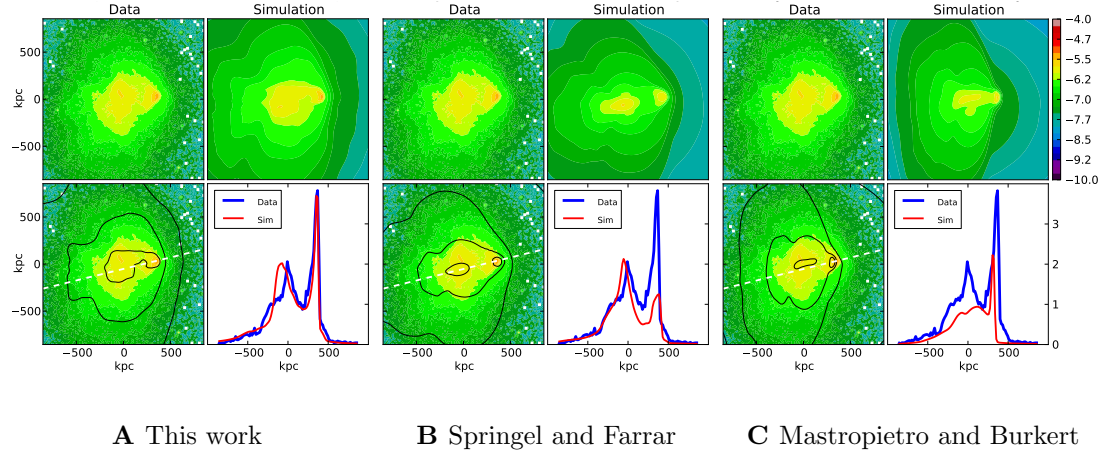


Figure 4.16: Lowest energy X-ray fits as compared to past simulation work. χ^2 calculated from mass lensing and lowest energy X-ray data as described in the text is 3.92 in this work, 13.67 for Springel and Farrar, and 19.93 for Mastropietro and Burkert.

4.3 Resolution Study

To verify that the simulations are of sufficiently high resolution to capture the main features of the cluster collision, simulations using the optimal initial conditions are run at higher and lower resolutions. For the lower resolution simulation, the number of dark matter particles is reduced by a factor of four, and the minimum grid size is increased by a factor of two. For the higher resolution simulation, the number of dark matter particles is increased by a factor of two, and the minimum grid size is decreased by a factor of two. All of these values are relative to the nominal values in Table 3.2. Figures 4.17 and 4.18 summarize the results. While there are some slight changes, especially in resolving the right-hand X-ray peak, the basic features of the simulation are unchanged, confirming that the main

conclusions are not impacted by the resolution of the simulation.

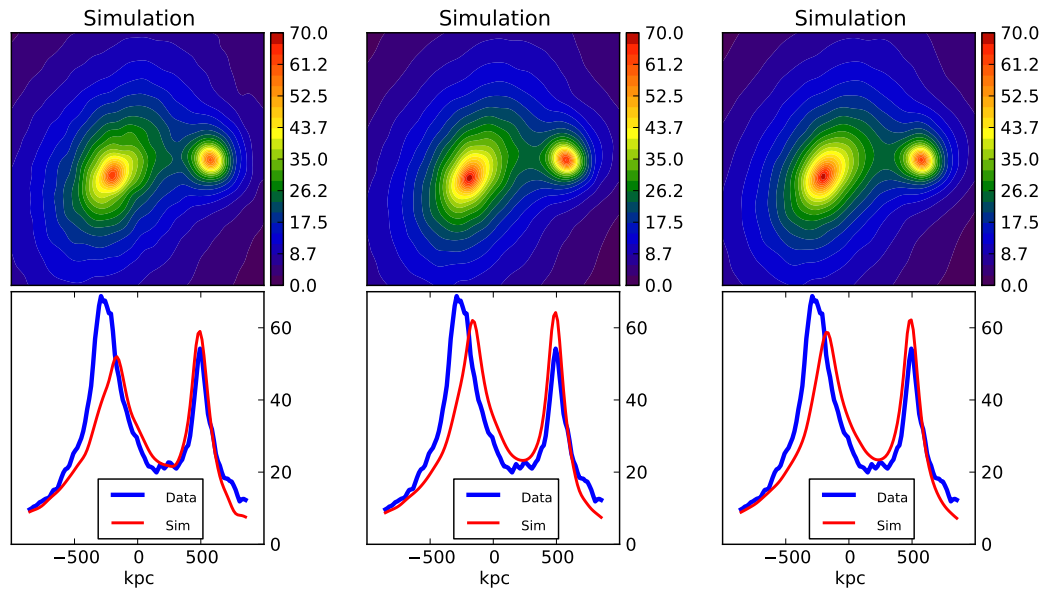


Figure 4.17: Impact of resolution on Mass Lensing fit

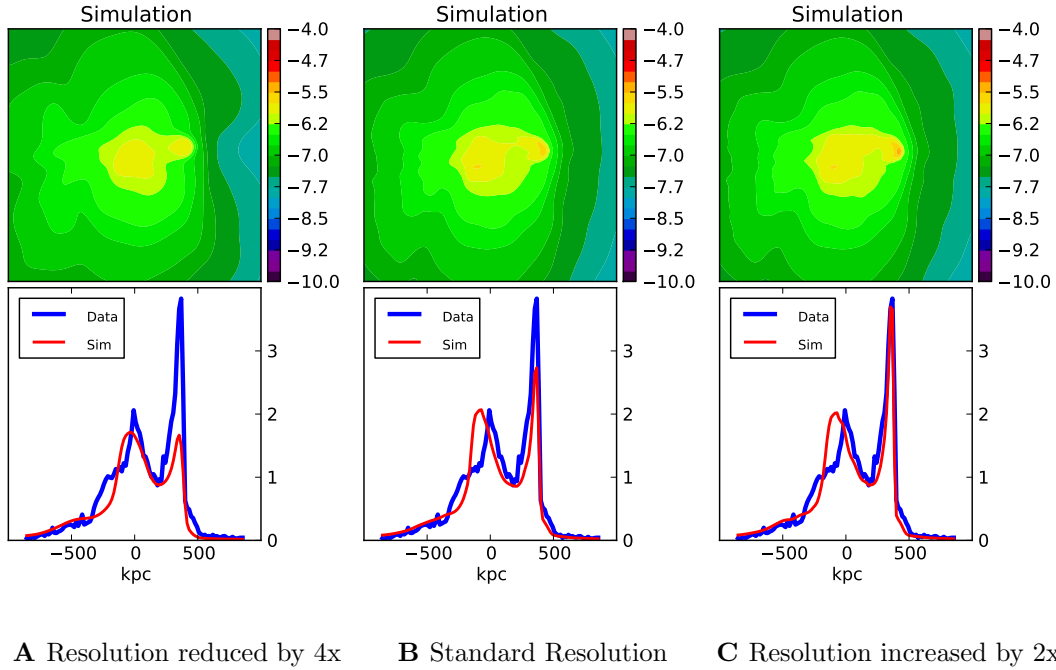


Figure 4.18: Impact of resolution on X-ray intensity fit

4.4 Cosmological Comparisons

As discussed in Section 1.2, one of the goals of this study is to clarify the disagreements on whether or not the cluster collision is consistent with the Λ CDM standard cosmological model. The fit between the observations and our simulation shown in the preceding section, while far from perfect, is remarkably good. The physics incorporated into the simulations is conventional, and the assumed initial conditions are generally quite reasonable as compared to known galaxy clusters. We find that the Bullet Cluster collision is fully consistent with Λ CDM, as discussed in this section and in a companion paper (Lage and Farrar 2014 [97]).

4.4.1 Cluster Initial Velocities

The two main simulation studies of the Bullet Cluster merger which were performed prior to this work, that of Springel and Farrar [8] and Mastropietro and Burkert [9], are discussed in Section 4.2. These studies constrain only a small number of extracted parameters, such as the location of the mass centroids and the general shape of the X-ray flux maps. Our work is a more detailed study which minimizes the chi-squared figure of merit between the two-dimensional observational data sets and the simulation. This technique greatly improves the accuracy with which the simulation matches the observations, and motivates us to revisit the question of consistency with Λ CDM. Table 4.1 shows a comparison of the cluster masses, initial cluster separations and initial infall velocities found in the various studies. To facilitate comparison, we also give a standardized initial infall velocity calculated assuming that the clusters move as point masses on a ballistic trajectory from their starting separation to a separation of 2500 kpc. Since there is very little interaction between the clusters at separations larger than 2500 kpc, assuming a ballistic trajectory of these widely separated clusters should be a very good approximation. We have also included the simulation study of Milosavljevic [10] in Table 4.1, although since it is a 2D axisymmetric simulation, it is not in the same category as the other studies. We note that a more recent study by Dawson [11] has also been performed, but since it did not include gas dynamics, it is not tabulated here.

To estimate whether the initial velocities of these simulations are consistent with a Λ CDM cosmology, we use an N-body simulation known as the Horizon Run (Kim [18]). This is a large dark-matter-only simulation using $4120^3 = 6.99 \times 10^{10}$ particles, and covering a volume of $(6.59 \text{Gpc}/\text{h})^3$. We analyze the data from this

Authors	M_{Main} (M_{\odot})	M_{Bullet} (M_{\odot})	R_{Initial} (kpc)	V_{Initial} (km/s)	V_{2500} (km/s)
Lage & Farrar	1.91×10^{15}	2.59×10^{14}	2800	2799	2943
Springel & Farrar	1.50×10^{15}	1.50×10^{14}	3370	2057	2386
Mastropietro & Burkert	7.13×10^{14}	1.14×10^{14}	5000	3000	3228
Milosavljevic et. al.	1.27×10^{15}	2.54×10^{14}	4600	0	1546

Table 4.1: Comparison of initial infall velocities from different simulation studies. For comparison, the last column gives a normalized initial infall velocity calculated assuming that the clusters move as point masses on a ballistic trajectory from their starting separation to a separation of 2500 kpc.

simulation in the following manner:

1. We start with the database of halos from the $z = 0.5$ snapshot. This database contains the masses, locations, and velocities of approximately 1.1 million halos. The $z=0$ and $z=0.5$ snapshots were available to us, and we used the $z=0.5$ snapshot since it is close to the redshift at the beginning of the simulation, which is approximately $z=0.39$.
2. For a range of target masses between $5 \times 10^{14} M_{\odot}$ and $2 \times 10^{15} M_{\odot}$, we search for a cluster within 10% of the target mass. A cluster meeting this criterion is referred to as a main cluster analog.
3. For each of these “main” clusters, we search for a neighboring cluster within a distance of 5 Mpc, with a mass between 6 times and 10 times less than the main cluster analog. A cluster meeting these criteria is referred to as a bullet cluster analog.
4. We extract the relative velocities of each pair of clusters, and convert to the value at a separation of 2500 kpc, assuming that the clusters move as point masses along ballistic trajectories from their current separation to a separation of 2500 kpc.

5. We also extract the total energy and impact parameter of these two clusters.

Figure 4.19 shows the initial infall velocities extracted in this way compared to the above simulation studies. Since the main cluster mass is much larger than the bullet cluster mass, we expect the initial infall velocities to be proportional to $\sqrt{M_{\text{Main}}}$, and this is just what is seen in Figure 4.19. The fit to the expected $\propto \sqrt{M_{\text{Main}}}$ behavior improves at lower masses because there are many more clusters and hence less stochastic variability. While there are 3309 cluster pairs whose main cluster mass is $5 \times 10^{14} M_{\odot} \pm 10\%$ there are only 7 cluster pairs at $2 \times 10^{15} M_{\odot} \pm 10\%$. The parameters obtained in the simulation studies discussed above are also plotted in Figure 4.19. We see that while the initial infall velocity from Mastropietro and Burkert is approximately 5 standard deviations away from the mean, the best fit initial infall velocity from this work is between 1 and 2 standard deviations above the mean. The difference is driven by our results having both a smaller initial infall velocity and a significantly larger main cluster mass than obtained by Mastropietro and Burkert.

In Figure 4.20, we plot the total energy and impact parameter of pairs of clusters extracted as described above, with main cluster mass of $2 \times 10^{15} M_{\odot} \pm 30\%$, as compared to our best fit simulation. It is seen that most cluster pairs in the Horizon simulation are near zero total energy, and our best fit simulation falls comfortably within the distribution.

4.4.2 Cluster Concentrations and Shapes

The concern that the Bullet Cluster is inconsistent with Λ CDM cosmology has focused on the initial infall velocity of the colliding clusters, and we have shown in the preceding section that this velocity is in fact not exceptional. However, it is

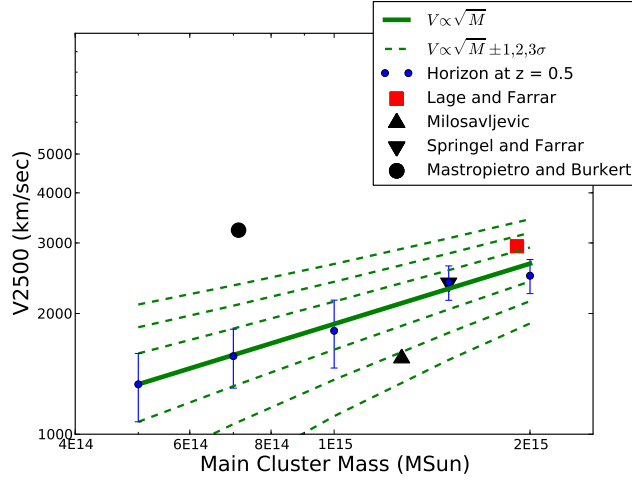


Figure 4.19: Initial infall velocity of the bullet cluster relative to the main cluster extracted from the $z=0.5$ snapshot of the Horizon simulation at a separation of 2500 kpc, using the analysis technique described in the text. The small circles are the mean relative velocity, with 1σ error bars. The thick solid line shows the expected $V \propto \sqrt{M_{\text{main}}}$ behavior. The three dotted lines are the $V \propto \sqrt{M_{\text{main}}}$ curve offset by 1, 2, and 3σ , respectively.

also worthwhile to examine the consistency of the sizes and shapes of the colliding clusters with observations and N-body simulations based on Λ CDM.

First, we examine the concentrations of the colliding clusters. Figure 4.21 shows the best fit masses and concentrations from our simulation as compared to two observational studies. Figure 4.21(A) shows the comparison to the work of Comerford [28]. While the bullet cluster is quite typical, the main cluster appears to have an unusually low concentration for its mass. However, a more recent study of Okabe [30], shown in Figure 4.21(B), has found a steeper slope for the Mass-Concentration relationship (heavy dashed line in Figure 4.21(B)) which is more consistent with our findings for the main cluster.

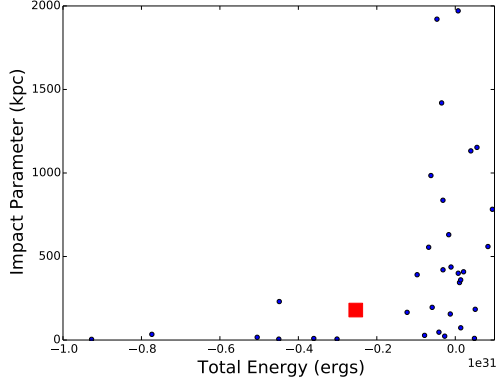
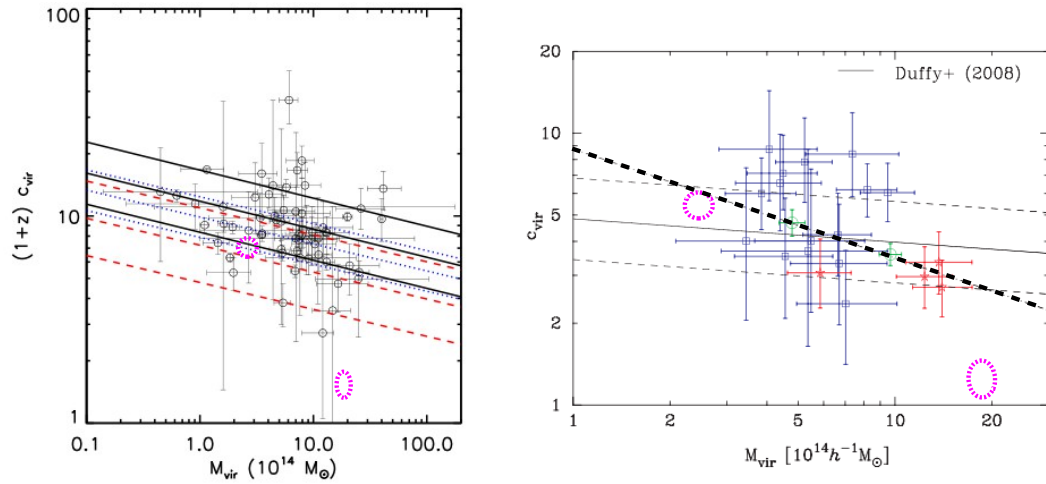


Figure 4.20: Total Energy vs Impact Parameter of cluster pairs in the Horizon Run having main cluster mass of $2 \times 10^{15} M_{\odot} \pm 30\%$. The large square represents the best fit simulation from Lage and Farrar [14].



A Comerford et.al. - 2008

B Okabe et.al. - 2011

Figure 4.21: Comparison of masses and concentrations from our best fit simulation to measured mass-concentration relations. The dotted ellipses represent one-sigma errors around the best fit simulation. In both plots, the bullet cluster is on the left and the main cluster on the right.

Using the axis ratios defined in Section 2.2.5, we compare our best fit axis ratios to those of clusters extracted from N-body simulations. This is shown in Figure 4.22. Figure 4.22(A) shows our best fit axis ratios as compared to an N-body simulation study by Bailin [55]. The bullet cluster is well within the population of clusters, while the small axis ratio of 0.35 found for the main cluster appears somewhat unusual. The more detailed study of Schneider, Frenk, and Cole [54], shown in Figure 4.22(B), examines the trends of axis ratios as a function of cluster mass and finds that more massive clusters tend to have smaller axis ratios, although the large mass of the main cluster (nearly $2 \times 10^{15} M_{\odot}$) is actually beyond the range considered. The lower right panel of Figure 4.22(B) shows our best fit axis ratio for the main cluster as compared to the largest masses studied, giving confidence that our axis ratios are within the expected distributions.

4.4.3 Comparison to Universal Baryon Fraction

Another key point of comparison is the baryon fraction value, i.e. the fraction of the total cluster mass made up of baryons. There is currently a great deal of interest in this parameter, and it is not clear whether or not to expect the gas fraction value in a galaxy cluster to match the universe-average values (Battaglia 2013 [98]; David 2012 [99]). In our work, the baryon fraction values (within R_{200}) of the initial clusters (parameters GF1 and GF2 in Table 3.3 - best fit values of $19 \pm 2\%$ and $17 \pm 2\%$) differ the Λ CDM average value at the 1-2 sigma level. The nine-year WMAP results (2013 [100]), for example, give a ratio of Ω_b/Ω_m of $16.5 \pm 2.5\%$, while the recent Planck results (2013 [101]) give a ratio of Ω_b/Ω_m of $15.4 \pm 0.5\%$. Further work is needed to determine whether the slightly higher baryon fraction values we find are due to a deficiency of our modeling, such as missing sub-

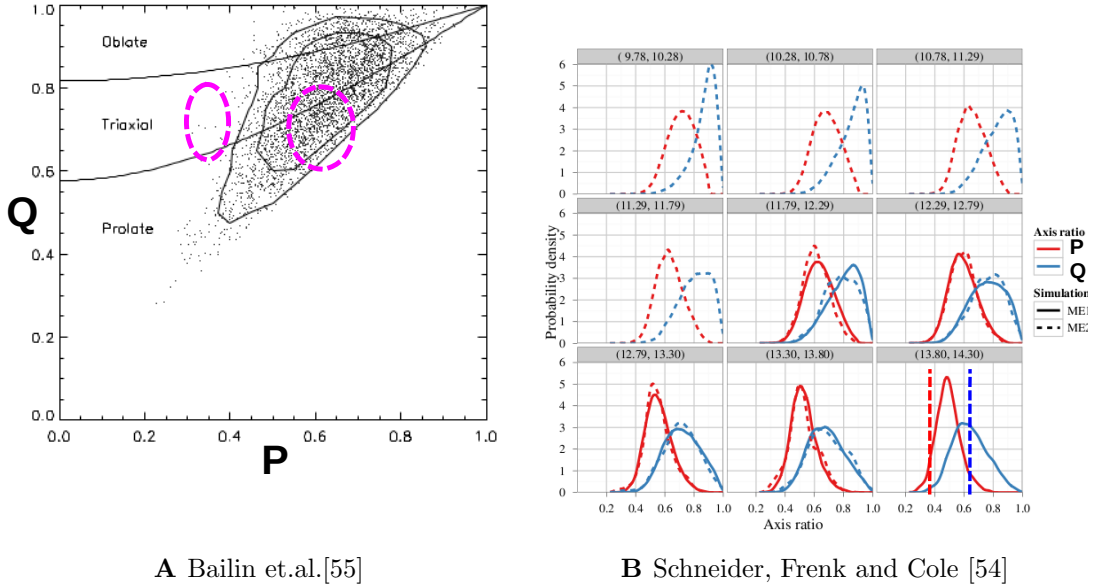


Figure 4.22: Comparison of our best fit axis ratios to those extracted from N-body simulations.

Left-hand panel: Axis ratios of halos extracted from N-body simulations by Bailin et.al.[55]. The dotted ellipses represent one-sigma errors around our best fit axis ratios, with the main cluster on the left and the bullet cluster on the right.

Right-hand panel: Axis ratios of halos of different masses extracted from N-body simulations by Schneider, Frenk, Cole [54], showing that more massive clusters have smaller axis ratios. The numbers in parentheses are the mass ranges in $\log(M_\odot)$, with masses increasing from upper left to lower right. The dotted lines in the lower right panel are our best fit axis ratios for the main cluster.

grid physics, or whether the baryon fraction in these clusters is actually enhanced over the universe-average values. The prime driver in the overall gas fraction normalizations is the X-ray luminosity, which $\sim n^2$, so including expected small-scale inhomogeneities would plausibly result in lower baryon fractions, as well as decrease the extracted metallicity which is presently somewhat high. In the next phase of the work, a variety of refinements will be explored.

4.5 Improved Modeling of Non-Thermal Pressure

As we have shown in Section 4.1.3, modeling of the non-thermal pressure is an absolute necessity in order to accurately model the S-Z signal and the plasma temperature of the Bullet Cluster. To study this further, we have compared the simulated vs measured temperatures of single galaxy clusters. As discussed in Section 3.3.1.3, we build the initial clusters so that the gas temperature is determined by the condition of hydrostatic equilibrium. Figure 4.23 shows the simulated equilibrium cluster temperature as compared to the simple Mass-Temperature relation from Vikhlinin (2006 [29]):

$$T = 5 \text{keV} \left(\frac{M_{500}}{3 \times 10^{14} M_\odot} \right)^{\frac{2}{3}} \quad (4.1)$$

Without the inclusion of non-thermal pressure, the equilibrium temperature is significantly hotter than the observations. We have addressed this up until now with our “fudge-factor” f_{ntp} .

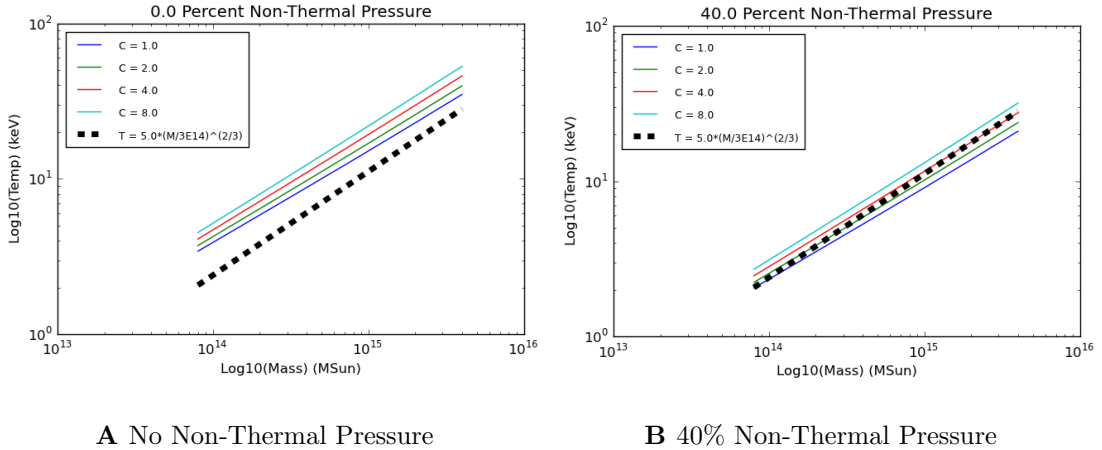


Figure 4.23: Simulated equilibrium cluster temperature as compared to Mass-Temperature relation from Vikhlinin (2006 [29]). Figure A has no non-thermal pressure and Figure B has 40% non-thermal pressure. Without the inclusion of non-thermal pressure, the equilibrium temperature is significantly hotter than the observations.

We have made significant progress toward improving this simple model, which this section will now describe. In order to create a more physical model of the non-thermal pressure, it is necessary to have a physical understanding of the mechanism. Some of the mechanisms which have been suggested include: (1) large-scale rotational fluid motions (Lau 2011 [102]), (2) turbulent fluid motions (Shi and Komatsu 2014 [46]; Nelson, Lau, and Nagai 2014 [47]), and (3) cosmic rays (Birnboim 2013 [40]). Our first direction of effort to improve our model pursues the idea that the non-thermal pressure is primarily due to turbulent fluid motions and that there are sources of energy which maintain the turbulent fluid motions by “stirring” the plasma at large scales. The most likely sources of this energy are outflows from active galaxy nuclei (Battaglia 2010 [36]). However, our model is not dependent on knowing the exact sources of this energy. Based on these assumptions, we

have simulated single galaxy clusters and shown that the turbulent fluid motions successfully play the role of non-thermal pressure. We have also quantified the numerical resolution required for these simulations to be successful.

Before reviewing these simulation results, we begin with a qualitative exploration of the energy balance of the plasma in a large galaxy cluster ($M \approx 2E15M_{\odot}$), shown in Figure 4.24. In the upper figure, there is no non-thermal pressure, so the primary energy reservoir is thermal motion (heat). In the lower figure, energy is stored in both thermal motion and turbulent fluid motion. In order to successfully model the non-thermal pressure as fluid turbulence, and in order for the non-thermal pressure to be of the same order as the thermal pressure, the energy stored in turbulent fluid motion needs to be roughly equal to the thermal energy. This is shown in the lower figure of Figure 4.24, where the energy densities given are rough estimates for a cluster of mass $M \approx 2E15M_{\odot}$. Furthermore, in order for the cluster to be roughly stable on Gy timescales, it is necessary for there to be a rough energy balance. This means that the rate of energy input into the cluster at large scales (P_{Stir}) is roughly equal to the rate at which viscous dissipation is transferring energy from turbulent fluid motion to thermal energy (P_{Visc}), which is roughly equal to the rate at which energy is being radiated away (P_{XRay}). Otherwise the energy reservoirs cannot remain roughly equal in magnitude. For example, if $P_{\text{Visc}} >> P_{\text{XRay}}$, the energy stored in fluid motion will be rapidly transferred to thermal motion, and our model no longer successfully models the non-thermal pressure.

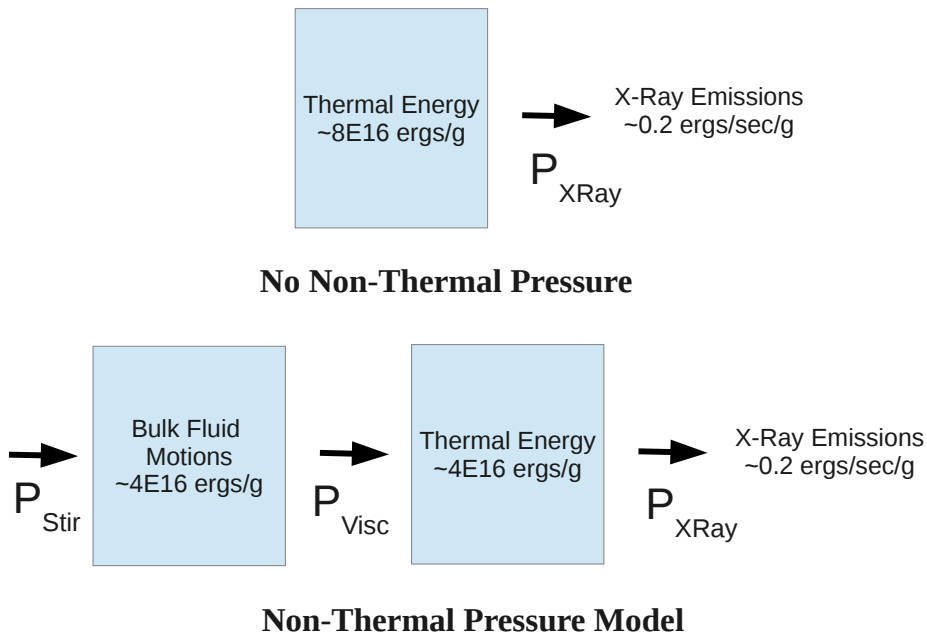


Figure 4.24: Energy balance of plasma in a large galaxy cluster. In the upper figure, there is no non-thermal pressure, so the primary energy reservoir is in thermal motion. In the lower figure, energy is stored in both thermal motion and turbulent fluid motion. The values of energy and power are rough estimates for a cluster of mass $M \approx 2\text{E}15 M_{\odot}$.

These considerations allow us to estimate the level of numerical viscosity required for our model to be successful. Numerical viscosity transfers energy from fluid motions to heat, and if the resolution is not high enough, the numerical viscosity will be too high. To quantify this, we have performed simulations of single triaxial galaxy clusters with $M \approx 2\text{E}15 M_{\odot}$, including fluid turbulence. For this study, we have not introduced a “stirring” of the fluid turbulence, but have simply seeded the gas with an initial turbulence and tracked the decay of turbulent fluid energy. We have followed Shi and Komatsu (2014 [46]) and Battaglia (2012 [37])

with an initial assumption of NTP fraction which is 10% in the cluster center and increases to 50% at R_{200} (see Figure 4.25).

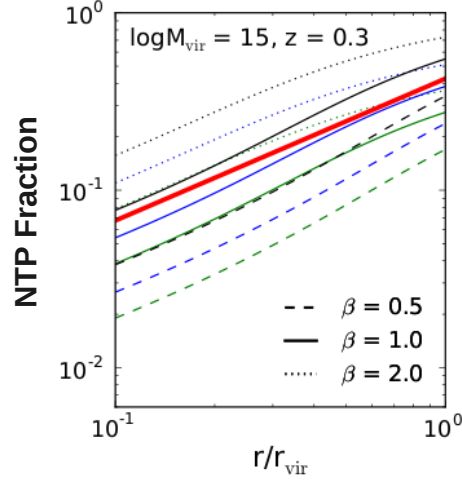


Figure 4.25: Red Line - (Battaglia 2012 [37]) fitting formula. Other lines - (Shi, Komatsu 2014 [46]) model with varying parameters. Reproduced from Shi and Komatsu.

Since the initial turbulent fluid energy is decaying exponentially, we can write:

$$E_{\text{FluidMotions}} \propto \exp(-\lambda t), \quad (4.2)$$

and the power dissipated through viscosity is:

$$P_{\text{Viscosity}} = \lambda \times E_{\text{FluidMotions}} \approx P_{\text{XRay}}, \quad (4.3)$$

meaning that we need the decay rate to be approximately:

$$\lambda \approx \frac{P_{\text{XRay}}}{E_{\text{FluidMotions}}} \approx \frac{0.2 \frac{\text{ergs}}{\text{sec-g}}}{4E16 \frac{\text{ergs}}{\text{g}}} \approx 0.2 \text{Gy}^{-1} \quad (4.4)$$

As shown in Figure 4.26, very high resolution simulations are needed in order

to reduce the numerical viscosity in the simulation to the necessary values, and we have not yet been able to achieve the resolution needed (on the order of 1 kpc grid size). However, Figure 4.27 shows the result of a cluster simulation with grid size of 2 kpc in the cluster center and 4 kpc in the outer regions. We see that when we approach the needed resolution, the fluid turbulence plays the role of non-thermal pressure as expected and stabilizes the cluster gas. Figure 4.27A shows the stable cluster that results with no turbulent fluid energy, and with the temperature set to the needed value to place the cluster in hydrostatic equilibrium. However, as we said in Figure 4.23 this temperature is too high to agree with empirically measured clusters. Figure 4.27B shows the result of simply reducing the cluster temperature, again with no turbulent fluid energy; the cluster gas rapidly collapses and heats up to the (too hot) equilibrium temperature. Figure 4.27C shows the result with the cluster gas at the lower temperature, but with significant added turbulent fluid energy; the stability of the cluster at lower temperature is much improved. To visualize the resulting fluid turbulence, Figure 4.28 shows both the x-velocity and the squared magnitude of the vorticity after the simulation of Figure 4.27C has run for 0.4 Gy. The lower magnitude of the turbulence in the cluster center is clearly visible.

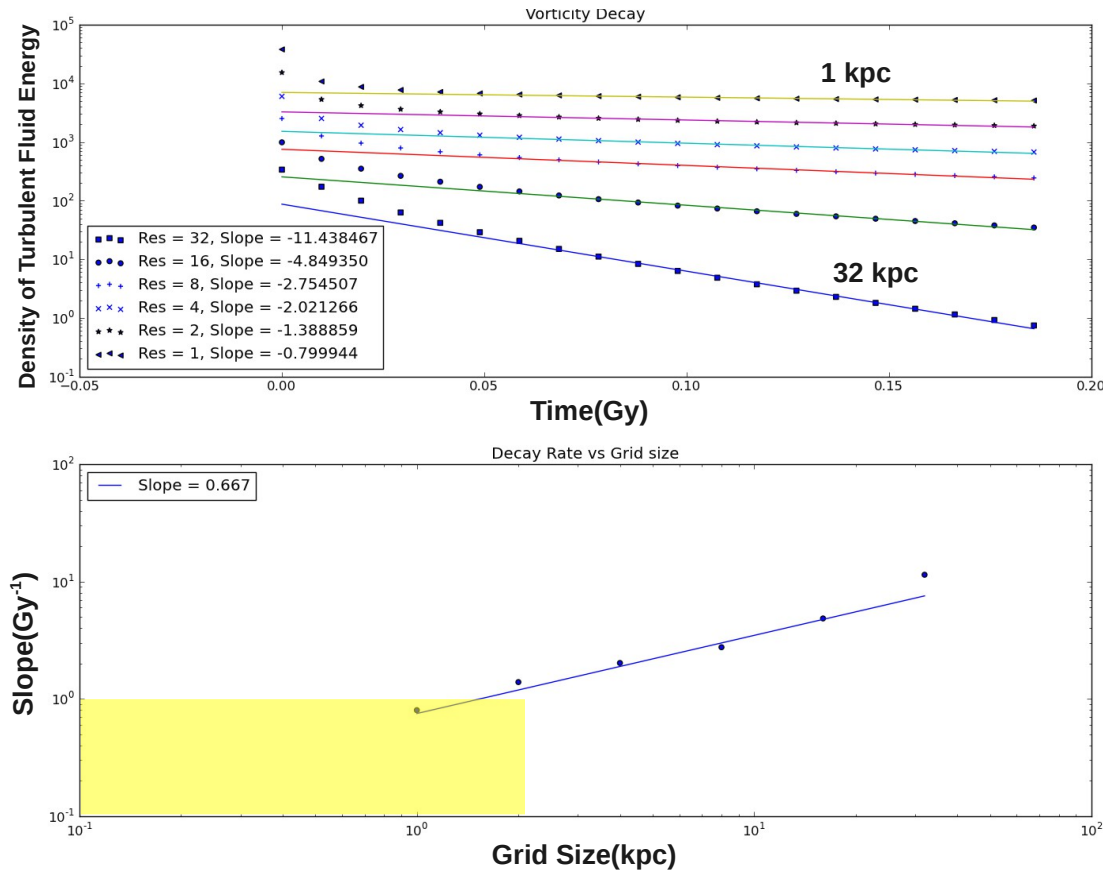


Figure 4.26: Decay of turbulent fluid energy as a function of grid resolution. Grid sizes on the order of 1 kpc or less are needed in order to reduce the numerical viscosity to the required level.

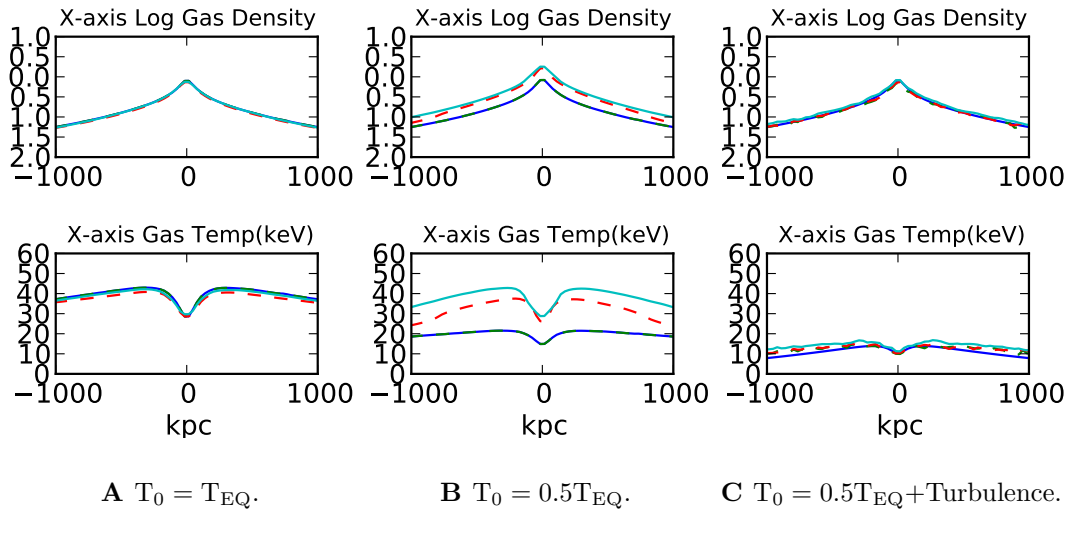
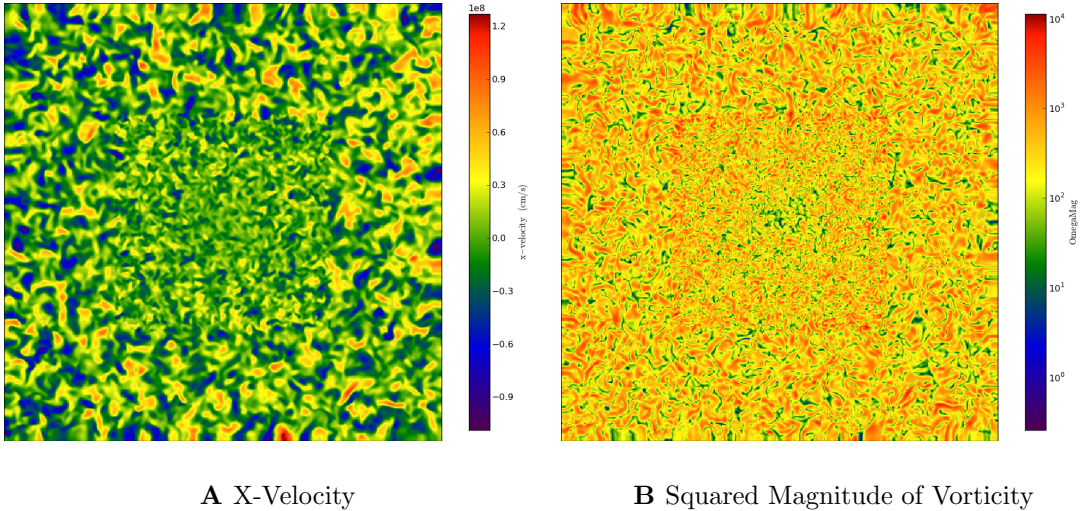


Figure 4.27: Simulated evolution of cluster gas. (Solid Blue: $t=0.0$ Gy; Dashed Green: $t=0.01$ Gy; Dashed Red: $t=0.40$ Gy; Solid Aqua: $t=0.80$ Gy)

Left: Without fluid turbulence, the equilibrium temperature of the cluster gas is too high.

Center: Reducing the gas temperature results in an unstable cluster.

Right: The inclusion of fluid turbulence allows a stable cluster at realistic temperature.



A X-Velocity

B Squared Magnitude of Vorticity

Figure 4.28: Non-thermal pressure modeled as fluid turbulence. NTP fraction is 10% in cluster center, increasing to 50% at R_{200} . 2×512^3 grid - grid size of 2 kpc in center 1 Mpc, 4 kpc in outer regions. (Plot is a 2Mpc X 2Mpc region.)

While much more needs to be done, this promising initial result points the way to future work to model the non-thermal pressure in a more physically realistic way. Performing a large number of simulations in this way is probably not realistic in terms of computing resources, so another approach is needed. Fortunately, a number of researchers are working on enhancing hydrodynamical models through the incorporation of sub-grid scale turbulence (Maier 2009 [103]; Latif 2013 [104]; Schmidt 2011 [105]; Iapichino 2011 [106]). This method carries the energy content of the turbulence which is present on sub-grid scales as additional fluid variables, allowing a more computationally efficient modeling of the contribution of the fluid turbulence to the non-thermal pressure. In Section 5.2, we discuss how this future work might proceed.

Chapter 5

Conclusions and Recommendations

5.1 Conclusions

We have presented a detailed simulation of the Bullet Cluster collision, which gives a 2D fit to observational data spanning an impressively wide range of wavelengths. The major conclusions of this work are as follows:

1. A simple initial configuration of two triaxial clusters fits the observed data for mass lensing quite well. The cluster masses, concentrations, and triaxialities required are compatible with those seen in N-body simulations.
2. The infall velocities required to explain the observations are not excessive compared to Λ CDM simulations.
3. The observed X-ray flux is quite sensitive to the baryon structure and can be reproduced with reasonable assumptions for the initial baryon distributions,

although the fits are not as good as the fits to the mass lensing data only. The best-fit structure of the initial clusters is similar to other observed clusters. The best-fit baryon fraction within the clusters is close to the average in the Universe, but slightly higher; whether this is an artifact of our simplified description is under investigation.

4. A significant amount of non-thermal pressure, roughly equal to the thermal pressure, is required in order to fit plasma temperature and S-Z effect observations.
5. Addition of magnetic fields to the simulations improves the simultaneous fit of the mass lensing and X-ray flux data, and the magnetic fields required are in rough agreement with what is required to explain the radio halo observations.
6. Initial work has demonstrated the feasibility of modeling the required non-thermal pressure as fluid turbulence, although very high resolutions are needed in order to reduce the numerical viscosity to physical levels.

5.2 Recommendations for Future Work

As always in a work of this type, one learns along the way. We can see many ways in which the work can be improved, and ways in which the work can be extended to other areas. Some of these are:

1. *Improvement of Non-Thermal Pressure modeling* The modeling of non-thermal pressure is clearly the weakest part of this analysis. We have shown in Section 4.5 the feasibility of modeling the non-thermal pressure as fluid turbulence.

Very high resolution simulations are needed in order to reduce the numerical viscosity in the simulation to realistic physical values, but when this is done the fluid turbulence serves as the expected source of non-thermal pressure. We propose to use sub-grid scale modeling to model the turbulent fluid motions in a computationally efficient way. We have obtained a preliminary copy of the Enzo code with the sub-grid-scale terms added (Wolfram Schmidt, private communication, April, 2014). A logical path is to study and modify this code as necessary to allow us to model single galaxy clusters, using high-resolution simulations of single galaxy clusters (like Figure 4.27) to calibrate the sub-grid-scale code. We can then build simulations of stable single galaxy clusters to use as inputs to the cluster collisions. This will give a much more realistic model of the non-thermal pressure than we have done to date. There are also observational studies ongoing (Vazza 2011 [107]; Bohringer 2010 [108]; Biffi 2013 [109]; Zhuravleva 2014 [110]) which attempt to quantify the fluid turbulence, mainly through measuring thermal broadening of X-ray spectral lines.

2. *Verification of Magnetic Field Configuration* While our results with inclusion of the magnetic field encourage us that it may be possible to constrain the cluster magnetic field, much work is needed before this can be done. In particular, the coherence length of the initial magnetic field has an effect on the structure and growth of the magnetic fields during the collision, and this needs to be explored. Furthermore, the required level of magnetic fields is likely related to the amount of non-thermal pressure, so the reliability of the inferred magnetic fields can only be settled after the more physical model of the non-thermal pressure has implemented.

3. *Use of colliding galaxy clusters to constrain dark matter interactions and alternatives to GR:* Having achieved believable models for a galaxy cluster merger, one of our goals was to use these models to introduce constraints on dark-matter interactions and alternate theories of gravity. Simulations of these cluster mergers are ideal laboratories for this. The plan would be to introduce the modified interactions, then repeat the optimization to see if a physically reasonable initial cluster structure can still explain the existing observations. Repeating this process should allow us to place constraints on the strength of the modified interactions.
4. *Build a catalog of merging galaxy clusters:* One request that we have received is to use the simulation machinery that we have created in this work to build a catalog of merging galaxy clusters to help guide the observations. The plan here would be to draw a set of initial galaxy clusters from a distribution, assign them an appropriate set of initial conditions, and then collide them and depict the result at different times and different viewing angles. This catalog could be especially useful for interpreting the large S-Z catalogs which are upcoming.
5. *Improvement of radio emission model:* The work to date has used a simple model for calculating the radio emissions from the colliding clusters. There is much opportunity to enhance this model by introducing a more physical model for the evolution of the non-thermal electron population responsible for the emissions, as well as introducing more realistic models for the magnetic fields. Some relevant references on this work include (vanWeeren 2011 [111]; Ensslin 2009 [59]; Vogt 2013 [58]).

6. *Application of the 2D image technique to other galaxy cluster collisions:* The techniques developed here of using the fit between observed 2D images and simulated 2D images to constrain the structure of colliding clusters has given insight into the Bullet Cluster collision. There are numerous other examples of colliding galaxy clusters, some more complex in that they have three or more colliding clusters. We propose to apply these techniques to a selected group of these other clusters. The cluster known as “El Gordo” (ACT-CL J0102-4915) appears to have the most observational data at present, so we would propose to begin with this cluster. Some simulation work on this has already been reported (Donnert 2014 [112]).

Finally, more and better observational data will be a valuable addition to the modeling efforts. Our results depend heavily on having an accurate reconstruction of the current mass distribution. Since the X-ray flux is proportional to the square of the baryon density, and the baryon density depends on the dark matter density, small changes in the mass distribution lead to large changes in the calculated X-ray flux. Errors in the mass reconstruction will therefore lead to errors in our determination of the optimal initial conditions. To constrain the magnetic fields, polarized radio emission and Faraday rotation measures of sources behind the bullet – especially strongly lensed ones! – would help the effort immensely.

Bibliography

- [1] M. J. Turk, B. D. Smith, J. S. Oishi, S. Skory, S. W. Skillman, T. Abel, and M. L. Norman. yt: A Multi-code Analysis Toolkit for Astrophysical Simulation Data. *"Astrophys. J. Supp."*, 192:9, January 2011.
- [2] M. Markevitch. Chandra observation of the most interesting cluster in the universe. *astro-ph/0511345*, 2005.
- [3] M. Markevitch, A. H. Gonzalez, L. David, A. Vikhlinin, S. Murray, W. Forman, C. Jones, and W. Tucker. A Textbook Example of a Bow Shock in the Merging Galaxy Cluster 1E 0657-56. *"Astrophys. J. Lett."*, 567:L27–L31, March 2002.
- [4] P. Kroupa, M. Pawłowski, and M. Milgrom. The Failures of the Standard Model of Cosmology Require a New Paradigm. *International Journal of Modern Physics D*, 21:30003, December 2012.
- [5] D. Clowe, A. Gonzalez, and M. Markevitch. Weak-Lensing Mass Reconstruction of the Interacting Cluster 1E 0657-558: Direct Evidence for the Existence of Dark Matter. *"Astrophys. J."*, 604:596–603, April 2004.

- [6] D. Clowe, M. Bradač, A. H. Gonzalez, M. Markevitch, S. W. Randall, C. Jones, and D. Zaritsky. A Direct Empirical Proof of the Existence of Dark Matter. *"Astrophys. J. Lett."*, 648:L109–L113, September 2006.
- [7] J. R. Brownstein and J. W. Moffat. The Bullet Cluster 1E0657-558 evidence shows modified gravity in the absence of dark matter. *"Monthly Notices RAS"*, 382:29–47, November 2007.
- [8] V. Springel and G. R. Farrar. The speed of the ‘bullet’ in the merging galaxy cluster 1E0657-56. *"Monthly Notices RAS"*, 380:911–925, September 2007.
- [9] C. Mastropietro and A. Burkert. Simulating the Bullet Cluster. *"Monthly Notices RAS"*, 389:967–988, September 2008.
- [10] M. Milosavljević, J. Koda, D. Nagai, E. Nakar, and P. R. Shapiro. The Cluster-Merger Shock in 1E 0657-56: Faster than a Speeding Bullet? *"Astrophys. J. Lett."*, 661:L131–L134, June 2007.
- [11] W. A. Dawson. The Dynamics of Merging Clusters: A Monte Carlo Solution Applied to the Bullet and Musket Ball Clusters. *"Astrophys. J."*, 772:131, August 2013.
- [12] J. Lee and E. Komatsu. Bullet Cluster: A Challenge to Λ CDM Cosmology. *"Astrophys. J."*, 718:60–65, July 2010.
- [13] E. Hayashi and S. White. How rare is the bullet cluster? *astro-ph/0604443*, 2006.
- [14] Craig Lage and Glennys Farrar. Constrained Simulation of the Bullet Cluster. *"Astrophys. J."*, 787(2):144, 2014.

- [15] M. Markevitch et al. Direct Constraints on the Dark Matter Self-Interaction Cross Section from the Merging Galaxy Cluster 1E 0657-56. *"Astrophys. J."*, 606:819–824, May 2004.
- [16] S. W. Randall, M. Markevitch, D. Clowe, A. H. Gonzalez, and M. Bradač. Constraints on the Self-Interaction Cross Section of Dark Matter from Numerical Simulations of the Merging Galaxy Cluster 1E 0657-56. *"Astrophys. J."*, 679:1173–1180, June 2008.
- [17] V. Mukhanov. *Physical Foundations of Cosmology*. Cambridge University Press, 2005.
- [18] J. Kim, C. Park, J. R. Gott, III, and J. Dubinski. The Horizon Run N-Body Simulation: Baryon Acoustic Oscillations and Topology of Large-scale Structure of the Universe. *"Astrophys. J."*, 701:1547–1559, August 2009.
- [19] E.-H. Peng, K. Andersson, M. W. Bautz, and G. P. Garmire. Deep Chandra observation of Abell 1689. In *AAS/High Energy Astrophysics Division #10*, volume 10 of *AAS/High Energy Astrophysics Division*, page #09.03, March 2008.
- [20] Abell 1689 Image, 2008. <http://chandra.harvard.edu/photo/2008/a1689>.
- [21] D. W. Hogg. Distance measures in cosmology. *ArXiv Astrophysics e-prints*, May 1999.
- [22] D. Coe, N. Benítez, T. Broadhurst, and L. A. Moustakas. A High-resolution Mass Map of Galaxy Cluster Substructure: LensPerfect Analysis of A1689. *"Astrophys. J."*, 723:1678–1702, November 2010.

- [23] A. Vikhlinin, M. Markevitch, S. S. Murray, C. Jones, W. Forman, and L. Van Speybroeck. Chandra Temperature Profiles for a Sample of Nearby Relaxed Galaxy Clusters. *"Astrophys. J."*, 628:655–672, August 2005.
- [24] A. H. Gonzalez, S. Sivanandam, A. I. Zabludoff, and D. Zaritsky. Galaxy Cluster Baryon Fractions Revisited. *"Astrophys. J."*, 778:14, November 2013.
- [25] F. Zwicky. On the Masses of Nebulae and of Clusters of Nebulae. *"Astrophys. J."*, 86:217, October 1937.
- [26] J. F. Navarro, C. S. Frenk, and S. D. M. White. The Structure of Cold Dark Matter Halos. *"Astrophys. J."*, 462:563, May 1996.
- [27] D. Merritt, A. W. Graham, B. Moore, J. Diemand, and B. Terzić. Empirical Models for Dark Matter Halos. I. Nonparametric Construction of Density Profiles and Comparison with Parametric Models. *"Astrophys. J."*, 132:2685–2700, December 2006.
- [28] J. M. Comerford and P. Natarajan. The observed concentration-mass relation for galaxy clusters. *"Monthly Notices RAS"*, 379:190–200, July 2007.
- [29] A. Vikhlinin, A. Kravtsov, W. Forman, C. Jones, M. Markevitch, S. S. Murray, and L. Van Speybroeck. Chandra Sample of Nearby Relaxed Galaxy Clusters: Mass, Gas Fraction, and Mass-Temperature Relation. *Astrophys. J.*, 640:691–709, April 2006.
- [30] N. Okabe, M. Takada, K. Umetsu, T. Futamase, and G. P. Smith. LoCuSS: Subaru Weak Lensing Study of 30 Galaxy Clusters. *"Pub. ASJ"*, 62:811–, June 2010.

- [31] S. Bhattacharya, S. Habib, K. Heitmann, and A. Vikhlinin. Dark Matter Halo Profiles of Massive Clusters: Theory versus Observations. *"Astrophys. J."*, 766:32, March 2013.
- [32] H. Tananbaum and M. Weisskopf. A General Description and Current Status of the Chandra X-ray Observatory (Invited). In H. Inoue and H. Kunieda, editors, *New Century of X-ray Astronomy*, volume 251 of *Astronomical Society of the Pacific Conference Series*, page 4, 2001.
- [33] A. Leccardi and S. Molendi. Radial temperature profiles for a large sample of galaxy clusters observed with XMM-Newton. *"Astro. & Astrophys."*, 486:359–373, August 2008.
- [34] M. Arnaud, G. W. Pratt, R. Piffaretti, H. Böhringer, J. H. Croston, and E. Pointecouteau. The universal galaxy cluster pressure profile from a representative sample of nearby systems (REXCESS) and the Y_{SZ} - M_{500} relation. *"Astro. & Astrophys."*, 517:A92, July 2010.
- [35] M. Arnaud. The β -model of the intracluster medium. Commentary on: Cavaliere A. and Fusco-Femiano R., 1976, AA, 49, 137. *"Astro. & Astrophys."*, 500:103–104, June 2009.
- [36] N. Battaglia, J. R. Bond, C. Pfrommer, J. L. Sievers, and D. Sijacki. Simulations of the Sunyaev-Zel'dovich Power Spectrum with Active Galactic Nucleus Feedback. *"Astrophys. J."*, 725:91–99, December 2010.
- [37] N. Battaglia, J. R. Bond, C. Pfrommer, and J. L. Sievers. On the Cluster Physics of Sunyaev-Zel'dovich and X-Ray Surveys. I. The Influence of Feed-

back, Non-thermal Pressure, and Cluster Shapes on Y-M Scaling Relations. ”*Astrophys. J.*”, 758:74, October 2012.

- [38] S. Khedekar, E. Churazov, A. Kravtsov, I. Zhuravleva, E. T. Lau, D. Nagai, and R. Sunyaev. Bias from gas inhomogeneities in the pressure profiles as measured from X-ray and Sunyaev-Zeldovich observations. ”*Monthly Notices RAS*”, 431:954–965, May 2013.
- [39] D. A. Prokhorov, E. T. Million, T. Akahori, M. Zemcov, A. Moraghan, S. Nagataki, K. Yoshikawa, S. Colafrancesco, T. D. Rawle, and E. Egami. A high-resolution study of the X-ray emission and Sunyaev-Zel’dovich effect in the Bullet cluster (1E 0657-56). ”*Monthly Notices RAS*”, 426:2291–2299, November 2012.
- [40] Y. Birnboim and S. Balberg. Galaxy Evolution: Modeling the Role of Non-thermal Pressure in the Interstellar medium. *ArXiv e-prints*, November 2013.
- [41] T. Plagge, B. A. Benson, P. A. R. Ade, K. A. Aird, L. E. Bleem, J. E. Carlstrom, C. L. Chang, H.-M. Cho, T. M. Crawford, A. T. Crites, T. de Haan, M. A. Dobbs, E. M. George, N. R. Hall, N. W. Halverson, G. P. Holder, W. L. Holzapfel, J. D. Hrubes, M. Joy, R. Keisler, L. Knox, A. T. Lee, E. M. Leitch, M. Lueker, D. Marrone, J. J. McMahon, J. Mehl, S. S. Meyer, J. J. Mohr, T. E. Montroy, S. Padin, C. Pryke, C. L. Reichardt, J. E. Ruhl, K. K. Schaffer, L. Shaw, E. Shirokoff, H. G. Spieler, B. Stalder, Z. Staniszewski, A. A. Stark, K. Vanderlinde, J. D. Vieira, R. Williamson, and O. Zahn. Sunyaev-Zel’dovich Cluster Profiles Measured with the South Pole Telescope. ”*Astrophys. J.*”, 716:1118–1135, June 2010.

- [42] A. Loeb and S. Mao. Evidence from gravitational lensing for a nonthermal pressure support in the cluster of galaxies Abell 2218. *"Astrophys. J. Lett."*, 435:L109–L112, November 1994.
- [43] P. Bode, J. P. Ostriker, and A. Vikhlinin. Exploring the Energetics of Intra-cluster Gas with a Simple and Accurate Model. *"Astrophys. J."*, 700:989–999, August 2009.
- [44] M. Brüggen, M. Ruszkowski, and E. Hallman. Active Galactic Nuclei Heating and Dissipative Processes in Galaxy Clusters. *"Astrophys. J."*, 630:740–749, September 2005.
- [45] A. Lazarian and G. Brunetti. Turbulence, reconnection and cosmic rays in galaxy clusters . *"Memorie della Societa Astronomica Italiana"*, 82:636, 2011.
- [46] X. Shi and E. Komatsu. Analytical model for non-thermal pressure in galaxy clusters. *ArXiv e-prints*, January 2014.
- [47] K. Nelson, E. T. Lau, and D. Nagai. Universal Non-thermal Pressure Fraction Profile in Galaxy Clusters. *ArXiv e-prints*, April 2014.
- [48] M. Markevitch and A. Vikhlinin. Shocks and cold fronts in galaxy clusters. *"Physics Reports"*, 443:1–53, May 2007.
- [49] M. S. Owers, P. E. J. Nulsen, W. J. Couch, and M. Markevitch. A High Fidelity Sample of Cold Front Clusters from the Chandra Archive. *"Astrophys. J."*, 704:1349–1370, October 2009.

- [50] E. L. Blanton, C. L. Sarazin, and B. R. McNamara. Chandra Observation of the Radio Source / ICM Interaction in the Cooling Flow Cluster Abell 262. In *American Astronomical Society Meeting Abstracts*, volume 201 of *Bulletin of the American Astronomical Society*, page 302, December 2002.
- [51] J. C. Vernaleo and C. S. Reynolds. AGN Feedback and Cooling Flows: Problems with Simple Hydrodynamic Models. *"Astrophys. J."*, 645:83–94, July 2006.
- [52] I. J. Parrish, E. Quataert, and P. Sharma. Anisotropic Thermal Conduction and the Cooling Flow Problem in Galaxy Clusters. *"Astrophys. J."*, 703:96–108, September 2009.
- [53] M. Limousin, A. Morandi, M. Sereno, M. Meneghetti, S. Ettori, M. Bartelmann, and T. Verdugo. The Three-Dimensional Shapes of Galaxy Clusters. *"Space Science Reviews"*, 177:155–194, August 2013.
- [54] M. D. Schneider, C. S. Frenk, and S. Cole. The shapes and alignments of dark matter halos. *"Journal of Cosmology and Astroparticle Physics"*, 5:30, May 2012.
- [55] J. Bailin and M. Steinmetz. Internal and External Alignment of the Shapes and Angular Momenta of Λ CDM Halos. *"Astrophys. J."*, 627:647–665, July 2005.
- [56] E. T. Lau, D. Nagai, A. V. Kravtsov, A. Vikhlinin, and A. R. Zentner. Constraining Cluster Physics with the Shape of X-Ray Clusters: Comparison of Local X-Ray Clusters Versus Λ CDM Clusters. *"Astrophys. J."*, 755:116, August 2012.

- [57] C. L. Carilli and G. B. Taylor. Cluster Magnetic Fields. *"Annu. Rev. Astron. Astrophys."*, 40:319–348, 2002.
- [58] C. Vogt and T. A. Enßlin. Measuring the cluster magnetic field power spectra from Faraday rotation maps of Abell 400, Abell 2634 and Hydra A. *"Astro. & Astrophys."*, 412:373–385, December 2003.
- [59] T. A. Enßlin, T. Clarke, C. Vogt, A. Waelkens, and A. A. Schekochihin. Magnetic turbulence in clusters of galaxies. In *Revista Mexicana de Astronomia y Astrofisica Conference Series*, volume 36 of *Revista Mexicana de Astronomia y Astrofisica, vol. 27*, pages 209–215, August 2009.
- [60] H. Xu, F. Govoni, M. Murgia, H. Li, D. C. Collins, M. L. Norman, R. Cen, L. Feretti, and G. Giovannini. Comparisons of Cosmological Magnetohydrodynamic Galaxy Cluster Simulations to Radio Observations. *"Astrophys. J."*, 759:40, November 2012.
- [61] K. Dolag, M. Bartelmann, and H. Lesch. SPH simulations of magnetic fields in galaxy clusters. *"Astro. & Astrophys."*, 348:351–363, August 1999.
- [62] K. Dolag, S. Schindler, F. Govoni, and L. Feretti. Correlation of the magnetic field and the intra-cluster gas density in galaxy clusters. *"Astro. & Astrophys."*, 378:777–786, November 2001.
- [63] K. Dolag, M. Bartelmann, and H. Lesch. Evolution and structure of magnetic fields in simulated galaxy clusters. *"Astro. & Astrophys."*, 387:383–395, May 2002.
- [64] H. Kotarba, H. Lesch, K. Dolag, T. Naab, P. H. Johansson, J. Donnert,

and F. A. Stasyszyn. Galactic ménage à trois: simulating magnetic fields in colliding galaxies. *"Monthly Notices RAS"*, 415:3189–3218, August 2011.

- [65] A. V. Kravtsov and S. Borgani. Formation of Galaxy Clusters. *"Annu. Rev. Astron. Astrophys."*, 50:353–409, September 2012.
- [66] D. Clowe. The bullet cluster 1e0657: Official project page, 2006.
<http://flamingos.astro.ufl.edu/1e0657/index.html>.
- [67] M. Bradač, D. Clowe, A. H. Gonzalez, P. Marshall, W. Forman, C. Jones, M. Markevitch, S. Randall, T. Schrabback, and D. Zaritsky. Strong and Weak Lensing United. III. Measuring the Mass Distribution of the Merging Galaxy Cluster 1ES 0657-558. *"Astrophys. J."*, 652:937–947, December 2006.
- [68] D. Paraficz, J.-P. Kneib, J. Richard, A. Morandi, M. Limousin, and E. Jullo. The Bullet Cluster revisited: New results from new constraints and improved strong lensing modeling technique. *ArXiv e-prints*, September 2012.
- [69] A. Fruscione, J. C. McDowell, G. E. Allen, N. S. Brickhouse, D. J. Burke, J. E. Davis, N. Durham, M. Elvis, E. C. Galle, D. E. Harris, D. P. Huenemoerder, J. C. Houck, B. Ishibashi, M. Karovska, F. Nicastro, M. S. Noble, M. A. Nowak, F. A. Primini, A. Siemiginowska, R. K. Smith, and M. Wise. CIAO: Chandra’s data analysis system. In *Society of Photo-Optical Instrumentation Engineers (SPIE) Conference Series*, volume 6270 of *Society of Photo-Optical Instrumentation Engineers (SPIE) Conference Series*, July 2006.
- [70] N. W. Halverson, T. Lanting, P. A. R. Ade, K. Basu, A. N. Bender, B. A. Benson, F. Bertoldi, H.-M. Cho, G. Chon, J. Clarke, M. Dobbs, D. Ferrusca, R. Güsten, W. L. Holzapfel, A. Kovács, J. Kennedy, Z. Kermish,

- R. Kneissl, A. T. Lee, M. Lueker, J. Mehl, K. M. Menten, D. Muders, M. Nord, F. Pacaud, T. Plagge, C. Reichardt, P. L. Richards, R. Schaaf, P. Schilke, F. Schuller, D. Schwan, H. Spieler, C. Tucker, A. Weiss, and O. Zahn. Sunyaev-Zel'Dovich Effect Observations of the Bullet Cluster (1E 0657-56) with APEX-SZ. *"Astrophys. J."*, 701:42–51, August 2009.
- [71] H. Liang, R. W. Hunstead, M. Birkinshaw, and P. Andreani. A Powerful Radio Halo in the Hottest Known Cluster of Galaxies 1E 0657-56. *"Astrophys. J."*, 544:686–701, December 2000.
- [72] T. W. Shimwell, S. Brown, I. J. Feain, L. Feretti, B. M. Gaensler, and C. Lage. Deep radio observations of the radio halo of the bullet cluster 1E 0657-55.8. *"Monthly Notices RAS"*, 440:2901–2915, June 2014.
- [73] E. Vasiliev and E. Athanassoula. Chaotic mixing and the secular evolution of triaxial cuspy galaxy models built with Schwarzschild's method. *"Monthly Notices RAS"*, 419:3268–3279, February 2012.
- [74] F. S. Kitaura and T. A. Enßlin. Bayesian reconstruction of the cosmological large-scale structure: methodology, inverse algorithms and numerical optimization. *"Monthly Notices RAS"*, 389:497–544, September 2008.
- [75] V. Springel. The cosmological simulation code GADGET-2. *"Monthly Notices RAS"*, 364:1105–1134, December 2005.
- [76] The Enzo Collaboration, G. L. Bryan, M. L. Norman, B. W. O'Shea, T. Abel, J. H. Wise, M. J. Turk, D. R. Reynolds, D. C. Collins, P. Wang, S. W. Skillman, B. Smith, R. P. Harkness, J. Bordner, J.-h. Kim, M. Kuhlen, H. Xu, N. Goldbaum, C. Hummels, A. G. Krutsuk, E. Tasker, S. Skory, C. M.

Simpson, O. Hahn, J. S. Oishi, G. C So, F. Zhao, R. Cen, and Y. Li. Enzo: An Adaptive Mesh Refinement Code for Astrophysics. *ArXiv 1307.2265*, July 2013.

- [77] R. K. Smith, N. S. Brickhouse, D. A. Liedahl, and J. C. Raymond. Collisional Plasma Models with APEC/APED: Emission-Line Diagnostics of Hydrogen-like and Helium-like Ions. *"Astrophys. J. Lett."*, 556:L91–L95, August 2001.
- [78] Joung hun Lee and Yasushi Suto. Modeling intracluster gas in triaxial dark halos: An analytic approach. *The Astrophysical Journal*, 585(1):151, 2003.
- [79] James Binney and Scott Tremaine. *Galactic Dynamics*. Princeton University Press, second edition, 2008.
- [80] M. Schwarzschild. A numerical model for a triaxial stellar system in dynamical equilibrium. *"Astrophys. J."*, 232:236–247, August 1979.
- [81] D. Yurin and V. Springel. An iterative method for the construction of N-body galaxy models in collisionless equilibrium. *ArXiv e-prints*, February 2014.
- [82] P. Bode, J. P. Ostriker, R. Cen, and H. Trac. Calibration of Nonthermal Pressure in Global Dark Matter Simulations of Clusters of Galaxies. *arXiv pre-print astro-ph*, April 2012. <http://arxiv.org/pdf/1204.1762.pdf>.
- [83] G. B. Rybicki and A. P. Lightman. *Radiative Processes in Astrophysics*. John Wiley and Sons, June 1986.
- [84] N. Itoh, T. Sakamoto, S. Kusano, Y. Kawana, and S. Nozawa. Radiative

processes in the intracluster plasma. *"Astro. & Astrophys."*, 382:722–729, February 2002.

- [85] F. Govoni, M. Markevitch, A. Vikhlinin, L. van Speybroeck, L. Feretti, and G. Giovannini. Chandra Temperature Maps for Galaxy Clusters with Radio Halos. *"Astrophys. J."*, 605:695–708, April 2004.
- [86] D. Nagai, A. Vikhlinin, and A. V. Kravtsov. Testing X-Ray Measurements of Galaxy Clusters with Cosmological Simulations. *"Astrophys. J."*, 655:98–108, January 2007.
- [87] P. Mazzotta, E. Rasia, S. Borgani, L. Moscardini, K. Dolag, and G. Tormen. Spectroscopic-Like Temperature of Clusters of Galaxies and Cosmological Implications. *ArXiv Astrophysics e-prints*, December 2004.
- [88] M. Birkinshaw. The Sunyaev-Zel'dovich effect. *"Physics Reports"*, 310:97–195, March 1999.
- [89] F. Govoni and L. Feretti. Magnetic Fields in Clusters of Galaxies. *International Journal of Modern Physics D*, 13:1549–1594, 2004.
- [90] H. Liang, V. A. Dogiel, and M. Birkinshaw. The origin of radio haloes and non-thermal emission in clusters of galaxies. *"Monthly Notices RAS"*, 337:567–577, December 2002.
- [91] R. J. van Weeren, M. Brüggen, H. J. A. Röttgering, and M. Hoeft. Relics as Probes of Galaxy Cluster Mergers. *Journal of Astrophysics and Astronomy*, 32:505–508, December 2011.

- [92] Nikolay Bliznyuk, David Ruppert, Christine A. Shoemaker, Rommel G. Regis, Stefan M. Wild, and Pradeep Mugunthan. Bayesian calibration of computationally expensive models using optimization and radial basis function approximation. *Journal of Computational and Graphical Statistics*, 17(2):1–25, 2008.
- [93] R. Barrena et al. The dynamical status of the cluster of galaxies 1E0657-56. ”*Astro. & Astrophys.*”, 386:816–828, May 2002.
- [94] M. McCourt, E. Quataert, and I. J. Parrish. What Sets Temperature Gradients in Galaxy Clusters? Implications for non-thermal pressure support and mass-observable scaling relations. *ArXiv e-prints*, December 2012.
- [95] A. Simionescu, S. W. Allen, A. Mantz, N. Werner, Y. Takei, R. G. Morris, A. C. Fabian, J. S. Sanders, P. E. J. Nulsen, M. R. George, and G. B. Taylor. Baryons at the Edge of the X-ray-Brightest Galaxy Cluster. *Science*, 331:1576–, March 2011.
- [96] M. Markevitch, T. J. Ponman, P. E. J. Nulsen, M. W. Bautz, D. J. Burke, L. P. David, D. Davis, R. H. Donnelly, W. R. Forman, C. Jones, J. Kaastra, E. Kellogg, D.-W. Kim, J. Kolodziejczak, P. Mazzotta, A. Pagliaro, S. Patel, L. Van Speybroeck, A. Vikhlinin, J. Vrtilek, M. Wise, and P. Zhao. Chandra Observation of Abell 2142: Survival of Dense Subcluster Cores in a Merger. ”*Astrophys. J.*”, 541:542–549, October 2000.
- [97] C. Lage and G. R. Farrar. The Bullet Cluster is not a Cosmological Anomaly. *ArXiv 1406.6703*, June 2014.
- [98] N. Battaglia, J. R. Bond, C. Pfrommer, and J. L. Sievers. On the Cluster

Physics of Sunyaev-Zel'dovich and X-Ray Surveys. III. Measurement Biases and Cosmological Evolution of Gas and Stellar Mass Fractions. *"Astrophys. J."*, 777:123, November 2013.

- [99] L. P. David, C. Jones, and W. Forman. The Universal Gas Mass Fraction in Clusters of Galaxies. *"Astrophys. J."*, 748:120, April 2012.
- [100] G. Hinshaw, D. Larson, E. Komatsu, D. N. Spergel, C. L. Bennett, J. Dunkley, M. R. Nolta, M. Halpern, R. S. Hill, N. Odegard, L. Page, K. M. Smith, J. L. Weiland, B. Gold, N. Jarosik, A. Kogut, M. Limon, S. S. Meyer, G. S. Tucker, E. Wollack, and E. L. Wright. Nine-year Wilkinson Microwave Anisotropy Probe (WMAP) Observations: Cosmological Parameter Results. *"Astrophys. J. Supp."*, 208:19, October 2013.
- [101] Planck Collaboration, P. A. R. Ade, N. Aghanim, C. Armitage-Caplan, M. Arnaud, M. Ashdown, F. Atrio-Barandela, J. Aumont, C. Baccigalupi, A. J. Banday, and et al. Planck 2013 results. XVI. Cosmological parameters. *arXiv preprint astro-ph*, March 2013. <http://arxiv.org/pdf/1303.5076.pdf>.
- [102] E. T. Lau, D. Nagai, A. V. Kravtsov, and A. R. Zentner. Shapes of Gas, Gravitational Potential, and Dark Matter in Λ CDM Clusters. *"Astrophys. J."*, 734:93, June 2011.
- [103] A. Maier, L. Iapichino, W. Schmidt, and J. C. Niemeyer. Adaptively Refined Large Eddy Simulations of a Galaxy Cluster: Turbulence Modeling and the Physics of the Intracluster Medium. *"Astrophys. J."*, 707:40–54, December 2009.

- [104] M. A. Latif, D. R. G. Schleicher, W. Schmidt, and J. Niemeyer. High-resolution studies of massive primordial haloes. *"Monthly Notices RAS"*, 430:588–598, March 2013.
- [105] W. Schmidt and C. Federrath. A fluid-dynamical subgrid scale model for highly compressible astrophysical turbulence. *"Astro. & Astrophys."*, 528:A106, April 2011.
- [106] L. Iapichino, W. Schmidt, J. C. Niemeyer, and J. Merklein. Turbulence production and turbulent pressure support in the intergalactic medium. *"Monthly Notices RAS"*, 414:2297–2308, July 2011.
- [107] F. Vazza, G. Brunetti, C. Gheller, R. Brunino, and M. Brüggen. Massive and refined. II. The statistical properties of turbulent motions in massive galaxy clusters with high spatial resolution. *"Astro. & Astrophys."*, 529:A17, May 2011.
- [108] H. Böhringer and N. Werner. X-ray spectroscopy of galaxy clusters: studying astrophysical processes in the largest celestial laboratories. *"Astronomy and Astrophysics Review"*, 18:127–196, February 2010.
- [109] V. Biffi, K. Dolag, and H. Böhringer. Investigating the velocity structure and X-ray observable properties of simulated galaxy clusters with PHOX. *"Monthly Notices RAS"*, 428:1395–1409, January 2013.
- [110] I. Zhuravleva, E. M. Churazov, A. A. Schekochihin, E. T. Lau, D. Nagai, M. Gaspari, S. W. Allen, K. Nelson, and I. J. Parrish. The Relation between Gas Density and Velocity Power Spectra in Galaxy Clusters: Qualitative

Treatment and Cosmological Simulations. "Astrophys. J. Lett.", 788:L13, June 2014.

- [111] R. J. van Weeren, M. Brüggen, H. J. A. Röttgering, and M. Hoeft. Using double radio relics to constrain galaxy cluster mergers: a model of double radio relics in CIZA J2242.8+5301. "Monthly Notices RAS", 418:230–243, November 2011.
- [112] J. M. F. Donnert. Initial conditions for idealized clusters mergers, simulating ‘El Gordo’. "Monthly Notices RAS", 438:1971–1984, March 2014.